

**SURFACE/INTERFACE STUDIES OF THIN FILMS AND
DEVELOPMENT OF ULTRA-SHORT PERIOD W/B₄C
MULTILAYER MIRRORS WITH LARGE LAYER PAIRS**

By

ARINDAM MAJHI

Enrolment No: PHYS03201404006

**Raja Ramanna Centre for Advanced Technology,
Indore-452013, India**

*A thesis submitted to the
Board of Studies in Physical Sciences*

*In partial fulfillment of requirements
for the Degree of*

DOCTOR OF PHILOSOPHY

of

HOMI BHABHA NATIONAL INSTITUTE



March, 2020

Contents

Acknowledgements	vi
Summary	xii
List of Figures	xv
List of Tables	xxi
Chapter 1 Introduction	1
1.1 Introduction	2
1.2 Optical properties of the materials in the x-ray region.	5
1.3 X-ray optics.	6
1.3.1 X-ray reflective optics.	7
1.3.2 Glancing incidence optics.	8
1.3.3 Multilayer (ML) reflective optics.	10
1.3.4 Multilayer (ML) design criteria.	12
1.3.5 Advantages of the multilayer optics.	14
1.3.6 Factors affecting the performance of multilayer mirrors.	17
1.3.6.1 Quality of the interface.	17
1.3.6.2 Contrast variation.	19
1.3.6.3 Thickness error.	20
1.3.6.4 Layer Contamination and Continuity.	21
1.3.6.5 Effect of the Residual stress.	22
1.3.7 Application of the ML optics.	22
1.3.7.1 X-ray focusing and microprobe optics.	23
1.3.7.2 Polarimetry.	23
1.3.7.3 Extreme ultraviolet/soft x-ray Astronomy.	24
1.3.7.4 Soft gamma-ray energy band selector.	24

1.3.8	Importance of the ultra-short period multilayer optics. . .	24
1.3.9	Multilayer optics for the soft gamma-ray spectroscopy .	26
1.4	Resonant soft x-ray reflectivity (R-SoXR)	28
1.5	Residual stress.	29
1.6	Aim and Scope of this thesis.	31
1.6.1	A novel approach to study surface interface science of nano-scaled layered structure materials.	32
1.6.2	Understanding the evolution of residual stress with varying microstructure in nano scaled W/B ₄ C MLs.	32
1.6.3	Study of residual stress-microstructure correlation in ML mirrors with large layer pairs.	33
1.6.4	Development of ML reflective optics for soft gamma-rays.	33
Chapter 2	Experimental Details.	35
2.1	Introduction.	36
2.2	Fabrication of thin films and multilayers (MLs)	37
2.3	Electron beam evaporation system.	38
2.4	Magnetron sputtering system.	39
2.5	Characterization techniques.	41
2.5.1	X-ray reflectivity.	41
2.5.2	Reflectivity from single thin film.	44
2.5.3	Reflectivity from Multilayer (ML) film.	44
2.5.4	X-ray diffuse scattering in rocking scan geometry.	47
2.5.5	Resonant soft x-ray reflectivity (R-SoXR)	49
2.5.6	Near edge x-ray absorption spectroscopy (NEXAFS)	53

2.5.7	Transmission electron microscopy (TEM)	54
2.5.8	Residual stress measurement.	55
2.5.8.1	Substrate curvature method.	56
2.5.8.2	GIXRD based $\sin^2\chi$ method.	59
Chapter 3	A novel approach for surface interface science of nano-scaled layered structure materials.	63
3.1	Introduction.	64
3.2	Experimental details.	69
3.3	Results.	71
3.3.1	X-ray refraction spectra simulated near boron (B) K-edge.	71
3.3.2	Experimental results of near-edge reflection spectra.	75
3.3.3	Quantitative spectroscopic depth profile.	80
3.4	Conclusion.	87
Chapter 4	Understanding the evolution of residual stress with varying microstructure in nano scaled W/B₄C MLs.	88
4.1	Introduction.	89
4.2	Experimental details.	92
4.3	Results and Discussion.	93
4.3.1	Microstructural analysis (hard x-ray reflectivity and diffuse scattering)	93
4.3.2	Residual stress analysis.	103
4.3.3	Correlation between the Stress and microstructure.	108
4.4	Conclusions.	113
Chapter 5	Study of residual stress-microstructure correlation in ML mirrors with large layer pairs.	114
5.1	Introduction.	115

5.2	Experimental details.	118
5.3	Results and discussion.	119
5.3.1	Microstructure analysis.	119
5.3.2	Residual stress analysis.	123
5.4	Conclusion.	133
Chapter 6	Development of W/B₄C multilayer (ML) reflective mirror for potential application in soft gamma-rays.	135
6.1	Introduction.	136
6.2	Experimental Details.	139
6.3	Results and discussion.	140
6.3.1	Understanding of material system for soft gamma-rays reflective optics.	140
6.3.2	Analysis of microstructure.	143
6.3.3	Residual stress and period uniformity.	152
6.3.4	Measured optical performance.	154
6.3.5	Predicted soft gamma-ray performance.	157
6.5	Conclusion.	159
Chapter 7	Future scope.	161
7.1	Future scope.	156

ACKNOWLEDGEMENTS

First of all, I would like to express my sincere thanks to my Ph.D. supervisor Dr. Maheswar Nayak for his guidance, support, advice and motivation. I would definitely like to thank that he gave me the opportunity to discuss each and every question regarding the course. His activities and methods of interpretation encouraged me to think more about the subject. His fatherly advice on honesty, morals, patience and dedication for work beyond scientific discussion helped me to find joy while doing my Ph.D.

It is a great opportunity to express my gratitude to Dr. Tapas Ganguli (Division Head, SUS, doctoral committee member), at the successful completion of my thesis work. I am extremely thankful to Dr. Arup Banerjee (doctoral committee Chairperson, Dean-Academic HBNI, RRCAT), Dr. D. M. Phase (External member), Dr. A. K. Karnal (doctoral committee member), Dr. *Surya Mohan Gupta* (doctoral committee member) for their constructive motivation and guidance.

I am very grateful to Dr. P. A. Naik and G. S. Lodha for his continual help during my course. I sincerely thank our HBNI Ph.D. coordination committee members for their continuous care and help during the Ph. D. course. I sincerely thank Dr. C. P. Paul, Dean of student affairs RRCAT for all necessary support during my Ph.D. course.

I sincerely thank to Dr. Paresh Chandra Pradhan for continuous support during my Ph. D. work.

I sincerely thank Dr. Sanjay Rai (RRCAT), Dr. V. R. Reddy and Mr. A. Gome, UGC-DAE CSR Indore, for HXR and RSM measurements and faithful discussions.

I specially thank Mr. Rajkumar Gupta and Dr. M. H. Modi for help during SXR measurements and faithful discussions. I sincerely thank Mr. Mahendra Babu, Mr. Puspen Mondal, H. Srivastava and Dr. A. K. Srivastava for help in TEM measurements.

I am grateful to Dr. A. Biswas, BARC for help for x-ray diffuse scattering data fitting in IMD software.

I specially thank to Soumita, Pabitra, and Pralay for continuous support during my Ph. D. work. I specially thank Rijul, Subhomoy, Mangalika and Charu for valuable research discussions. We together had enjoyed small trips and parties.

Above all, it would not have been possible for me to achieve this milestone in my research career without encouragement and support from my all family members who have dreamed and prayed for my all around success. I sincerely thank all the persons who have helped and supported me directly or indirectly in the course of this research work.

Contents

Acknowledgements	vi
Summary	xii
List of Figures	xv
List of Tables	xxi
Chapter 1 Introduction	1
1.1 Introduction	2
1.2 Optical properties of the materials in the x-ray region.	5
1.3 X-ray optics.	6
1.3.1 X-ray reflective optics.	7
1.3.2 Glancing incidence optics.	8
1.3.3 Multilayer (ML) reflective optics.	10
1.3.4 Multilayer (ML) design criteria.	12
1.3.5 Advantages of the multilayer optics.	14
1.3.6 Factors affecting the performance of multilayer mirrors.	17
1.3.6.1 Quality of the interface.	17
1.3.6.2 Contrast variation.	19
1.3.6.3 Thickness error.	20
1.3.6.4 Layer Contamination and Continuity.	21
1.3.6.5 Effect of the Residual stress.	22
1.3.7 Application of the ML optics.	22
1.3.7.1 X-ray focusing and microprobe optics.	23
1.3.7.2 Polarimetry.	23
1.3.7.3 Extreme ultraviolet/soft x-ray Astronomy.	24
1.3.7.4 Soft gamma-ray energy band selector.	24

1.3.8	Importance of the ultra-short period multilayer optics. . .	24
1.3.9	Multilayer optics for the soft gamma-ray spectroscopy .	26
1.4	Resonant soft x-ray reflectivity (R-SoXR)	28
1.5	Residual stress.	29
1.6	Aim and Scope of this thesis.	31
1.6.1	A novel approach to study surface interface science of nano-scaled layered structure materials.	32
1.6.2	Understanding the evolution of residual stress with varying microstructure in nano scaled W/B ₄ C MLs.	32
1.6.3	Study of residual stress-microstructure correlation in ML mirrors with large layer pairs.	33
1.6.4	Development of ML reflective optics for soft gamma-rays.	33
Chapter 2	Experimental Details.	35
2.1	Introduction.	36
2.2	Fabrication of thin films and multilayers (MLs)	37
2.3	Electron beam evaporation system.	38
2.4	Magnetron sputtering system.	39
2.5	Characterization techniques.	41
2.5.1	X-ray reflectivity.	41
2.5.2	Reflectivity from single thin film.	44
2.5.3	Reflectivity from Multilayer (ML) film.	44
2.5.4	X-ray diffuse scattering in rocking scan geometry.	47
2.5.5	Resonant soft x-ray reflectivity (R-SoXR)	49
2.5.6	Near edge x-ray absorption spectroscopy (NEXAFS)	53

2.5.7	Transmission electron microscopy (TEM)	54
2.5.8	Residual stress measurement.	55
2.5.8.1	Substrate curvature method.	56
2.5.8.2	GIXRD based $\sin^2\chi$ method.	59
Chapter 3	A novel approach for surface interface science of nano-scaled layered structure materials.	63
3.1	Introduction.	64
3.2	Experimental details.	69
3.3	Results.	71
3.3.1	X-ray refraction spectra simulated near boron (B) K-edge.	71
3.3.2	Experimental results of near-edge reflection spectra.	75
3.3.3	Quantitative spectroscopic depth profile.	80
3.4	Conclusion.	87
Chapter 4	Understanding the evolution of residual stress with varying microstructure in nano scaled W/B₄C MLs.	88
4.1	Introduction.	89
4.2	Experimental details.	92
4.3	Results and Discussion.	93
4.3.1	Microstructural analysis (hard x-ray reflectivity and diffuse scattering)	93
4.3.2	Residual stress analysis.	103
4.3.3	Correlation between the Stress and microstructure.	108
4.4	Conclusions.	113
Chapter 5	Study of residual stress-microstructure correlation in ML mirrors with large layer pairs.	114
5.1	Introduction.	115

5.2	Experimental details.	118
5.3	Results and discussion.	119
5.3.1	Microstructure analysis.	119
5.3.2	Residual stress analysis.	123
5.4	Conclusion.	133
Chapter 6	Development of W/B₄C multilayer (ML) reflective mirror for potential application in soft gamma-rays.	135
6.1	Introduction.	136
6.2	Experimental Details.	139
6.3	Results and discussion.	140
6.3.1	Understanding of material system for soft gamma-rays reflective optics.	140
6.3.2	Analysis of microstructure.	143
6.3.3	Residual stress and period uniformity.	152
6.3.4	Measured optical performance.	154
6.3.5	Predicted soft gamma-ray performance.	157
6.5	Conclusion.	159
Chapter 7	Future scope.	161
7.1	Future scope.	156

List of Figures

1.1	Calculated optical constants (δ and β) for B, C, B ₄ C and W with varying energy from 50 eV to 7200 eV.	6
1.2	(a) Schematic representation reflection of incident x-ray beam on Pt thick film. (b) Calculated critical angle at the incident photon energy 8.047 keV for Pt thin film. The downward mark indicates the critical $\theta_c = 0.58^\circ$ in the inset. .9	
1.3	Schematic representation of the ML structure. Alternately high-Z layer “reflector” (A) and low-Z layer “spacer” (B) are illustrated to form ML structure. The period, d is the sum of the thicknesses of layers A and B. N is the number of layer pairs.	11
1.4	Dependence of Bragg peak position on period of ML period as well as on incident photon energy. (a) Calculated reflectivity spectra as a function of incidence angle for two W/B ₄ C ML having N=50 but varying periods 40 Å and 30 Å at energy 8 keV. (b) Calculated reflectivity spectra as a function of incidence angle for a W/B ₄ C ML having period 30 Å and N=50 at two different energies 8 keV and 20 keV.	13
1.5	Variation of calculated reflectivity as a function of the number of layer pairs for W/B ₄ C ML with period 30 Å at energy 8.047 keV. The vertical dotted line represents the number of layer pairs at which the reflectivity saturated.	14
1.6	Calculated normal incidence reflectivity from a Mo thin film mirror (ideal) and a Mo/Si ML mirror (ideal) having period d= 60 Å and number of layer pairs, N= 50 as a function of energy in the energy range 60 eV to 195 eV.	15
1.7	Calculated reflectivity profile of W/B ₄ C ML mirrors with d= 3 nm and N = 100 up to first order at the energy 8.047 keV (Cu K _α radiation).	16
1.8	Schematic of a fluorescence x-ray microprobe (Krikpatrick-Baez (KB)) using a pair of multilayer coated elliptically bent mirrors to focus incident hard x-ray.	17
1.9	The effect of roughness on the reflectivity profile at energy 8.047 keV. The reflectivity is calculated as a function of q_z for W/B ₄ C ML with period d=40 Å and N= 50 for three different roughness (0 Å, 4 Å and 8 Å).	18
1.10	Reflectivity vs. momentum transfer vector for two W/B ₄ C ML with d= 23 Å (red line) and d= 40 Å (Black line) having fixed N= 50 at energy 8.047 keV. (a) Roughness= 0 Å (b) Roughness= 8 Å.	19

1.11	The effect of electron density contrast on reflectivity profile is calculated at energy 8.047 keV for W/B ₄ C ML with period 30 Å and N=20. Black line represents the ideal density contrast ($\rho_W - \rho_{B_4C} = 16.78 \text{ g/cm}^3$), Red line represents density contrast ($\rho_W - \rho_{B_4C} = 14.86 \text{ g/cm}^3$), Blue line represents density contrast ($\rho_W - \rho_{B_4C} = 13 \text{ g/cm}^3$).	20
1.12	The effect of thickness error on reflectivity profile calculated at energy 8.047 keV for W/B ₄ C ML with period 40 Å and N=20. Black line represents without effecting random thickness error and Red line illustrates the effect of 2.5% random thickness error.	21
1.13	Schematic of the experimental arrangement of gamma-ray signal from nuclear spent fuel with the use of ML mirror.	26
2.1	Schematic of the electron beam evaporation instrument.	38
2.2	Photograph of magnetron sputtering system in our laboratory used for the fabrication of W/B ₄ C multilayer mirrors.	41
2.3	Reflection and refraction of x-ray beam from surface/interfaces.	42
2.4	Reflection and transmission of x-ray beam from a slab of finite thickness t.	44
2.5	Schematic of a multilayer which consists of a stack of bilayers.	46
2.6	Schematic of the scattering phenomenon of a many-electron atom with incident radiation.	50
2.7	Schematic of the Zygo Mark-II laser Fizeau interferometer set-up for experimental arrangement.	57
2.8	Drawing of the radius of curvature measurement from the spherical surface profile.	58
2.9	(a) Schematic diagram of GIXRD method for residual stress measurement. (b) In-plane and out of plane direction are shown on the W/B ₄ C ML sample. .60	
3.1	(a) Schematic energy level diagram of the Si atom with incident photon energy just below the Si L-edge. (b) The variation of the scattering factors (f_1 and f_2) around the Si L-edge. (c) Schematic energy level diagram of the Si atom with incident photon energy just above the Si L-edge.	67
3.2	The schematic of the angular R-SoXR measurement and energy dependent reflection measurement along with NEXAFS measurement in the thin film layer structure are shown in this figure. (a) angular R-SoXR measurement, (b) energy dependent reflection measurement along with NEXAFS measurement.	70

3.3	Energy dependent grazing incidence reflection spectra calculated near B K-edge for an ideal structure (considering bulk density and zero roughness) along with measured optical constants of elementary boron. (a) Reflection spectra at a grazing incidence angle of 2° by varying the thickness of the top C layer. (b) and (c) show the variation of the reflection spectra as function of grazing incidence angle for the two different thicknesses of 200 Å and 20 Å of the top C layer, respectively. (d) Measured near edge spectral dependent optical constants (δ and β) of boron. The vertical dotted lines correspond to the positions of the dip ($E \sim 189.4$ eV) and peak ($E \sim 191.3$ eV) in the δ and β profiles, respectively.	73
3.4	The measured reflection spectra (energy dependence) (coloured line) at different selected incidence angles around the K-edges of C, B. Also, the measured NEXAFS spectrum (black line) at 45° close to the respective edges is shown. (a) C K-edge region. (b) B K-edge region. The vertical dotted lines represent the fine structure features at different energy positions as mentioned in the text.	77
3.5	The measured reflection spectra (energy dependence) (coloured line) at different selected incidence angles around the O K-edge and Si L-edge. Also, the measured NEXAFS spectrum (black line) at 45° close to the respective edges is shown. (a) O K-edge region. (b) Si L-edge region. The vertical dotted lines represent the fine structure features at different energy positions as mentioned in the text.	79
3.6	Measured Hard X-ray reflectivity (using Cu K_α source, $E=8.047$ keV) with fitted curves of the layer structure and electron density profile (inset) are shown in the figure.	81
3.7	(a) Measured and fitted angular R-SoXR measurements around the B K-edge at the selected energies. The spectra are shifted vertically for clarity. This figure analyzes the quantitative structural and compositional analysis using angle dependent R-SoXR near to the B K-edge. (b) Spectra of the atomic scattering factors of B around the K-absorption edge. The coloured shadow area exhibits the energy range over which R-SoXR performance was carried out.	82
3.8	(a) Measured R-SoXR spectra at energies near the B K-edge of B_2O_3 . (b) This figure shows the variation of atomic scattering factor of B_2O_3 . The shadowed region indicates the energy range over which the measured R-SoXR profiles were presented.	83

3.9	The measured and the fitted R-SoXR data at 190.7 eV demonstrating the sensitive of R-SoXR to atomic composition of the resonating atoms in a layered structure.	84
3.10	(a) The effective electron density (EDP) depth profiles obtained from the best-fit R-SoXR results. (b) Schematic representation of variation of spatial composition according to the best-fit R-SoXR data.	85
4.1	Measured (colored circles) and fitted (solid black line) HXR profiles of W/B ₄ C MLs with altering the thickness of individual layer and constant N = 20 for Set-A and Set-B. (a) For sample set-A, the thickness of the W layer reduces from 2.03 nm to 1.06 nm (ML-a to ML-d) at a fixed thickness of the B ₄ C layer of ~2.9 nm. (b) For sample set-B, the thickness of the B ₄ C layer reduces from 2.14 nm to 0.4 nm (ML-e to ML-h) at a fixed thickness of W layer of ~1.7 nm. For ML-g, the measured Kiessig fringes (N-2 number) between 2 nd and 3 rd Bragg peak of ML-g are indicated by the vertical downward arrows in inset. The HXR profiles are vertically shifted for clear picture.	95
4.2	Measured (colored bubble) and fitted (solid black line) x-ray diffuse scattering spectra of W/B ₄ C multilayers. (a) set-A (b) set-B.	99
4.3	(a) Measured GIXRD profile of the ML-c at energy 15.4 keV at (α) = 0.6° and at χ = 0°. (b) Crystallite size with considering W (110) plane as a function of thickness of the W layer.	103
4.4	Two dimensional surface contour plot of W/B ₄ C MLs. [(a) before deposition and (b) after deposition] for ML-a and [(c) before deposition and (d) after deposition] for ML-e. The height of the surface profile is indicated by the colour contrast.	104
4.5	Variation of the diffraction peak position (2θ) relating to the W (110) plane with $\sin^2\chi$ for ML-b and ML-h.	105
4.6	Variations of residual stress as a function of the individual layer thickness. (a) Set-A, with varying the W layers thickness at unchanged thickness of the B ₄ C layer of 2.9 nm. (b) Set-B, with varying the B ₄ C layers thickness at a fixed thickness of W layer of 1.7 nm. In (b), the stress value of ML-b is re-plotted from set-A for extrapolation of B ₄ C thickness up to 2.9 nm. The solid line with data points and the dotted line with data points represent the total residual stress and stresses in the W layers of the ML stack, respectively.	107
4.7	Schematic of a B ₄ C layer on a W layer at two different important growth stages. (a) At the W layer thickness of ~ 1.06 nm, discontinuous-to-continuous	

	transition. (b) At the W layer thickness of ~ 1.38 nm, onset of formation of the continuous layer.	111
5.1	Measured (coloured bubbles) with fitted (black solid lines) HXR profiles of W/B ₄ C MLs as a function of N from 20 to 400 at unchanged period of $d \approx 1.9$ nm. Random layer thickness errors are considered as 0.006 nm and 0.013 nm for MLs with N=300 and 400, respectively during the fitting. In case of N =20, 50 and 100, the measured XRR spectra are fitted with constant period.	120
5.2	Measured diffuse scattering spectra (coloured bubbles) of W/B ₄ C MLs with varying N = 20-400 at $d \sim 1.9$ nm. Solid black lines correspond to the fitted profiles N = 20, 50 and 100.	123
5.3	2-D surface shape profile of W/B ₄ C ML having N = 400, (a) before fabrication and (b) after fabrication. The height of the profile is indicated by colour variation.	124
5.4	Measured total residual stress of W/B ₄ C MLs as a function of N. The total residual decreases with increasing N and also it is still compressive in nature. The period thicknesses of these MLs are fixed ~ 1.9 nm.	125
5.5	Measured residual stress of W/B ₄ C MLs as a function of periodicity. The periodicity (d) varies from 1.2 nm to 1.97 nm at fixed N=300.	126
5.6	The variation of total residual stress as a function N from 20 to 100 having period $d \sim 1.9$ nm with time evolution. Black coloured line shows the measurement within 4 months from sample fabrication. The Red coloured line shows the measurement of residual stress after two years from first measurement.	127
5.7	((a) Measured GIXRD profile of W/B ₄ C ML with N=300 at energy 15.695 keV and $\chi=0$. (b) Variation of diffraction peak position (2θ) relating to W(211) with changing $\text{Sin}^2\chi$ for multilayer with N=300.	129
5.8	Measured residual stress of W layers in W/B ₄ C MLs with varying N. The solid line and dashed line show that stresses have been determined by two elastic constants values (bulk and thin film). The red lines illustrate the variation of residual stress using W(110) plane at an incidence angle 0.6° whereas the black lines represent the variation of residual stress using W(211) plane at an incidence angle 4.5°	131
6.1	The reflectivity performances of four different ML systems (WC/SiC, WC/B ₄ C, W/Si and W/B ₄ C) are calculated by considering ideal mass densities at the energy 300 keV. Both the step size and instrumental angular resolution	

($\Delta\theta$) are kept fixed at 0.0001° for that calculation. (a) Peak reflectivity of the 1st order Bragg peak as a function of interface width (σ). The calculations are performed for MLs with $d = 1.86$ nm, $N = 400$, and Γ ratio = 0.505. The dotted line represents the interfacial width (σ) = 0.275 nm of earlier reported soft gamma ray WC/SiC ML optics [9] and the dashed line indicates the $\sigma = 0.27$ nm for W/B₄C ML optics in the current work. The corresponding calculated reflectivities at the above specified interfacial width are indicated by the positions of the blue and olive colored arrows. (b) The 1st order Bragg peak reflectivity with varying N represents the material dependent of saturated peak reflectivity (indicated by arrows). 142

6.2 Measured and fitted HXR spectra at energy 10 keV of three W/B₄C MLs with varying periods $d = 1.86$ nm (ML-1), 1.55 nm (ML-2) and 1.23 nm (ML-3) at a fixed $N = 400$ with considering random thickness error ~ 0.012 nm, instrumental angular resolution 0.001° . Also, measured reflectivity spectra are fitted at energy band (± 1 eV) with interval 1 eV and then averaged over the energy band width. 145

6.3 The RSM Measured data of three W/B₄C MLs at energy 8.047 keV. The figures in left panel (a-d) are of ML-1, the figures in the middle (e and f) are of ML-2 and the figures in right panel (g and h) are of ML-3. In left panel: (a) 1st order Bragg peak, (b) 2nd order, (c) 3rd order and (d) 4th order. In the middle: (e) 1st order Bragg peak and (f) 2nd order peak. In right panel: (g) 1st order Bragg peak, and (h) 2nd order peak. 148

6.4 High resolution cross-sectional TEM images of W/B₄C MLs with $N = 400$. (a) ML-2 with $d = 1.55$ nm. (b) ML-3 with $d = 1.23$ nm. (c) line profile of the ML-2. (d) line profile of the ML-3.. . . . 149

6.5 Measured and fitted GIXRD profiles of W (110) diffraction of ML-1, ML-2 and ML-3 at energy 17.295 keV. (a) Out-of plane diffraction (b) In-plane diffraction with data taken at an angle 18° above the sample surface. . . 141

6.6 Schematic of morphology of W layer near the layer continuous limit representing correlation between roughness and surface density of grains. As surface density of grains increases gradually (indicated by arrows), the morphology tends toward more compact and smoother. The color code represents the different orientations of crystallites (particles). 152

- 6.7 Measured HXR data (at Cu K_{α} energy) of three W/B₄C ML samples (MS1, MS2, MS3) with a fixed N= 300 fabricated simultaneously.154
- 6.8 Measured optical performances of W/B₄C ML with d = 1.86 nm and N = 400 for selected energy in the energy range 10-20 keV. The reflectivity around 1st Bragg peak in the linear scale as a function of incident angle is shown in the lower figure. The top figures show more clearly the Bragg peaks at three selected energies to measure angular resolution. 156
- 6.9 Comparative measured optical performances at 1st Bragg peak of three W/B₄C MLs with ML-1 (d = 1.86 nm), ML-2 (1.55 nm) and ML-3 (1.23 nm) at a fixed N = 400 at an energy 10 keV. Measured reflectivity profiles in linear scale are plotted as a function of incident angle. The inset shows reflectivity multiplied with θ^4 as function of θ157
- 6.10 1st order Bragg peak reflectivity performances of three MLs with varying instrumental angular resolution ($\Delta\theta$) are calculated at energies of 384 keV ($\Delta E = 3$ keV) and 378 keV ($\Delta E = 9.8$ keV). The calculation is done with an angular step size 0.1 mdeg using measured structural parameters of MLs derived from hard x-ray data and by extrapolation of known optical properties of materials. The black line and red line indicate the energies 384 keV and 378 keV. The dotted line represents a typical instrumental angular resolution of 0.024 mdeg, where the respective peak reflectivities are marked by arrows. (a), (b) and (c) are for ML-1, ML-2 and ML-3, respectively.158

List of Tables

2.1	Characterization techniques with brief description of the measurements.	61
3.1	The best-fit results of HXR the thickness, rms roughness and mass density.	80
3.2	The table contains the best-fit results of the composition of the layers structure, layer thickness, and rms roughness earned from R-SoXR measurement.	86
4.1	The best fit results of HXR of W/B ₄ C MLs with varying individual layer thickness. d , t , ρ , σ and R denote ML periodicity, layer thickness, mass density, interface width and 1 st Bragg peak reflectivity, respectively.	97
4.2	X-ray diffuse scattering performance results. σ_r and σ_d are physical roughness and interfacial diffuseness, respectively. ξ_{\parallel} and ξ_{\perp} are in-plane and perpendicular correlation lengths, respectively. .	100
5.1	The best fit results of HXR of W/B ₄ C MLs with varying N . d , t , ρ and σ denote as ML period, layer thickness, mass density and interfacial width, respectively.	121
5.2	Best-fit results of diffuse scattering spectra. σ_r , and σ_d represent physical roughness and interfacial diffuseness where as ξ_{\parallel} and ξ_{\perp} represent the lateral correlation length and perpendicular correlation length, respectively.	123
6.1	Best fit HXR results of W/B ₄ C MLs at energy 10 keV. d , t , σ and ρ are period, thickness of layer, interface width and mass density of layer, respectively.	145
6.2	The best fit GIXRD results of W (110) diffraction peak along with average size of crystallite (particle).	151
6.3	The values of the measured peak reflectivities R and $E/\Delta E$ of three MLs at 10 keV.	156

Summary

X-ray multilayer optics finds potential applications in a wide spectral region from extreme-ultra-violet to soft gamma-rays. It has potential scientific and technological applications in diverse fields such as synchrotron radiation instrumentation, astrophysics, plasma diagnosis etc. However, the fabrication of such periodic ML structure is a challenging aspect, where the control on structural parameters on angstrom level is required. Any deviations of these parameters from the desired values affect the optical properties. Recently, attention is made towards exploitation of soft gamma-rays (100 to 600 keV) to advance scientific and technological applications in the emerging frontier areas of both nuclear physics as well as high energy astrophysics. Thus, the central issue to develop ML mirror of such high energies is the understanding of microstructure of layers at an early stage of film growth, physics/chemistry of formation of interfaces, their correlation with residual stress in ML stack, and thereafter development of such ML mirror with the required structural parameters.

The properties of the thin film and multilayer structures are strongly governed by the distribution & chemical nature of the elements and presence of impurity across the buried interfaces. Therefore, it is important to understand precisely the surface/interface phenomena for improving the quality of the films. For that purpose, a novel approach is developed by combining the resonant soft x-ray reflection spectroscopy at grazing incidence near the “critical angle” with angular dependent reflection at energies around the respective absorption edges to precisely quantify spatio-chemical depth profile in a non-destructive manner. The developed approach is demonstrated on the layered model structure C(20 Å)/B(40 Å)/Si(300 Å)/W(10 Å)/Substrate. To observe the presence of different chemical states of elements qualitatively, the glancing incidence reflection spectra are recorded at the near respective absorption edges (K-edges of B, C and O; and L-edge of Si) with different

incident angles near critical angle and also the results are verified with the routinely used NEXAFS spectroscopy. Thereafter, the angular resonant curves at the respective absorption edges precisely quantify its profile in a nano-scaled layered structure configuration. The approach developed enables to reconstruct a highly precise chemically- and spatially-resolved nano-scaled interfacial map from free surface to the embedded layers up to few tens of nanometers comparable to the dimension of the devices.

The residual stress in x-ray multilayer (ML) plays important role in the performance of x-ray optics. Thus, it is important to understand the evolution of the residual stress as well as the correlation with microstructure for better performance of ML mirrors. The evolution of the residual stress has been studied in W/B₄C MLs system with systematically varying individual layer thickness in ultra-thin limit. The observed variation of the residual stress has been explained on the basis of the mechanism of growth of film at different stages at early stage of film formation. The total residual stress in ML stack which is obtained using interferometer is correlated with the stress of W layers obtained by grazing incidence x-ray diffraction (GIXRD) based $\sin^2\chi$ method using synchrotron. The total residual stress in W/B₄C ML stack is compressive in nature, is correlated with the compressive residual stress of W layers. The contributions of stress originating from layers and interfaces are correlated with the total stress in the ML stack. The experimental results show that the total stress in the MLs is less compared to the stress in the W layers. Therefore, it is indicated that the net stresses generated in B₄C layers and interfaces are tensile in nature. The contributions of stress originating from layers and interfaces are correlated with the total stress in the ML stack. A non-monotonic variation of compressive residual stress is observed with varying the microstructure.

Similarly, it is interesting to understand evolution of residual stress and its correlation with microstructure as a function of the number of layer pairs (N) for

development of ultra-short period multilayer (ML) optics with large N in soft gamma-ray application. Thus, the evolution of residual stress is studied in W/B_4C ML optics varying N from 20 to 400 with fixed period ~ 1.9 nm. The result shows that the both the residual stress (total stress and stress in W layers) are compressive in nature residual and total stress is less compared to the stress in W layers. It indicates that the combined stress due to B_4C layer and interface is tensile in nature. The compressive stress decreases with increasing N . It is observed that the total residual stress decrease from -1.444 GPa to -0.389 GPa with increasing N from 20 to 400. This may be due to relaxation of stress in MLs as the number of layer pair increases. For the ML with $N=400$ the total residual stress is -0.389 GPa which is in tolerable range for ML mirror suitable soft gamma ray optics.

Finally, W/B_4C ML optics for soft gamma rays application are developed with low residual stress and with achievable interface width by varying period $d = 1.86$ - 1.23 nm at a fixed number of layer pairs $N = 400$. The average interfacial widths are ~ 0.27 nm and 0.285 nm for multilayer mirrors having $d = 1.86$ and 1.55 nm, respectively. The maximum stress in multilayer stacks measured is -0.389 GPa for $d = 1.86$ nm. An excellent optical performances are measured in the energy range 10 to 20 keV, e.g., reflectivities ≈ 64 % (39%) with energy resolution $E/\Delta E \approx 76 \pm 1$ (133 ± 1) are obtained for MLs with $d = 1.86$ nm ($d = 1.55$ nm) at photon energy of 10 keV. The expected optical performance at soft gamma rays are predicted considering the structural parameters obtained from hard x-ray model and extrapolated known optical constant of materials. The results show W/B_4C could be the material of choice for soft gamma-ray optics to provide high photon flux due to superior optical contrast, ability to yield low interface width as well as low residual stress.

Summary

X-ray multilayer optics finds potential applications in a wide spectral region from extreme-ultra-violet to soft gamma-rays. It has potential scientific and technological applications in diverse fields such as synchrotron radiation instrumentation, astrophysics, plasma diagnosis etc. However, the fabrication of such periodic ML structure is a challenging aspect, where the control on structural parameters on angstrom level is required. Any deviations of these parameters from the desired values affect the optical properties. Recently, attention is made towards exploitation of soft gamma-rays (100 to 600 keV) to advance scientific and technological applications in the emerging frontier areas of both nuclear physics as well as high energy astrophysics. Thus, the central issue to develop ML mirror of such high energies is the understanding of microstructure of layers at an early stage of film growth, physics/chemistry of formation of interfaces, their correlation with residual stress in ML stack, and thereafter development of such ML mirror with the required structural parameters.

The properties of the thin film and multilayer structures are strongly governed by the distribution & chemical nature of the elements and presence of impurity across the buried interfaces. Therefore, it is important to understand precisely the surface/interface phenomena for improving the quality of the films. For that purpose, a novel approach is developed by combining the resonant soft x-ray reflection spectroscopy at grazing incidence near the “critical angle” with angular dependent reflection at energies around the respective absorption edges to precisely quantify spatio-chemical depth profile in a non-destructive manner. The developed approach is demonstrated on the layered model structure C(20 Å)/B(40 Å)/Si(300 Å)/W(10 Å)/Substrate. To observe the presence of different chemical states of elements qualitatively, the glancing incidence reflection spectra are recorded at the near respective absorption edges (K-edges of B, C and O; and L-edge of Si) with different

incident angles near critical angle and also the results are verified with the routinely used NEXAFS spectroscopy. Thereafter, the angular resonant curves at the respective absorption edges precisely quantify its profile in a nano-scaled layered structure configuration. The approach developed enables to reconstruct a highly precise chemically- and spatially-resolved nano-scaled interfacial map from free surface to the embedded layers up to few tens of nanometers comparable to the dimension of the devices.

The residual stress in x-ray multilayer (ML) plays important role in the performance of x-ray optics. Thus, it is important to understand the evolution of the residual stress as well as the correlation with microstructure for better performance of ML mirrors. The evolution of the residual stress has been studied in W/B₄C MLs system with systematically varying individual layer thickness in ultra-thin limit. The observed variation of the residual stress has been explained on the basis of the mechanism of growth of film at different stages at early stage of film formation. The total residual stress in ML stack which is obtained using interferometer is correlated with the stress of W layers obtained by grazing incidence x-ray diffraction (GIXRD) based $\sin^2\chi$ method using synchrotron. The total residual stress in W/B₄C ML stack is compressive in nature, is correlated with the compressive residual stress of W layers. The contributions of stress originating from layers and interfaces are correlated with the total stress in the ML stack. The experimental results show that the total stress in the MLs is less compared to the stress in the W layers. Therefore, it is indicated that the net stresses generated in B₄C layers and interfaces are tensile in nature. The contributions of stress originating from layers and interfaces are correlated with the total stress in the ML stack. A non-monotonic variation of compressive residual stress is observed with varying the microstructure.

Similarly, it is interesting to understand evolution of residual stress and its correlation with microstructure as a function of the number of layer pairs (N) for

development of ultra-short period multilayer (ML) optics with large N in soft gamma-ray application. Thus, the evolution of residual stress is studied in W/B_4C ML optics varying N from 20 to 400 with fixed period ~ 1.9 nm. The result shows that the both the residual stress (total stress and stress in W layers) are compressive in nature residual and total stress is less compared to the stress in W layers. It indicates that the combined stress due to B_4C layer and interface is tensile in nature. The compressive stress decreases with increasing N . It is observed that the total residual stress decrease from -1.444 GPa to -0.389 GPa with increasing N from 20 to 400. This may be due to relaxation of stress in MLs as the number of layer pair increases. For the ML with $N=400$ the total residual stress is -0.389 GPa which is in tolerable range for ML mirror suitable soft gamma ray optics.

Finally, W/B_4C ML optics for soft gamma rays application are developed with low residual stress and with achievable interface width by varying period $d = 1.86$ - 1.23 nm at a fixed number of layer pairs $N = 400$. The average interfacial widths are ~ 0.27 nm and 0.285 nm for multilayer mirrors having $d = 1.86$ and 1.55 nm, respectively. The maximum stress in multilayer stacks measured is -0.389 GPa for $d = 1.86$ nm. An excellent optical performances are measured in the energy range 10 to 20 keV, e.g., reflectivities ≈ 64 % (39%) with energy resolution $E/\Delta E \approx 76 \pm 1$ (133 ± 1) are obtained for MLs with $d = 1.86$ nm ($d = 1.55$ nm) at photon energy of 10 keV. The expected optical performance at soft gamma rays are predicted considering the structural parameters obtained from hard x-ray model and extrapolated known optical constant of materials. The results show W/B_4C could be the material of choice for soft gamma-ray optics to provide high photon flux due to superior optical contrast, ability to yield low interface width as well as low residual stress.

Chapter-1

Introduction:

This chapter discusses the general overview of the thesis work and its importance. A brief overview of the x-ray optics and its applications are discussed. The discussion continues with the resonant soft x-ray reflectivity is a novel potential tool to obtain the spatio-chemical depth profile from free to buried interfaces as it is required for a better understanding of the physics and chemistry of the formation of interfaces. The evolution of residual stress and its correlation with the microstructure in the multilayer structure is also discussed to understand and improve for better optical performance and long term structural stability. Finally, a brief overview about the importance of development of a metal-based (W/B₄C) high efficient multilayer reflective optics for the soft gamma-ray is presented. This chapter also introduces the aim and scope of the thesis. The detail of the introduction is described as follows.

1.1 Introduction:

Today's central objective of the nano-structured material science is the control of the materials and their morphologies along with the interface structures at the atomic levels to tune their optical, magnetic, superconducting, electronic properties etc [1-8]. Frequently, the film quality is a governing factor that determines the structural and chemical parameters in a nano-scaled layer structure to maintain its functionality. Any deviation of their structural and chemical parameters from the desired values may affect their properties; for example, the catastrophic drop of reflectance of the ultra-short-period x-ray multilayer mirrors is observed as the layer thickness approaches towards the quasi-continuous limit [9]. Besides, the problem becomes more difficult owing to the interlayers formation, atomic migration, and the chemical reactions which may impact the functionality of the nano-scaled devices e.g., affecting the optical contrast [10] or their magnetization [11] etc.

Like visible optics manipulates visible light, x-ray optics manipulates x-rays for the advancements of science and technology. The smaller wavelength of x-rays writes smaller features in lithography and sees smaller features in microscopy. However, as the wavelength decreases the corresponding tolerances are required for the fabrication of x-ray optics to angstrom level compared to visible optics. So there is a demand for improving thin film technology with the higher structural requirement. Apart from that, it is also equally important for a better understanding of physics and chemistry of surface & interface of nano-scaled layer structure device to improve the underlying performances. From few decades much attention is made towards utilizing x-rays to advance scientific and technological applications in emerging frontier areas. One of the important issues for this exploitation is the development of challenging x-ray multilayer (ML) optics, which involves complex understanding of interfacial phenomena at sub-nanometer scale. X-ray multilayer (ML) mirror is an artificial one-dimensional periodic multilayer structure (see schematic in Fig

1.3). It consists of two different materials deposited alternatively in a periodic manner, so that the reflection from periodic interfaces adds in phase to enhance reflectivity when it satisfies the Bragg condition. Due to shorter wavelengths of the x-rays, the period of the x-ray multilayer (ML) mirrors is in the range of few to several nano-meters. Like visible optics, x-ray ML optics manipulates x-rays for different scientific and technological applications such as in synchrotron beamline to condition x-rays [12, 13], radiation biology [14], plasma diagnostics [15], x-ray lithography [16], x-ray astronomy [17] etc. Recently, ML optics also finds application in further higher energies, for examples, ML based soft gamma-ray reflective optics used in soft gamma-ray spectroscopy for the applications in the nuclear technology [9, 18] as well as in the high energy astrophysics [19, 20].

As the part of the work in this thesis, the work related to a novel analytical methodology has been demonstrated that is in general applicable to more complex nano-scaled layered structure materials to study the physics and chemistry of the buried interfaces. This is because the understanding of surface-interface phenomenon is very significant for nano-scaled layer structure to improve its functionality. The technique is based on the near-edge resonance scattering phenomenon in the soft x-ray region. This approach enables to quantitatively reconstruct a spatio-chemical map from free surface to the buried layer in non-destructive manner. This methodology is developed by the combination of resonant soft x-ray reflection spectroscopy at grazing incidence close to the “critical angle” with angle-dependent reflection at energies in the region of the corresponding absorption edges.

The second part of the thesis involves the work related to understanding the physics of multilayer and the development of the reflective ML optics for soft gamma-ray. Generally, the advantages of the ML reflective optics are that the period thickness, composition of layers can be tuned for operating at the desired wavelength as well as at the desired incidence angle. In addition, the ML mirror can be deposited on a curved substrate for focusing and/or

imaging applications [21, 22]. In EUV/soft x-ray region, ML mirrors provide high near normal reflectivity with a moderate spectral band pass. In the hard x-ray, ML optics used at relatively larger incident angles compared to single surface glancing incidence optics. Further, the advantage of ML optics is that it provides significantly higher photon flux compared to the diffractive optics [23]. Many experiments require high photon flux with a moderate resolution like x-ray reflectivity, x-ray fluorescence, and experiments where the incident photon flux is very low, like in high energy astronomy etc. Recently, ultra-short period (1-2 nm) ML optics has been used for high energy applications (soft gamma-ray) [9]. However, the fabrication of such ML optics is a challenging task because the structural parameters need to be controlled at the angstrom level. Apart from fabrication, understanding the physics and chemistry of the formation of interfaces is crucial aspects, when the layer thickness is around 0.5-1 nm. Typical structural parameters of such ML optics for high energy applications are as periodicity (d) ~1-2 nm; number of layer pairs (N) 300-500; interfacial width (σ) ~0.2-0.3 nm and residual stress in ML stack ~0.2-0.5 GPa. To realize Bragg's reflection of such higher energies of soft gamma rays by ML optics, the period of the ML must be controlled to the lowest possible desired values with structural perfection at the atomic level. In order to do that, the main difficulty in achieving the ultimate shortest period is limited by the minimum thickness to form a continuous layer that depends on the material and its growth. Also, the study of residual stress is another important aspect because it has destructive effect on the performance of the ML optics. The residual stress can create crack or buckle in the film due to high residual stress [24]. It also reduces the peak intensity increasing the width of the reflectivity peak, angular resolution [25]. Due to high residual stress, the ML may become unstable over time and peel off from the substrate [26].

Thus, the central theme of the present thesis is to understand the microstructure of the layers in the early stages of film formation, the physics/chemistry of the interface formation,

their correlation to the residual stress of the ML stack, and subsequently the development of ML optics for soft gamma-ray energy range.

1.2 Optical properties of the materials in the x-ray region:

X-ray was first discovered in 1895 by Wilhelm Conrad Röntgen. It is an electromagnetic radiation. Commonly, x-rays are generated by the transition of inner electrons in the atomic orbital. X-rays can also be generated by other sources like laser produced hot plasma and synchrotron source. There is no sharp boundary limit from one spectrum to another spectrum. The energy range $\sim 40\text{-}500$ eV is known as extreme ultra violet (EUV). This is followed by the energy range ~ 500 eV-6 keV, which is known as soft x-ray. The EUV and soft x-ray combining is sometime known as x-ray ultraviolet (XUV). Similarly, the energy range of the x-rays is $\sim 6\text{-}100$ keV is known as hard x-rays. The further higher energy beyond 100 keV is known as gamma-rays (up to few hundreds keV, known as soft gamma-rays). The x-ray interaction with materials strongly depends on the optical properties of the material in the desired wavelengths. Since the interaction undergoes through both the elastic and inelastic (dissipative), therefore, the refractive index is complex. So, the refractive index “n” is written as [27].

$$n = 1 - \delta + i\beta = 1 - \frac{r_e}{2\pi} \lambda^2 N_a (f_1 - if_2) \quad (1.1)$$

where, δ and β are optical constants of the material, r_e is the Thomson scattering length, N_a is atomic number density (atoms per unit volume). f_1 and f_2 are the real and imaginary part of the atomic scattering factor. The optical constants are real, and they depend both on the material and the wavelength. For all material the values of $\delta = 10^{-2}$ to 10^{-5} and $\beta = 10^{-3}$ to 10^{-7} , in the x-ray region except at atomic absorption edges, where anomalous effects take place. At the absorption edges, the optical constants are highly sensitive to the configuration of an atom in its environment. Therefore, it can distinguish the chemical composition of the

material by tuning the photon energy near the absorption edges. The optical constants (δ and β) of the materials (B, C, B₄C and W) with varying energy are calculated from Henke database [28] as shown in Figure 1.1. In the x-ray range, the optical properties are defined based on the interaction of photon with the electrons at different shells. Near absorption edges, inner shell electrons contribute to the absorption of x-rays and give rise to the series of jumps at the binding energy of these electrons. The optical constant δ can even be negative near the absorption edge for some of the materials. This is called anomalous dispersion. Material selection for the design of x-ray multilayer reflective optics for a particular energy is based on the optical properties of materials apart from their structural stability.

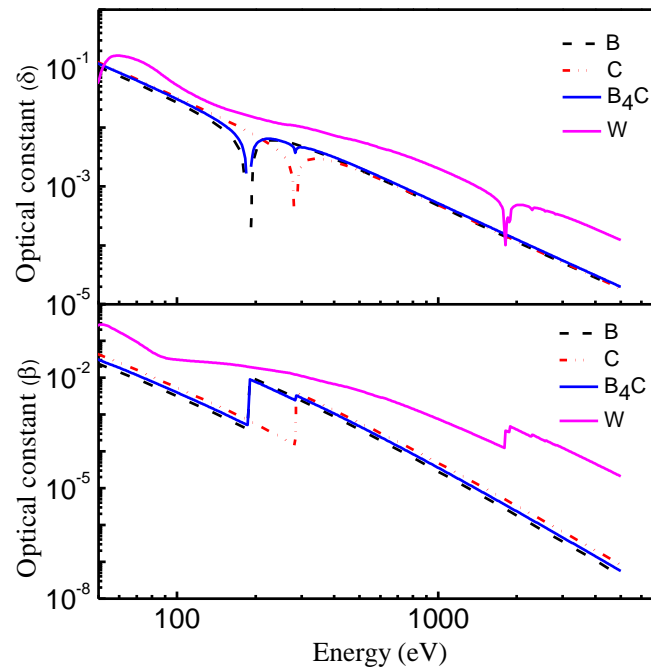


Figure 1.1 Calculated optical constants (δ and β) for B, C, B₄C and W with varying energy from 50 eV to 7200 eV.

1.3 X-ray optics:

From few decades, the synchrotron radiation sources are widely used to analyze the structural, compositional and chemical properties of materials. Different types of x-ray

optical elements are used to advance the synchrotron-based experimental techniques. Here, “x-ray optical elements” means the x-ray optical device, which is used to condition/manipulate the x-ray beam. Again, x-ray optical elements are also used in various scientific fields such as plasma diagnostic, medical diagnostics, radiation biology and x-ray astronomy. Commonly, the x-ray optical elements work in three different phenomena (a) refraction, (b) diffraction and (c) reflection. The refractive index of a material is very close to 1 for the x-ray region. Therefore, the refraction angle is very small which makes conventional refractive lenses having very large focal lengths. Considering the diffraction principle, gratings and zone plates and, recently, Bragg-Fresnel optics [29] are used as the optical elements for x-rays with the wavelength in the range $\approx 20 \text{ \AA}$ - 40 \AA (and in some cases over a wider range). Since this thesis concerns x-ray multilayer optics, we will deliberate on the discussion of x-ray reflective optics (glancing incidence optics and multilayer optics).

1.3.1 X-ray reflective optics:

Generally, x-ray reflective optics (glancing incidence optics and multilayer optics) is based on Fresnel’s reflection formalism. For the specular reflection, the transverse component of the momentum transfer vector at the boundary of two materials is $q_z = \frac{4\pi \sin\theta}{\lambda}$ and the lateral component is $q_{x,y} = 0$. Here, θ and λ are the incident angle with respect to the sample surface and incident wavelength, respectively. According to the Fresnel equation, at specular condition, the amplitude of reflection and transmission for S-polarized wave (electric field is perpendicular to the plain of incidence) can be written as (more details are discussed in chapter 2 in section 2.5.1)

$$r^s = \frac{n_1 \sin\theta - n_2 \sin\theta}{n_1 \sin\theta + n_2 \sin\theta} \quad (1.2)$$

$$t^s = \frac{2n_1 \sin\theta}{n_1 \sin\theta + n_2 \sin\theta} \quad (1.3)$$

The reflectivity from the surface is $R = |r^s|^2$. For normal incidence condition ($\theta=90^\circ$) the reflectivity is calculated as

$$R_{s,\perp} = \left| \frac{n_1 - n_2}{n_1 + n_2} \right|^2 \approx \frac{\delta^2 + \beta^2}{4} \quad (1.4)$$

Since for the x-ray region, the values of δ and β are very low, therefore, the reflectivity at the normal incident condition from a single interface is very low for x-rays.

1.3.2 Glancing incidence optics:

The glancing incidence optics (thin film mirror) is based on the phenomenon of total external reflection. According to Snell's law the total external reflection of x-rays from a single surface happens when the incidence angles is less than the critical angle. The critical angle can be written as [27]

$$\theta_c \approx \sqrt{2\delta} = \lambda \sqrt{r_e \rho_0 / \pi} \quad (1.5)$$

where, r_e and ρ_0 are the Thompson scattering length and electrons density, respectively. Therefore, θ_c is proportional to the wavelength of the incident beam and the square root of the electron density of the material. A schematic of glancing incidence optics (thin film mirror considering Pt thin film) on a thick substrate is shown in figure 1.2 (a). Here, the incidence angle is defined as the angle between the incident ray and the sample surface. At $\lambda = 1.54 \text{ \AA}$, the critical angle for different materials is less than 0.65° . For example, the value of the θ_c is 0.58° for platinum (Pt) mirror at $\lambda=1.54 \text{ \AA}$ (hard x-rays) and up to few degree for soft x-ray region. The critical angle for Pt thin film mirror is shown in the figure 1.2 (b) (marked by the arrow in the inset).

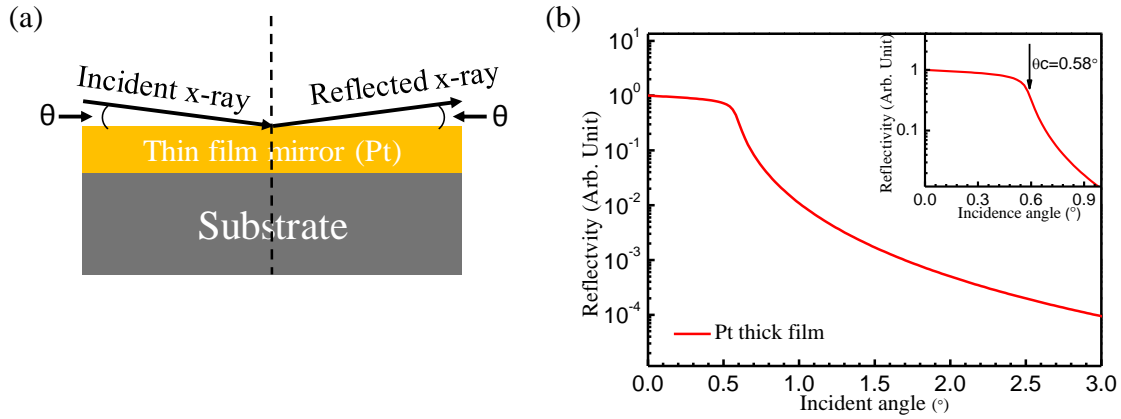


Figure 1.2 (a) Schematic representation reflection of incident x-ray beam on Pt thick film. (b) Calculated critical angle at the incident photon energy 8.047 keV for Pt thin film. The downward mark indicates the critical $\theta_c = 0.58^\circ$ in the inset.

Above the critical angle, the reflectivity falls as q_z^{-4} ($q_z = \frac{4\pi \sin\theta}{\lambda}$, is the momentum transfer vector in the normal direction of the sample surface). At normal incidence condition, the reflectivity is extremely low and drops significantly above the critical angle. The typical value of the reflectivity from a single surface ranges from 10^{-3} and 10^{-6} at the normal incidence condition. The reflectivity can be enhanced by adding the reflected intensities in-phase from periodic interfaces by fabricating periodic multilayer structure as compared to the thin film mirror. More details about multilayer optics are discussed in the next section.

The selection of the material for a glancing incidence mirror depends on its application. The thermal properties of the material are of importance in high photon flux applications (e.g. in synchrotron application), where thermal distortion of mirrors may occur. Therefore, an ideal material would be one with a low thermal expansion coefficient, a high thermal conductivity, and low susceptibility to distortion through thermal spiking. Mirror materials should also be chemically stable.

Glancing incidence optics is generally widely used in synchrotron beamline as an optical element for transportation of x-ray beam as well as for focusing. Glancing incidence optics is

also used in other areas of science and technology to manipulate x-rays for such applications although optics size is bulky.

There are many disadvantages in glancing incidence optics. These are as follows,

- (a) The size of the required mirror is very large (~meter long) due to the large foot print area of the incident hard x-ray beam. Also, the focal length of the mirror becomes very large, usually tens of meters. ($f=R/\delta$, for plano-concave lens where, f is focal length, R is the radius of curvature and δ is the real part of refractive index $\sim 10^{-5}$)
- (b) Optical aberrations such as spherical aberration, astigmatism, and coma become significantly large [29] in that glancing incidence geometry.
- (c) The fabrication of such optical components requires with large size having high precisions in terms of surface roughness, slope, figured etc. The difficulties mentioned above can be overcome by using artificial multilayer (ML) structures, which are discussed in the following sections.

1.3.3 Multilayer (ML) reflective optics:

The x-ray multilayer (ML) mirror is a 1D periodic artificial Bragg's reflector. The ML mirrors are formed by deposition of alternately high-Z and low-Z materials to maximize the electron density contrast at the interface. Layer with high-Z material is called "reflector" and layer with low-Z material is called "spacer". The period (d) of the ML is equal to the sum of the thicknesses of layer A (high-Z) and layer B (low-Z). A schematic representation of a ML structure is shown in figure 1.3.

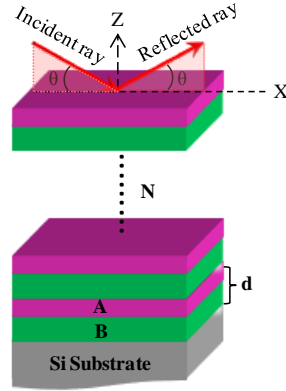


Figure 1.3 Schematic representation of the ML structure. Alternately high-Z layer “reflector” (A) and low-Z layer “spacer” (B) are illustrated to form ML structure. The period, d is the sum of the thicknesses of layers A and B. N is the number of layer pairs.

The periodicity (the thickness of one-layer pair) is maintained as per the applicability at the desired wavelength, e.g., $d=\lambda/2$ for normal incidence condition at wavelength λ . Therefore, the amplitudes of x-rays from successive layer pairs add in phase to give the maximum reflectivity at the Bragg angle due to constructive interference. Generally, in off-normal incidence, the ML optics operates under modified Bragg condition due to refraction corrections [27]

$$2d\sin\theta\sqrt{\left(1 - \frac{4\delta d^2}{m^2\lambda^2}\right)} = m\lambda \quad (1.6)$$

where, θ is measured from the surface, δ is the bilayer weighted real part of the refractive index, m is the order. The details of the numerical calculation of the reflectivity for ML structure can be calculated using dynamical theory (multiple scattering using Parratt formalism) has been discussed in chapter-2 section 2.5.3.

1.3.4 Multilayer (ML) design criteria:

In designing the ML mirror it must be looked into the layer thickness so that the absorption effect is minimized. Therefore, an important parameter is the gamma factor, $\Gamma = \frac{t_{high-Z}}{d}$, the ratio of the high-Z layer thickness to the period thickness for ML fabrication.

The optimized value Γ_{opt} can be written as

$$\Gamma_{opt} \approx \frac{1}{\pi} \left(\frac{3\pi\delta_L\beta_L}{\delta_H\beta_H} \right)^{\frac{1}{3}} \quad (1.7)$$

where, δ_L, β_L are optical constants of low-Z layer and δ_H, β_H are optical constants of high-Z layer, respectively. Generally, the typical value of Γ ranges from 0.3 to 0.45 for low period ML structure [27]. Similarly, the maximum number of contributing layer pairs, N_{max} , depends upon the operating angle of the ML optics as well as the average absorption co-efficient of the two materials in the ML stack at the desired energy of application, Therefore, the maximum number of layer pairs (N_{max}) for ML structure is maintained by the equation

$$N_{max} = \sin^2\theta/2\pi\beta \quad (1.8)$$

Main features in x-ray reflectivity profile from x-ray ML mirror

1. Bragg peaks originate due to constructive interference of the reflected intensities from the periodic interfaces.
2. The Keissig fringes arise between the critical angle and first Bragg peak as well as between two consecutive Bragg peaks are due to interference of reflected intensities from the top of the ML stack and from the interface between top of the substrate and the first layer. So, the Keissig fringes provide information about the total film thickness.
3. Position of Bragg peaks depends on incident photon energy (E) and period (d) of the ML structure. In figure 1.4 (a) and (b), it is clearly illustrated the variation of Bragg

peaks position for W/B₄C ML. Figure 1.4 (a) shows the angle of the Bragg peak position decreases with increasing period thickness. For example, when the period increases from 30 Å to 40 Å the 1st Bragg peak position decreases from 1.5° to 1.13°. In figure 1.4 (b) the reflectivity profile shows that the Bragg peak position also decreases as the incident photon energy increases.

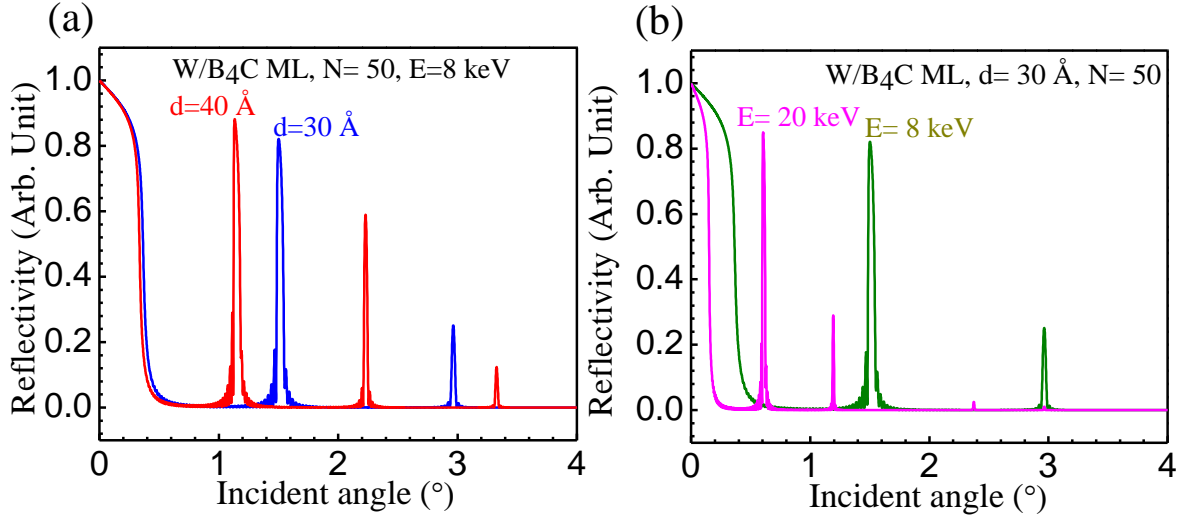


Figure 1.4 Dependence of Bragg peak position on period of ML period as well as on incident photon energy. (a) Calculated reflectivity spectra as a function of incidence angle for two W/B₄C ML having N=50 but varying periods 40 Å and 30 Å at energy 8 keV. (b) Calculated reflectivity spectra as a function of incidence angle for a W/B₄C ML having period 30 Å and N=50 at two different energies 8 keV and 20 keV.

4. Reflectivity (R) of Bragg peak also depends on electron density contrast at the interface ($\Delta\rho$), number of layer pairs (N), interfacial roughness (σ) and layer thickness error. When the electron density contrast at the interface ($\Delta\rho$) decreases the reflectivity decreases as $R \propto (\Delta\rho)^2$ (discussed in figure 1.11). Similarly, as the number of layer pairs increases the reflectivity increases as N^2 initially, thereafter, tends towards to be saturated due to the absorption effect, as shown in figure 1.5. In figure 1.5, the calculated reflectivity is saturated at $\sim N=70$ for a W/B₄C ML with a

period 30 \AA at energy 8.047 keV . In addition, when the roughness decreases the reflectivity in whole profile after the critical angle, thickness error affects both on distributions of peak intensities as well as causes to produce irregularities in Kiessig fringes. The more details about effect of roughness and thickness error are discussed in section 1.3.6.1.

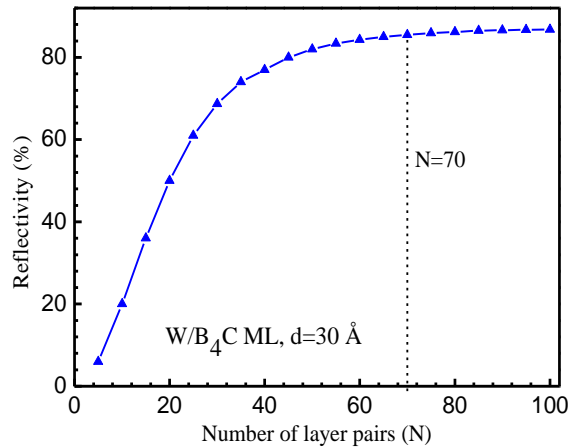


Figure 1.5 Variation of calculated reflectivity as a function of the number of layer pairs for W/B₄C ML with period 30 \AA at energy 8.047 keV . The vertical dotted line represents the number of layer pairs at which the reflectivity saturated.

1.3.5 Advantages of the multilayer optics:

(i) Provide high normal incidence reflectivity for XUV region and high reflectivity above critical angle for hard-rays:

Generally, the reflectivity from a single interface is very low above the critical angle to the normal incidence in the x-ray region. However, the reflectivity can be enhanced at near normal incidence (for extreme ultraviolet/soft x-ray region (XUV)) as well as above the critical angles (up to few degrees for hard x-rays) by fabricating the x-ray multilayer (ML) mirrors. The typical value of normal incidence reflectivity from a single surface lies between 10^{-3} and 10^{-6} in the XUV. For a comparison of normal angle reflectivity of a glancing incidence mirror and a ML mirror in XUV region, the calculated normal angle reflectivity

from a molybdenum (Mo) thin film mirror as well as from a Mo/Si ML mirror in the energy range 60 eV to 195 eV is shown in figure 1.6. It is shown that there is an order of enhancement of the reflectivity with moderate resolution at the Bragg peak of ML mirror (marked by vertical arrow) as compared with thin film mirror.

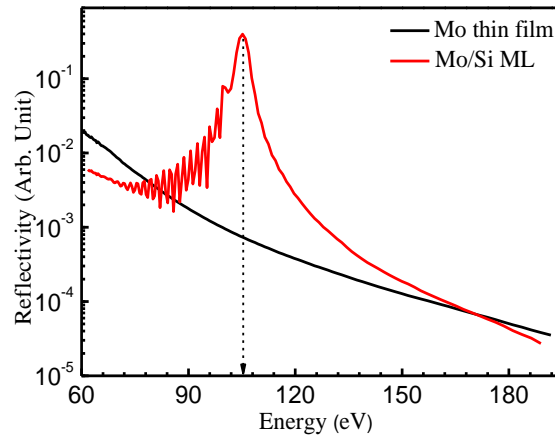


Figure 1.6 Calculated normal incidence reflectivity from a Mo thin film mirror (ideal) and a Mo/Si ML mirror (ideal) having period $d= 60 \text{ \AA}$ and number of layer pairs, $N= 50$ as a function of energy in the energy range 60 eV to 195 eV.

Similarly, for a comparison of hard x-ray reflectivity above critical angle between glancing incidence optics and ML optics, the calculated reflectivity from a Mo thin film mirror (ideal) and a W/B₄C ML mirrors with $d= 3 \text{ nm}$ and $N = 100$ up to first order at the energy 8.047 keV (Cu K_α radiation) is shown in figure 1.7. It is clearly shown that at the first Bragg peak, there is orders of enhancement of reflectivity (shown by dotted line) with moderate resolution ($\Delta\theta=0.05^\circ$) compared with thin film optics.

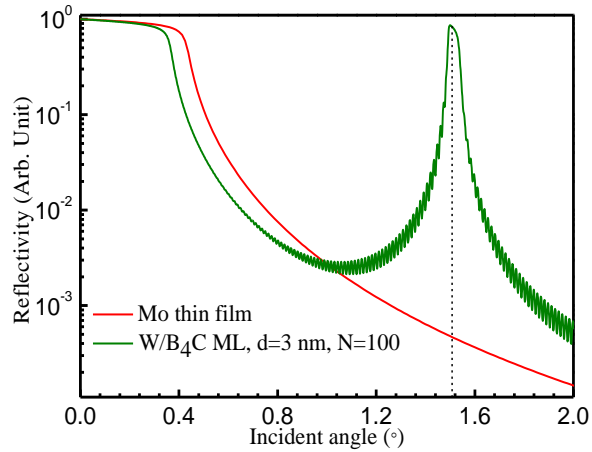


Figure 1.7 Calculated reflectivity profile of W/B₄C ML mirrors with d= 3 nm and N = 100 up to first order at the energy 8.047 keV (Cu K_α radiation).

(ii) Tunability of the ML parameters as well as adoptable with figured surfaces:

The multilayer (ML) structure has also advantages such as tunability of layer the thickness, composition of the layer. So, as per the applicability of the ML optics, one can fabricate ML optics with a constant period ML, varying period along the lateral direction and varying the period along the depth of the ML optics. These can be fabricated according to the desired wavelength region. The depth graded ML is commonly known as super mirror and act as broadband reflector [30, 31]. The lateral graded ML is used as wavelength selector [32].

Another great advantage of the ML optics is that ML mirror can be adapted to contoured surfaces so that focusing and imaging are achieved. A schematic of a ML based fluorescence x-ray microprobe (Krikpatrick-Baez (KB)) using a pair of multilayer coated elliptically configured mirrors to focus incident hard x-ray is shown in the figure 1.8. One mirror is horizontal configured which provides the horizontal focus whereas another is vertically configured which provides vertical focus. Therefore, off-axis spherical aberration significantly reduced by elliptically configured mirrors as compared to the spherical mirror or cylindrical mirror resulting in a small spot size. Thus, it provides the better focussing (few

micron size) of hard x-rays for the desired micro-focussing applications in the synchrotron beamline.

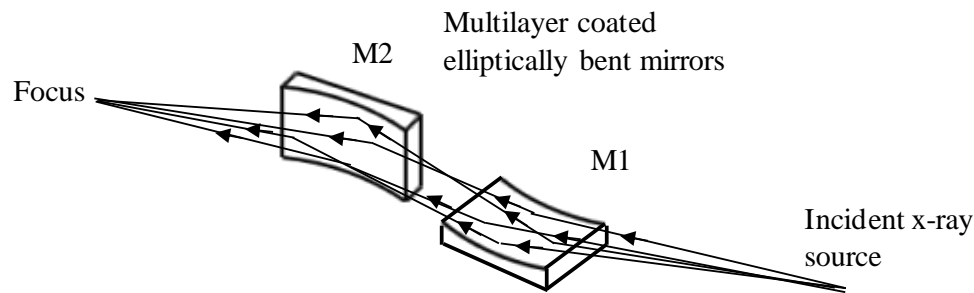


Figure 1.8 Schematic of a fluorescence x-ray microprobe (Krikpatrick-Baez (KB)) using a pair of multilayer coated elliptically bent mirrors to focus incident hard x-ray.

1.3.6 Factors affecting the performance of multilayer mirrors:

The optical performance of x-ray ML structures is affected by several factors such as quality of the interface, thickness error and layer contamination and continuity. The performance of the ML system considering different structural parameters are calculated by IMD coded XOP software package [33]. These are described as follows.

1.3.6 1 Quality of the interface:

The performance of the multilayer structure is strongly affected by the imperfections at the interfaces like roughness, interdiffusion and compound formation. There are two types of roughness. One is low spatial frequency roughness which is generally called “figure error”. This increases the half-width of the focal spot. 2nd is high-frequency roughness which increases diffuse scattering. The high spatial frequency reduces specular reflectivity. The effect of roughness is more for higher q_z values. Generally, the interdiffusion process reduces the optical contrast at the interface which reduces the specular reflectivity. The high spatial frequency physical roughness as well as the interfacial diffuseness generates interface imperfection which causes gradient in the electron density profile instead of abrupt change in electron density profile (ideal). This interfacial imperfection (known as interface width and

also sometime generally called interface roughness) reduces the whole reflectivity profile. A typical example of the effect of roughness on the hard x-ray reflectivity profile calculated for a W/B₄C ML using Parratt's formalism [34] is shown in Figure 1.9. Figure 1.9 shows the reflectivity vs. q_z with different roughness values. It is noted that here the figure is plotted in linear scale to clearly show the effect of roughness on the peak reflectivity (if the plot would be in log scale, then the effect of the roughness on the whole reflectivity pattern would be visible). The profile shows that the peak reflectivity decreases with increasing roughness and the effect is more significant at higher q_z values. It is also clearly observed that the area under the Bragg's peak also decreases with increasing roughness. In figure 1.10 ((a) and (b)), the effect of roughness on reflectivity profile has been calculated for W/B₄C ML with two different periods (23 Å and 40 Å) having fixed N=50. It is clearly illustrated that as the period of the ML mirror decreases, the roughness has more significant effect on the peak reflectivity. The reflectivity of the thin film and ML structure is reduced by the damping factor $e^{-\sigma^2 q^2}$ called Debye-Waller factor [35, 36], where σ and q are the rms roughness of the surface or interface and momentum transfer vector. In other words, a higher tolerance of roughness (achievable smaller values of roughness) is mandatory for the fabrication of low period ML optics.

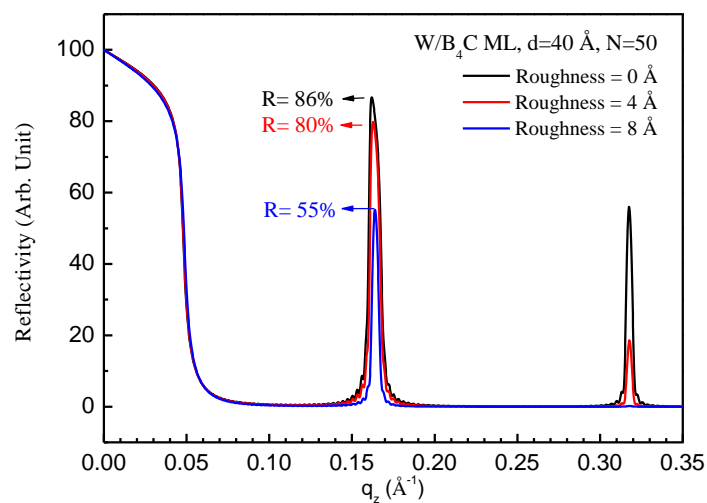


Figure 1.9 The effect of roughness on the reflectivity profile at energy 8.047 keV. The reflectivity is calculated as a function of q_z for W/B₄C ML with period $d=40$ Å and $N= 50$ for three different roughness (0 Å, 4 Å and 8 Å).

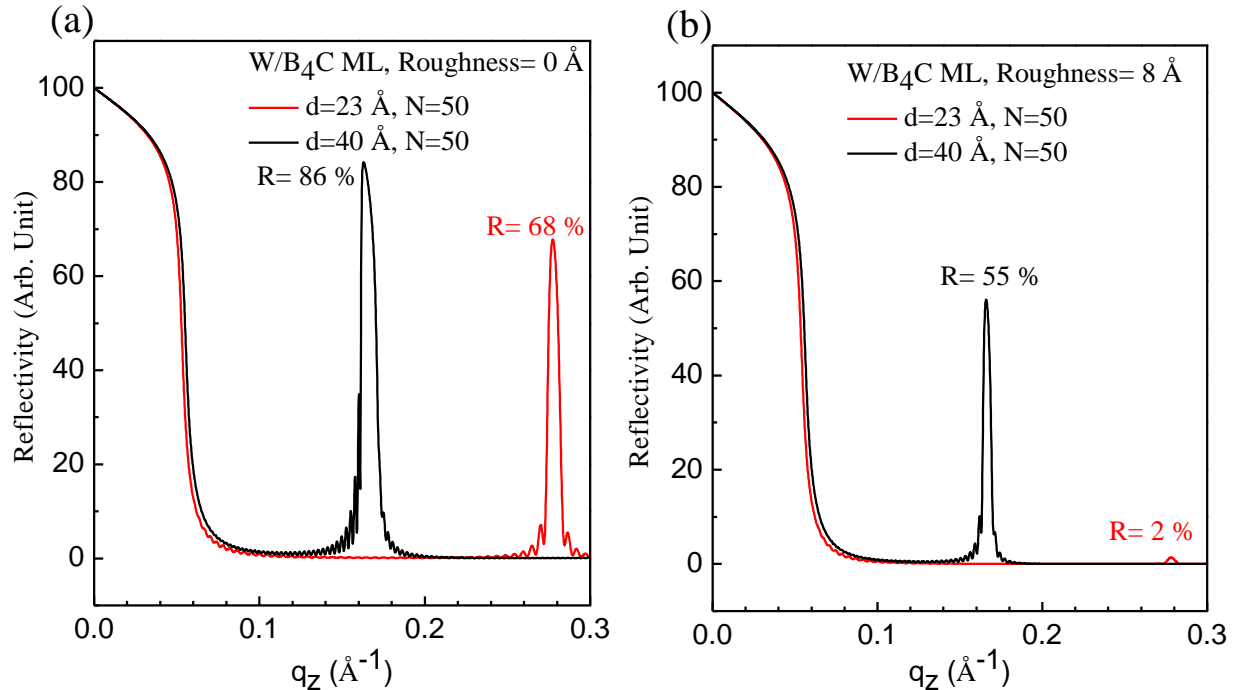


Figure 1.10 Reflectivity vs. momentum transfer vector for two W/B₄C ML with $d= 23$ Å (red line) and $d= 40$ Å (Black line) having fixed $N= 50$ at energy 8.047 keV. (a) Roughness= 0 Å (b) Roughness= 8 Å.

1.3.6.2 Contrast variation:

The reflectivity also strongly depends on the electron density contrast at the interface for a particular ML structure. During the deposition, the layer density may be lower than the bulk density as the thickness of the layer goes to the few angstrom level. As a result, the density contrast at the interface decreases due to uniform intermixing in the layer. It is noted that, a uniform intermixing in a layer resulted in a constant electron density, which we consider as layer. Whereas a non-uniform interdiffusion within interfacial region resulted in non-uniform electron density (also called electron density gradient), which we consider as

interfacial diffuseness, which along with physical roughness decreases reflectivity, as it is discussed earlier. Again, when the individual layer thicknesses are very small, the electron density contrast decreases due to the interdiffusion process. The effect of the reduction of the electron density contrast is illustrated in figure 1.11 for W/B₄C ML. It shows that the reflectivity decreases with decreasing density contrast at the interface.

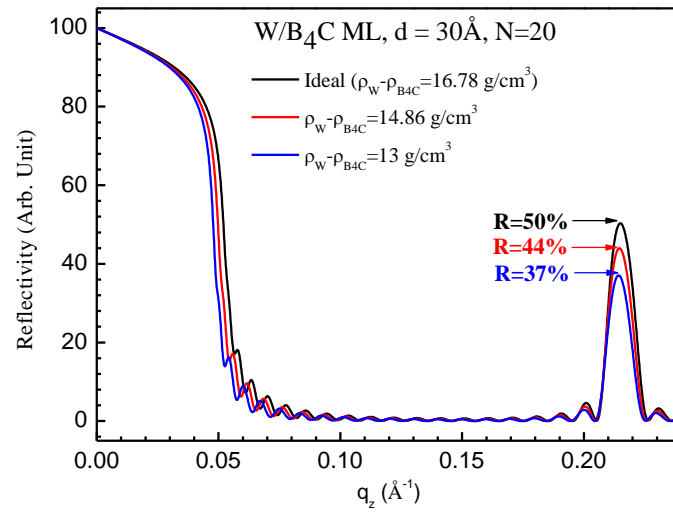


Figure 1.11 The effect of electron density contrast on reflectivity profile is calculated at energy 8.047 keV for W/B₄C ML with period 30 Å and N=20. Black line represents the ideal density contrast ($\rho_W - \rho_{B4C} = 16.78 \text{ g/cm}^3$), Red line represents density contrast ($\rho_W - \rho_{B4C} = 14.86 \text{ g/cm}^3$), Blue line represents density contrast ($\rho_W - \rho_{B4C} = 13 \text{ g/cm}^3$).

1.3.6.3 Thickness error:

The amplitudes of the reflected beam from a periodic ML structure add in phase to give maximum reflectivity at the Bragg angles when the ML structure is perfectly periodic. For a ML structure with N number of layer pairs, there is N-2 number of regular Kiessig oscillations between successive Bragg peaks. But in reality, the thickness of each layer in that ML structure randomly changes by a very small amount. This might occur during film deposition. In a real ML structure with random thickness error, the spacing in the Kiessig

oscillations between Bragg peaks becomes irregular, and the width of the Bragg peaks increases. The thickness errors also can be derived from the width of the Bragg peaks [37]. The effect of the random thickness errors on the reflectivity profile for W/B₄C ML at 2.5 % random thickness error is shown in the figure 1.12. Therefore, it is careful to control deposition parameters during the deposition of the ML structure, so that the random thickness error gets minimized.

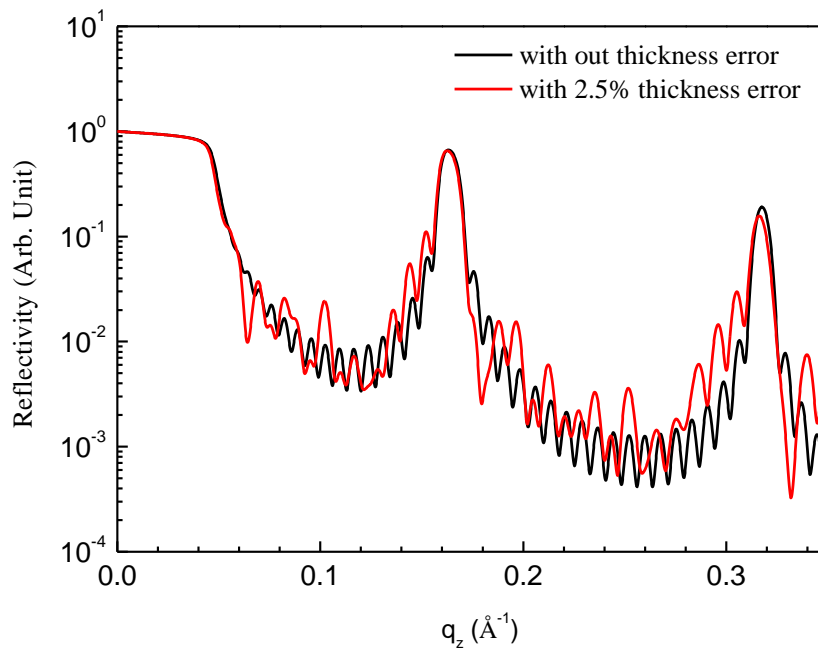


Figure 1.12 The effect of thickness error on reflectivity profile calculated at energy 8.047 keV for W/B₄C ML with period 40 Å and N=20. Black line represents without effecting random thickness error and Red line illustrates the effect of 2.5% random thickness error.

1.3.6.4 Layer Contamination and Continuity:

When a pure layer is contaminated by impurities, its optical response (refractive index changes) changes. Further, the presence of impurities can alter the structure in the nano-scale range due to formation of alloy and compound. Therefore, the change in optical properties of the layer as well as change in structure from the desired value affects the reflectivity at the wavelength for which the ML is designed [38]. In addition, for a real ML structure, its layer must be continuous [39] with sharply defined boundaries, which results in large contrast in

refractive index at the boundaries, yielding maximum reflected amplitude. When a ML structure is exposed to the ambient condition, the top surface of the ML structure may have contaminated by the impurities, which modulated its electron density profile. As a result, the reflectivity profile gets modulated near to the critical angle. The presence of the top contaminated layer on ML structure can be inferred by observing the oscillations in the reflectivity profile between critical angle and 1st Bragg peak (see the figure 6.2 in chapter-6).

1.3.6.5 Effect of the Residual stress:

Besides the aforementioned factors, the residual stress is also another critical factor that has the destructive effect on ML optics. For example, high residual stresses can cause cracks and buckle in films. It also reduces the angular or spectral resolution and peak intensities by increasing the width of the reflectivity peak. [25] Again, due to the effects of high residual stress, ML can become unstable over time and peel off from the substrate. [26] Thus, it is desirable to fabricate ML optics with low residue stress for the device application.

1.3.7 Application of the ML optics:

A summary of the advantages of ML optics (as discussed earlier in sec. 1.3.5) would facilitates to discuss about it's wide applications. X-ray ML optics manipulates x-rays for its wide technological applications, e.g., in synchrotron beamline, plasma diagnosis, x-ray lithography, astrophysics and nuclear technology etc. As we know, the ML mirror is an artificial periodic structure, so it has the following advantages: (i) Layer thickness, composition can be tailored as per the desired energies spanning from extreme ultra violet to soft gamma-rays, (ii) Importantly, ML optics can be fabricated on the figured surfaces for focusing and imaging applications in telescopes & microscopes, (iii) It provides higher near normal reflectivity in extreme ultraviolet/soft x-ray region with moderate spectral band pass, (iv) It operates relatively larger incidence angle compared to thin film glancing angle optics in the hard x-ray region, so that it decreases numerical apparatus, decreases aberration and

reduces the size of optics, and provide a monochromatic beam and so on. In this section some of these important applications are briefly described as follows:

1.3.7.1 X-ray focusing and microprobe optics:

X-ray ML optics extensively used as focusing optics in fluorescence microprobe. A pair of elliptically curve multilayer coated mirrors is used to focus 8- 20 keV x-ray to a 1 μm diameter spot size [40]. One mirror provides horizontal focus while other provides the vertical focus in the Kirkpatrick-Baez (KB) optics configuration. For that application, the length of the optics size can be reduced significantly by using ML coated KB optics because Bragg angle is a number of times larger as compared to the critical angle for total external reflection. Also, ML optics is extensively used in the soft x-ray microscope to image the biological samples in the “water window” region (between C – and O- K edge) [41].

1.3.7.2 Polarimetry:

Based on the reflection effect near the 45° incidence angle, the multilayer optics offers a powerful tool for controlling and measuring polarization properties of the radiation in EUV and soft x-ray region [42-45]. This particular incidence is called Brewster’s angle. The reflectivity of the p-polarized radiation (the electric field lying in the plane of incidence) is either zero or minimum (in case β is not zero) at Brewster’s angle. At that same incidence angle, the reflectivity of s-polarized radiation becomes very high. ML optics used at Brewster’s angle for a linear polarizer in the extreme ultra violet regions. To generate linear polarization towards soft x-ray region, one requires ML mirror with a very ultra-short period. Different studies have been reported to use ultra-short period ML as quarter-wave in the transmission mode for analysis of polarization characteristics in soft x-rays. Recently, a simple design of a soft x-ray polarimeter using ultra-short period ML mirror has been reported for astronomical observations [46]. Ultra-short period W/B₄C based transmission

MLs are used for polarization analysis of the soft x-rays [47, 48]. Further, astronomical x-ray polarimetry is one of the last windows which is poorly explored [49].

1.3.7.3 Extreme ultraviolet/soft x-ray Astronomy:

The ML optics is also used in EUV and x-ray astronomy. Distant stellar objects e.g., neutron stars, emit an enormous amount of soft x-rays. Their spectral properties afford the information about the production mechanism of radiation, magnetic field strength etc. Multilayer-coated normal incidence optics is used to obtain high-resolution astronomical images for these purposes.

1.3.7.4 Soft gamma-ray energy band selector:

Recently ML optics finds applications as reflective optics for the high energy range in the soft gamma-rays (100 to 600 keV) range to advance its scientific and technological applications in the emerging frontier areas of both nuclear physics [9, 18] as well as high energy astrophysics [19, 20]. For example, the detection of the gamma-ray signal from the distant stellar objects is a challenging task due to the weak gamma-ray signal as compared to the background noise signal. For these applications, grazing incidence ML optics is used as a narrow energy band selector to suppress the background noise signal.

1.3.8 Importance of the ultra-short period multilayer optics:

MLs with ultra-short period operate at higher incidence angle for desired energies. Because of higher operating angles, it provides higher resolution. It also increases numerical apertures important for the focusing and imaging application [21, 22]. However, the fabrication of such ultra-short period ML mirror is a challenging task. This is because, to realize all these technological applications, the period thickness of the ML must be controlled to the shortest possible desired value with the structural perfection at the atomic level. The

main hindrance in attaining the ultimate shortest period is the limitation imposed by minimum thickness needed to form a continuous layer of homogeneous density (*continuous limit*) which depends on the material and its growth. It requires a proper understanding of the film microstructure to produce a continuous layer at the shortest thickness in Volmer-island growth mode [50, 51]. All these aspects required advancement of thin film technology to produce ML structure with high precision and control of layer thickness, better understanding of layer microstructure and physics & chemistry of formation of interfaces to produce atomically smooth interfaces with high optical contrast.

For the development of ultra-short period ML optics at the desired energies, at first, it is required to choose the appropriate material combinations with suitable optical properties to understand the chemical stability of the structure and structural perfection in the tolerable range. Therefore, it is important to develop efficient ML optics having a smooth chemically stable interface, good optical contrast, and structural stability for long term application. For soft gamma-ray spectroscopy application, it is also required a suitable material combination of ML optics which provides higher photon flux to improve the signal-to-noise ratio particularly for high energy astronomy as well as nuclear technology applications. This is due to the weak gamma-ray signals from distance stellar objects as well as from remnant radioactive substances in nuclear spent fuel compared to the background signal. Based on these aspects W/B₄C material combination is selected for soft gamma-ray application which is broadly described in the chapter-6. To develop ML mirror for the soft gamma-ray optics, W/B₄C ML mirrors are designed and developed with varying period $d = 1.86- 1.23$ nm at a fixed number of layer pairs $N = 400$ to operate at the glancing incidence (few miliradian to several miliradian) to cover energy range 100-500 keV.

1.3.9 Multilayer optics for the soft gamma-ray spectroscopy:

In the past decade, the utility of ML reflective optics has been gradually extended towards further higher energies i.e., in the energy range of soft gamma-ray (100-600 keV). Astronomical observations in the soft gamma-ray energy range are being enabled with coded-aperture telescopes such as those on INTEGRAL [52] and Swift [53]. Recently, ML coating is also used to advance the astronomical telescope [54]. In nuclear physics, the ML reflective optics is used to detect remnant radioactive isotopes in nuclear spent-fuel. The direct measurements of gamma-rays signal emitted from spent-fuel materials are a high risk task for the safeguard community. This is because, the weak signal of the characteristic radiation of the radioactive materials get lost in the strong background radiation. Therefore, it poses a challenge how to measure the amount of radioactive materials present in the spent fuel. Previously, several groups demonstrated that K-shell fluorescence lines of U and Pu from spent fuel could be detected with high-purity germanium (HPGe) detectors by the use of grazing incidence multilayer mirrors by reducing the background rate and minimizing the dwell time of the measurement [55, 56]. A schematic of the experimental set-up for detecting nuclear spent fuel using ML mirror as shown in figure 1.13. There is a beam conditioning elements (e.g., collimator) between the source and the ML mounting goniometer. There is a beam stopper at the direct beam. The detector is placed at the reflected beam position, such that it doesn't expose to direct beam.

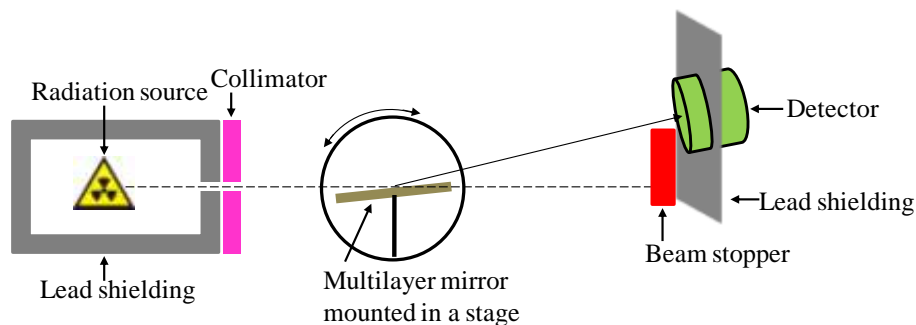


Figure1.13 Schematic of the experimental arrangement of gamma-ray signal from nuclear spent fuel with the use of ML mirror.

Thus, in the soft gamma-ray spectrometer application, the challenges are higher requirements of efficient optics to deliver sufficient amount of photon flux to improve signal-to-noise ratio because of the weak signal strength of emitted gamma-rays from distance stellar objects as well as remnant radioactive isotopes in nuclear spent-fuel. Therefore, it requires an optically suitable better material for ML mirror which provides both high peak reflectance as well as high integrated reflectance. Previously, Perea *et. al.* [9] demonstrated the WC/SiC ML optics with periods in the range 1-2 nm and number of layer pairs 300-500. They evaluated the reflectivity of WC/SiC based soft gamma-ray ML optics ($d= 1.474$ nm, $N= 300$) with actual beam divergence 0.024 mdeg. Subsequently, 1st Bragg peak reflectivities are measured ~ 52.6 % at energy 384 keV (with $\Delta E = 3$ keV) and ~ 23 % at energy ~ 378 keV (with $\Delta E = 9.8$ keV). On that basis, in this thesis, W/B₄C ML optics has been demonstrated by fabricating with varying period $d = 1.86- 1.23$ nm at a fixed number of layer pairs $N = 400$. Here, metal based (W/B₄C) based ML optics is chosen to provide higher photon flux owing its higher optical contrast than the corresponding metal carbide counterpart if the structural parameters of the metal-based ML could be tailored to obtain the achievable values and comparable with the later one. The more details about the choice of materials and methodology have been discussed in the chapter-6. Now, from the beginning of this chapter it was mentioned that the probing and understanding the physics and chemistry interface formation and controlling the interface width in nano-scaled layer structure is vital for improving underlying optical performance of the ML structure. In this connection, we have work on a novel methodology/analytical technique for better understanding of physics and chemistry of buried layer using resonant soft x-ray reflectivity (**R-SoXR**) which is

discussed briefly in the following section. In addition, residual stress in ML structure is also discussed.

1.4 Resonant soft x-ray reflectivity (R-SoXR):

The conventional hard x-ray reflectivity (HXR) is an important non-destructive technique which is used to probe the surfaces and interfaces in thin film and multilayer structures. It is well known that electrons are responsible for the interaction of x-rays with matter. In fact, the x-rays probe effective electron density, which is directly allied to the refractive index. Generally, the incident photon energy is far away from the absorption edge (of materials in the sample) in conventional HXR technique. In addition, using the conventional HXR technique, it is difficult to probe buried interfaces and to determine the layer composition if optical contrast between the elements present in thin film/ML is not sufficient (less than 5 %). In this thesis (chapter-3), a novel approach is developed to address this low contrast physics problem by combining the resonant soft x-ray reflection spectroscopy at grazing incidence close to the “critical angle” with angle dependent reflection at energies in the region of the corresponding absorption edges to precisely quantify spatio-chemical depth profile. Resonant x-ray reflectivity is an important non-destructive technique which precisely probes the spatio-chemical structure from free to buried interfaces in thin film and MLs. Near the absorption edge, the interaction of the incident x-ray photon and the electron undergoes through a strong variation due to significant variation of optical constants. The significant variation of optical constants modulates the reflectivity profile which contains the information about the spatial variation of the resonating elements. The chemical compositional information is investigated by tuning the energy near the respective absorption edges and the spatial depth profiling is investigated by using angle dependent reflection spectroscopy at the absorption edges. We demonstrated that resonant x-ray reflectivity is a

unique powerful technique for quantitative depth profiling of both microstructure and spectroscopic information from free surface to the buried interfaces.

Previously, the resonant soft x-ray reflectivity (R-SoXR) has been used for characterization of the polymeric & organic films near C K-edge [57, 58], ion distribution at the bio-mimetic membranes [59], ionic liquid [60], electronic and structural analysis of the inorganic surface layer and the thin films [61-63], the magnetization in magnetic structures [64], proximity effect at the cuprate/manganate interfaces [65] and ordering in the correlated electron systems [66] etc. However, it is complicated to extract unique real-space information in order to achieve an element specific chemically and spatially resolved depth distribution profile in a straightforward way in more complex interface structures. The very poor electron density contrast at the interface with unknown interfacial atomic diffusion at different extents, chemical changes and the presence of impurities leads to complicated interfacial structures. It requires a proper understanding of the real and imaginary parts of scattering factor for modelling the scattered length density. In this thesis, an approach has been demonstrated to overcome this difficulty together with spectral dependent reflection spectroscopy apparently to determine interfacial profiles. All the R-SoXR performances are carried out at BESSY-II synchrotron source in the s-polarization geometry using the Optics Beam line [67]. The developed technique enables precisely to reconstruct spatio-chemical interfacial map in a non-destructive manner up to tens of nanometre thickness within a few atomic percent.

1.5 Residual stress:

The residual stress of the ML structure is an important factor that reduces the long-term performance of the ML optics. The residual stress is primarily related to the thin film ML stability i.e. peeling, cracking and curling of the films. It also reduces the peak intensity

by increasing the width of the reflectivity peak and reduces the angular resolution. Therefore, it is necessary to understand the evolution of the residual stress in the ML structure and how it relates to the microstructure of the ML structure. So, what is residual stress? The residual stress is defined as the stress that is present in a substance or thin films/multilayer (ML) structures in the absence of any external force or load. The origin of residual stress in the thin films or multilayer structures depends on the various factors such as deposition process and process parameters, growth mechanism, morphology and structural parameters etc [24]. Generally, nano-scaled thin film or multilayers are grown in Volmer-Weber (VW) growth mode which leads to a polycrystalline or amorphous structure. The different stages of the VW growth mode are nucleation, island growth, island-island coalescence to form larger islands, establishment of large area contiguity and forming the continuous layer. The island growth structure is one of the causes to generate compressive residual stress. The residual stress would be compressive or tensile that also depends on growth process. For example, in sputtered deposited film, the compressive residual stress is generated due to atomic peening process [68]. The interfacial stress between the adjacent layers is very important for ultra-short period MLs. The type of the interfacial stress depends on the material combination. For example, compressive interfacial stress is observed in the sputtered deposited Ag/Ni [69], Ag/Cu [70] ML films. On the other hand, a tensile interfacial stress is observed in sputtered Cu/Cr ML [71].

In this thesis, to determine the residual stress in the W/B₄C MLs two measurement techniques have been used as (a) substrate curvature method using laser Fizeau interferometer and (b) GIXRD based $\sin^2\chi$ method using synchrotron (details of the methods are described in chapter-2). The substrate curvature method provides information about the total residual stress in the film, whereas the GIXRD method is used to measure the residual stress of layers separately for one type of material (here only in W layers) which should be crystalline

structure through variations of lattice spacing. This is because sputtered deposited W layers are formed in polycrystalline structure and B₄C layers are formed as amorphous structure. A comprehensive stress-structure correlation analysis is done on W/B₄C ML by systematically varying thickness of the individual layer, and number of layer pairs.

1.6 Aim and Scope of this thesis:

In layered structured nano-scale periodic ML mirror, the understanding of physics and chemistry of interface formation is an important aspect apart from growth of such structure for improving underlying optical performances of such ML optics. In addition, the optical performance is also affected by another factor, called residual stress. Therefore, the central issue of this thesis is to understand the microstructure of the layers at early stage of growth, spatio-chemical interfacial map, the evolution of the residual stress and its correlation with the microstructure in the MLs and finally the development of the ML optics for soft gamma-ray application. Understanding of these physics issues are important aspect for development of high efficient ML reflective optics for such high energy gamma-rays. The main thesis works are followed as

1. A novel approach to study surface interface science of nano-scaled layered structure materials
2. Understanding the evolution of residual stress with varying microstructure in nano-scaled W/B₄C MLs.
3. Study of residual stress-microstructure correlation in ML mirrors with large layer pairs.
4. Development of W/B₄C multilayer (ML) reflective mirror for potential application in soft gamma-rays.

1.6.1 A novel approach to study surface interface science of nano-scaled layered structure materials:

Nano-scaled layered structured films have broad range of application in material science owing to its unique optical, structural, electronic, magnetic and superconducting properties. These properties are strongly affected by the spatial and chemical distributions of elements and presence of impurity across the underlying interfaces. Therefore, it is important to understand precisely chemically- and spatially-resolved atomic profile across the interface to improve the quality of the films. In order to study that, a novel approach is demonstrated here to precisely probe spatio-chemical structural phenomena in nano-scaled layered structure materials. This methodology is developed by the combination of resonant soft x-ray reflection spectroscopy at grazing incidence close to the “critical angle” with angle-dependent reflection at energies in the region of the corresponding absorption edges. The developed approach is demonstrated on the nano-scaled layered structure of C (20Å)/B (40Å)/Si (300Å)/W (10Å)/Si substrate. At first, different chemical states of elements are investigated qualitatively by using the glancing incidence reflection near respective absorption edges (K-edges of B, C and O; and L-edge of Si) with different incident angles near critical angle. Simultaneously, near edge x-ray absorption spectra are measured to support the validity of the reflection spectra. After that, angle dependent resonant soft x-ray reflectivity measurements were performed to precisely quantify the spatio-chemical depth profile.

1.6.2 Understanding the evolution of residual stress with varying microstructure in nano scaled W/B₄C MLs:

The residual stress in x-ray multilayer (ML) plays important role in the performance of x-ray optics. It has destructive effect on the optical properties of the ML optics. Thus, in order to achieve low residual, it is essential to understand the evolution of the residual stress as well as its correlation with microstructure. Therefore, the details of residual stress and its

correlation with microstructure have been studied near the onset of formation of continuous layer with systematically varying individual layer thicknesses, important for ultra-short period W/B₄C ML optics. In order to investigate that, the residual stress is determined by varying the individual layer thickness from ~ 0.4 nm to 2.9 nm keeping fixed number of layer pairs, N= 20. The total residual stress is measured by substrate curvature method, whereas the residual stress in W layers is determined separately by using synchrotron based GIXRD method. The HXR and the diffuse scattering techniques are used to analyse microstructure for the correlation of the stress-structure, and is discussed.

1.6.3 Study of residual stress-microstructure correlation in ML mirrors with large layer pairs:

ML optics for soft gamma-rays requires a larger number of layer pairs (few hundred). So when the number of layer pairs becomes large, residual stress in such ML optics plays important role in the long term stability of the ML optics. So, it is important to understand and evaluate the variation of the residual stress with the number of layer pairs, which has been undertaken in this chapter. Here, the residual stress is studied in W/B₄C MLs with varying N = 20- 400 with a fixed low d value at ~1.9 nm. In addition, the variations of the residual stress with varying the period of multilayer at a fixed number of layer pairs are also studied. In this case, the residual stress is analysed by varying period d = 1.9-1.23 nm at a constant N =300.

1.6.4 Development of ML reflective optics for soft gamma-rays:

Recently, the ML optics finds its application in soft gamma –ray spectroscopy in the energy range (100 - 500 keV). For this application, a highly efficient ML optics is required to deliver higher photon flux. In this chapter, the metal based W/B₄C ML optics is demonstrated as high efficient ML reflective optics for the potential energy range 100-500 keV. The ML mirror is produced by precisely controlling the microstructure at the ultrathin limit and

tailoring for low interfacial width to obtain high optical contrast. The ML mirrors are designed and developed with varying period $d = 1.86 \text{ nm}-1.23 \text{ nm}$ at a fixed $N = 400$. Presently, due to unavailability of soft gamma-ray reflectometer in India, the optical performances are measured in the energy range 10-20 keV using synchrotron, which is easily available. Considering the measured structural parameters of MLs and well agreement of the measured optical properties with theoretical values in the hard x-rays, the optical properties are predicted in the soft gamma-ray energy range considering extrapolated known optical constants. This is the well adopted method of accurately predicting reflectivity performance at first order Bragg peak of ML reflectivity mirror in the soft gamma-ray region. The results of the predicted optical performances in the soft gamma-rays have been discussed.

Chapter-2

Experimental details:

In this chapter, the working principle of the different experimental techniques used for the fabrication of thin films and multilayers, and their characterizations are briefly described. At first, the experimental techniques for the fabrication of thin film and multilayer (ML) samples using the electron beam evaporation system and the magnetron sputtering system are briefly described. Thereafter, the characterization techniques such as x-ray reflectivity (XRR), x-ray diffuse scattering in rocking scan mode, resonant soft x-ray reflectivity (R-SoXR), near edge x-ray absorption spectroscopy (NEXAFS), transmission electron microscopy (TEM), residual stress measurements using substrate curvature method, and grazing incidence x-ray diffraction (GIXRD) are described briefly. The methodology of the related data analysis has also been discussed here.

2.1 Introduction:

Modern fabrication techniques allow materials to be designed and fabricated for thin film and multilayer (ML) at the atomic and molecular level. Knowledge of such various deposition techniques enables us to deposit good quality of ultra-thin films with the desired thickness. In the present thesis, the thin film and ML structure are synthesized using Volmer-Weber growth [72] mode by electron beam evaporation system [73, 74] and magnetron sputtering system [75, 76]. Therefore, it is important to understand these deposition techniques more in detail and also the various characterization techniques which are used to characterize the thin film and ML structures. Structural parameters of the films (such as thickness, interface width and density etc) are probed in the non-destructive methods using x-ray scattering based complementary techniques such as hard x-ray reflectivity (HXR) and diffuse scattering measurement using rocking scan mode. The spatio-chemical depth profile from free to buried interfaces is probed by resonant soft x-ray reflectivity (R-SoXR) along with near edge x-ray absorption spectroscopy (NEXAFS). The details of the NEXAFS have been discussed in the section 2.5.6. It is also important to study the residual stress, because residual stresses have a destructive impact on the film. So the total residual stress of the film is determined by using the substrate curvature method where as $\sin^2\chi$ method based on grazing incidence x-ray diffraction (GIXRD) is used for the determination of stress of crystalline layers of the individual type of material. Transmission electron microscopy (TEM) measurement has also been performed to obtain the structural image of ML to correlate with the structure determined through HXR. Finally, optical performances of the developed ML mirrors are measured using synchrotron-based hard x-ray reflectivity.

2.2 Fabrication of thin films and multilayers (MLs):

Generally, thin films are fabricated by physical processes and chemical processes. In the physical process, the direct atom/molecules of the material are made to be deposited on the substrate. Whereas in the chemical process, the chemical compound of the material which to be deposited is used as a precursor. Then, the material is deposited due to chemical decomposition of the precursor on the surface of the substrate by chemical reaction. In the physical vapour deposition method, the materials are deposited on substrate either evaporation technique or sputtered technique. If the lattice parameters of the substrate do not match with the lattice parameters of the material to be deposited, then the film grows under the Volmer-Island growth mode [72]. Generally, optically suitable materials of thin films and multilayer involved in the present study for x-ray/soft gamma-ray optics are not lattice matched with the substrate and hence grow in Volmer-island growth mode. Generally, the thermal evaporation, electron beam evaporation, sputtering process (DC/RF/magnetron/ion beam), pulsed laser deposition, chemical vapour deposition etc [77-79] are used to fabricate thin film and ML samples. In the present work, the thin film is deposited by electron beam evaporation system [74] and ML is deposited by magnetron sputtering system [76]. The electron beam evaporation and magnetron sputtering technique have their own advantages and disadvantages for the fabrication of thin films and ML. Magnetron sputtering system is favourable for the fabrication of ML samples with a larger number of layer pairs because the sputtered film is produced comparatively smoother and denser due to the higher kinetic energy of ad-atoms and plasma stability over a longer interval of time (~12-30 hrs). Fabrication of a multilayer mirror for soft gamma rays, which requires a larger layer pairs ~300-500 is difficult using the evaporation technique. This is because to maintain a stable deposition rate to ensure thickness control on the angstrom level within the ML stack is difficult due to thermal drift in quartz crystal.

2.3 Electron beam evaporation system:

In the present work, thin films of C/B/Si/W are deposited on Si substrates by electron beam evaporation system (e- beam system) [74]. The e-beam system consists of two 6 kW Telemark guns, one gun has 3 pockets with 15 cm³ crucible and the other has 4 pockets 7 cm³ crucible. In this method, a high energy electron beam (electron gun supply voltage ~ 7.5 kV DC, the emission current ranges from few tens of mA to few hundred mA) is used to evaporate source materials. Electrons are emitted from a hot filament (tungsten filament) and accelerated toward the source materials to evaporate the material. Due to the collision of the electron with source material the kinetic energy of the electron generates heat in the material. The energy of the evaporated particles is in the order of 0.2 eV to 0.5 eV. A schematic arrangement of the electron beam evaporation instrument is shown in figure 2.1.

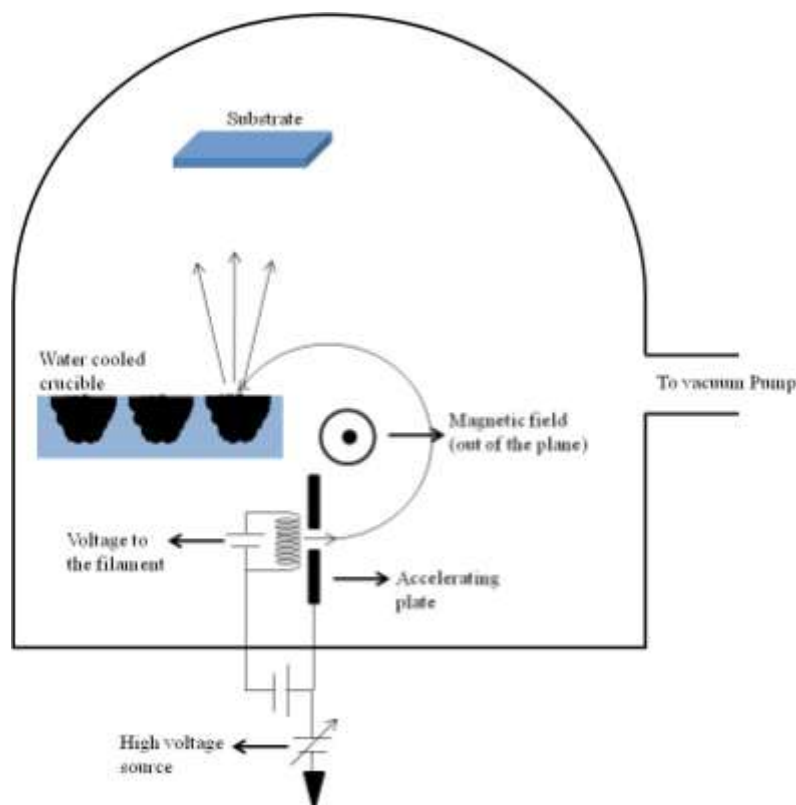


Figure 2.1 Schematic of the electron beam evaporation instrument.

The electron beam is directed by the magnetic deflection system by bending 270° into the source material on the copper crucible. To prevent contamination of the deposited materials with Cu crucible as well as the melting of the crucible, the Cu crucible is cooled by water. The main chamber is pumped through two large sizes (1500 litre/sec) turbo-molecular pumps (TMP) which are followed by two rotary pumps. The base pressure of the main chamber is attained $\sim 3 \times 10^{-8}$ mbar. The load-lock chamber is pumped by a turbo molecular vacuum pump with speed 250 litre/sec followed by a rotary pump of speed $15 \text{ m}^3/\text{hour}$. The thickness of the film is monitored by a quartz crystal couple with Inficon (IC-5) controller. Multiple materials have been deposited sequentially using multiple pockets crucibles.

2.4: Magnetron sputtering system:

In the sputtering technique [78, 79], the target material is bombarded by accelerated ions (like inert Argon gas ion) which are produced by glow discharge. Then the sputtered target atoms are ejected and deposited on the substrate due to the energy transfer from accelerated ions to the target atoms. The target atoms are ejected when the kinetic energy of the bombarded ion is higher than the surface binding energy of the target atom. The energy range of the sputtered atoms is $\sim 1\text{-}10$ eV which is sufficient to provide the required surface mobility of sputtered atoms to form a smoother and dense film. The main advantages of the magnetron sputtering technique are (a) high deposition rate, (b) variable kinetic energy of the sputtered particles to provide required surface mobility of the adatoms, (c) good adhesion to the substrate, and (d) stoichiometric film [80]. The “sputtering yield” i.e. the average number of ejected atoms from the target materials per incident ion depends on the surface binding energy of the atoms in the target, the ion incident angle, the energy of the ions, the masses of the target atoms and ions. Generally, the sputtering process happens by using DC or RF power supply. RF supply is used for the deposition of insulating material to remove the space charge difficulty by DC supply. In the magnetron sputtering system the magnetic field is

applied perpendicularly to the electric field that helps to spiral around the electrons in the magnetic field lines. Therefore, the rate of collisions and ionization are increased. As a result, the application of the magnetic field increases the deposition rate at low operating pressure and temperature. Therefore, the magnetic sputtering system grows high quality films at a lower pressure ($\sim 10^{-3}$ mbar). In the present thesis, W/B₄C MLs have been deposited by DC and RF (frequency 13.6 MHz) magnetron sputtering system [76]. A photograph of the magnetron sputtering system is shown in Figure 2.2. It has two vacuum chambers, the main deposition chamber and the load-lock chamber. The main deposition chamber is rectangular and its volume is $\sim 800 \times 325 \times 770$ (length \times width \times height) mm³. The length and diameter of the cylindrical load-lock chamber are ~ 920 mm and ~ 130 mm, respectively. There are two rectangular cathodes (W and B₄C) of size 500 mm \times 100 mm each. The purity of W and B₄C targets are 99.9 % and 99.99 %, respectively. The main chamber and load-lock chamber are pumped by directly connecting to two turbo-molecular pumps having speeds 1800 litre/sec and 250 litre/sec. The ultimate base pressure in the main chamber and load-lock chamber are typically at $\sim 3 \times 10^{-8}$ mbar and $\sim 8 \times 10^{-8}$ mbar respectively. High purity (99.9995%) argon is used as sputtering gas with a fixed flow rate of 12 sccm. DC power and RF (13.56 MHz) power are used for sputtering of W target and B₄C target, respectively. The warm-up time was kept at 600 seconds to ensure stable plasma before the start of each deposition run.



Figure 2.2 Photograph of magnetron sputtering system in our laboratory used for the fabrication of W/B₄C multilayer mirrors.

2.5: Characterization techniques:

In this section, various characterization techniques have been discussed for studying structural properties, spatio-chemical depth profile, and structure-optical properties correlation of thin films and multilayers (MLs). The structural properties are like the thickness of the film, the period of the multilayer (ML), the roughness of the interface, the correlation length of the interface. Apart from the structural parameters, the spatio-chemical depth profile is determined by resonant soft x-ray spectroscopy. In addition to that, the substrate curvature and GIXRD techniques are discussed for residual stress analysis.

2.5.1: X-ray reflectivity:

One of the most important non-destructive techniques is the x-ray reflectivity technique. This is widely used to measure the structural parameter of the buried thin-film and ML. This technique extracts the information about thicknesses, surface interface roughness, and optical behaviour of buried layers. Since the x-ray reflectivity (XRR) technique has been used as a routinely measurement technique for the structural analysis of thin films and

multilayers in this thesis, therefore, here XRR technique has been discussed more in details.

The reflectivity of thin film and multilayer is calculated from Fresnel equations [35].

When x-ray beam falls on an interface between two mediums, the x-ray beam is reflected and refracted at the interface is shown in the figure 2.3.

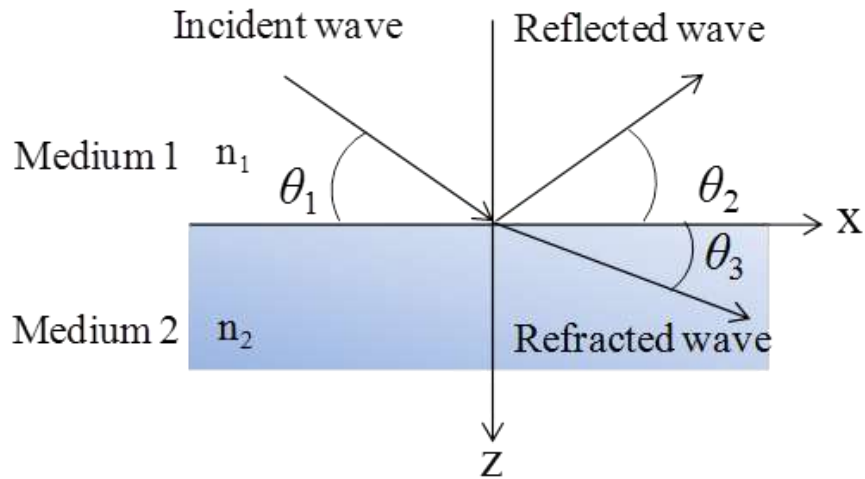


Figure 2.3 Reflection and refraction of x-ray beam from surface/interfaces.

Let us consider a plane electromagnetic wave (k_1) incident from the vacuum on a substance at an angle θ_1 . Then the incident wave reflected at an angle θ_2 and refracted at an angle θ_3 from the interface between the two mediums. The amplitude of the reflected and transmitted wave can be written as

$$r^s = \frac{n_1 \sin \theta_1 - n_2 \sin \theta_2}{n_1 \sin \theta_1 + n_2 \sin \theta_2} \quad (2.1)$$

$$r^p = \frac{n_1 \sin \theta_2 - n_2 \sin \theta_1}{n_1 \sin \theta_2 + n_2 \sin \theta_1} \quad (2.2)$$

$$t^s = \frac{2n_1 \sin \theta_1}{n_1 \sin \theta_1 + n_2 \sin \theta_2} \quad (2.3)$$

$$t^p = \frac{2n_1 \sin \theta_1}{n_2 \sin \theta_1 + n_1 \sin \theta_2} \quad (2.4)$$

where n_1, n_2 are the refractive indices of the medium 1 and medium 2, respectively. r^s, r^p, t^s, t^p are the reflected and transmitted amplitude of the s and p polarised x-ray beam. The reflected amplitude can be written by using the momentum transfer vector, $q = \frac{4\pi n \sin \theta}{\lambda} = 2k_z$ along the normal direction.

$$r^s = \frac{q_1 - q_2}{q_1 + q_2} = \frac{k_{1z} - k_{2z}}{k_{1z} + k_{2z}} \quad (2.5)$$

The reflectivity is written as

$$R = |r^s|^2 = \left| \frac{q_1 - q_2}{q_1 + q_2} \right|^2 \quad (2.6)$$

For x-ray the refractive index, n of a material is given by the expression as

$$n = 1 - \delta + i\beta = 1 - \frac{r_e}{2\pi} \lambda^2 N_a (f_1 - if_2) \quad (2.7)$$

$$\delta = \frac{r_e}{2\pi} \lambda^2 N_a f_1 \quad (2.8)$$

$$\beta = \frac{r_e}{2\pi} \lambda^2 N_a f_2 \quad (2.9)$$

where, δ and β are optical constants of the material, r_e is the Thomson scattering length, N_a is atomic number density (atoms per unit volume). f_1 and f_2 are the real and imaginary part of the atomic scattering factor.

Now the reflectivity has been calculated for thin film and multilayer by using Fresnel reflectivity in specular condition (see next sections 2.5.2 and 2.5.3). The specular condition means that the angle of reflected beam and the angle of incident beam are equal and also the reflected intensity is confined to the plane of incidence.

2.5.2: Reflectivity from single thin film:

The specular reflectivity from a single thin film has been discussed here. At first, a finite thickness of a single layer film is deposited on the substrate. There are two interfaces as vacuum/film interface and film/substrate interface. The incident beam is now successively reflected and transmitted from the two interfaces which form a geometrical progression series to give the actual reflectivity expression shown in figure 2.4. Let us consider the Fresnel's reflection amplitude from the vacuum/film interface and film/substrate interface are r_{01} and r_{12} and the film thickness is t . Therefore, the actual reflectivity from the single layer thin film is

$$R = \left| \frac{r_{01} + r_{12} \exp(iqt)}{1 + r_{01} r_{12} \exp(iqt)} \right|^2 \quad (2.10)$$

where $q = 2k_1 \sin \theta_1$

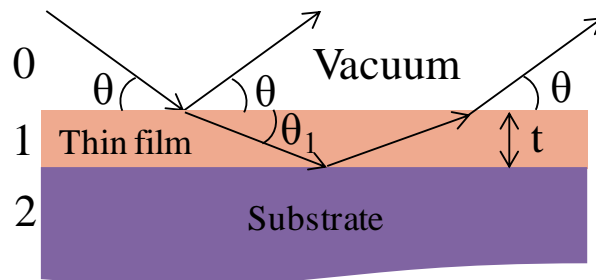


Figure 2.4 Reflection and transmission of x-ray beam from a slab of finite thickness t .

2.5.3: Reflectivity from Multilayer (ML) film:

The expression of the reflectivity of a multilayer (ML) structure can be calculated from Parratt recursive formalism [34] by considering Fresnel reflection from the interfaces. Here it is considered that the multilayer structure is composed of N layers deposited on an infinitely thick substrate, as shown in the figure 2.5. According to the formalism the N^{th} layer

deposited directly on the substrate. The refractive index each layer is $n_j = 1 - \delta_j + i\beta_j$ and thickness is t_j . It is found that

$$k_{z,j}^2 = (n_j k)^2 - k_x^2 = (1 - \delta_j + i\beta_j)^2 k^2 - k_x^2 \approx k_x^2 - 2\delta_j k^2 + i2\beta_j k^2 \quad (2.11)$$

Now the wave vector transfer, q_j of the j^{th} layer is

$$q_j = 2k_j \sin\theta_j = 2k_{z,j} = \sqrt{(q^2 - 8k^2\delta_j + i8k^2\beta_j)} \quad (2.12)$$

The reflectivity of each interface (in absence of multiple reflections) is obtained from Fresnel's equation as

$$r_{j,j+1}^* = \frac{q_j - q_{j+1}}{q_j + q_{j+1}} \quad (2.13)$$

The reflectivity from the interface of the bottom layer and the substrate is

$$r_{N,\infty}^* = \frac{q_N - q_\infty}{q_N + q_\infty} \quad (2.14)$$

The reflectivity from the top of the N^{th} layer can be written as

$$r_{N-1,N} = \frac{r_{N-1,N}^* + r_{N,\infty}^* \exp(iq_j t_j)}{1 + r_{N-1,N}^* r_{N,\infty}^* \exp(iq_j t_j)} \quad (2.15)$$

which allows the multiple scattering and refraction in the N^{th} layer. It is clear that the process is recursive to get total reflectivity from the vacuum/layer interface to the N^{th} layer/substrate interface.

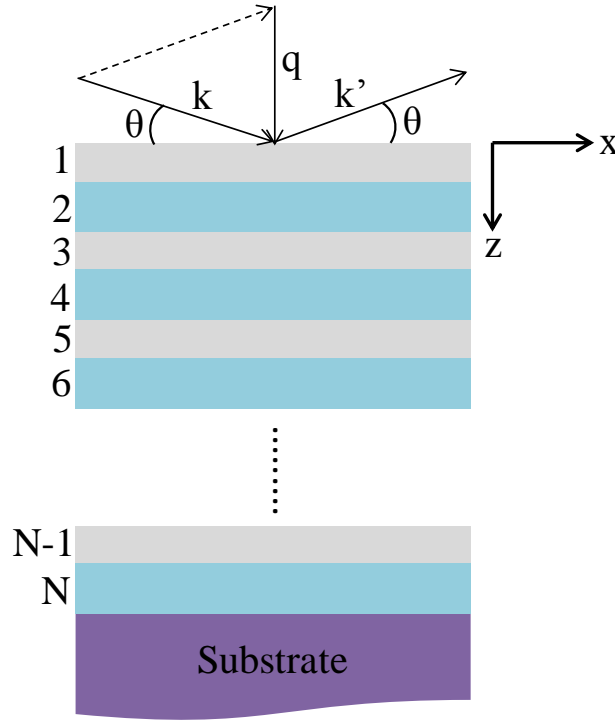


Figure 2.5 Schematic of a multilayer which consists of a stack of bilayers.

In real thin film and multilayer structure, the surface and interface are not perfectly smooth and there is some finite width due to imperfections such as roughness, interdiffusion, chemical reaction. The imperfections at the interface reduce the actual specular reflectivity. The density variation at the interface between two rising layers creates a density gradient which also reduces the reflectivity. The reflectivity of the thin film and ML structure is reduced by the damping factor $e^{-\sigma^2 q^2}$ called Debye-Waller factor [35, 36], where σ and q are the rms roughness of the surface or interface and momentum transfer vector. For multilayer structure the momentum transfer vector, q changes from q_j to q_{j+1} in the layer j^{th} to $(j+1)^{\text{th}}$ layer due to the change of refractive index from one layer to another. The change of the momentum transfer vector is included in that model given by Nevot and Croce [81]. The q^2 is replaced by the geometrical average $q_j q_{j+1}$ for the interface between j^{th} and $(j+1)^{\text{th}}$ layers. As the incident angle changes, the momentum transfer vector propagates in the normal direction to the sample surface. Therefore, the information about the lateral surface morphology is not

extracted from specular reflectivity measurement. That can be determined from diffuse scattering measurements (see section 2.5.4).

The hard x-ray reflectivity (HXR) measurements in the thin film and ML samples are performed using a Bruker D8 Discover x-ray diffractometer. In this diffractometer, the x-ray source used is a Philips x-ray tube of Cu target (1600 watt). The monochromatic beam (Cu K_{α}) is generated by using a two bounce Ge (222) monochromator. The incident beam slit is kept fixed at 0.1 mm and the detector slit is fixed 0.3 mm during the HXR measurement. The angular divergence of the incident beam is 0.005° . The HXR performances were carried out in θ - 2θ geometry. Thus by fitting the HXR profile of thin film and ML gives the estimation of the structural parameters. The “IMD” coded “XOP” software package [33] and Parratt software package [34] have been used to fit the HXR profiles. The best fit results are obtained by using non-linear list square fitting algorithm.

2.5.4: X-ray diffuse scattering in rocking scan geometry:

XRR measurement using hard x-ray provides information about roughness i.e. total interfacial width at the interface (σ). The physical roughness (σ_r) and interfacial diffuseness (σ_d) are related to the total interfacial width or roughness as $\sigma = (\sigma_r^2 + \sigma_d^2)^{1/2}$. It is important to understand and distinguish the contribution of each component to the total interfacial width. To separate the physical roughness from total interfacial width the x-ray diffuse scattering measurements were performed in rocking scan (ω scan) geometry. In addition, to extract the information about the lateral surface morphology, the correlation lengths (in-plane correlation length and the perpendicular correlation length) are also determined from the diffuse scattering measurement. Originally, the theoretical aspect of diffuse scattering reflectivity is proposed by Sinha *et al.* [82]. After that, the theory has been again developed by Stearns *et al.* [83], Spiller *et al.* [84] and Holý *et al.* [85] to modify the

power spectral density or the intrinsic roughness of each interface by introducing a vertical correlation function across the depth of the multilayer through a replication factor. Depending on two different angular regions the theoretical development of diffuse reflectivity from thin film, multilayer or bulk surface [86] is established by considering two approximations: (a) Born Approximation (BA) (applicable at a higher grazing incidence angles where multiple reflections is ignored) and (b) Distorted Wave Born Approximation (DWBA) (valid near critical angle).

In this thesis, the diffuse scattering spectra of W/B4C MLs were analyzed by the formalism proposed by Windt *et al.* [87]. In this formalism, each interface structure is expressed by the Power Spectral Density (PSD) function given as

$$PSD(q_{\parallel}) = \exp(-z/\xi_{\perp}) \frac{4\pi H \sigma_r^2 \xi_{\perp}^2}{(1+|q_{\parallel}|^2 \xi_{\parallel}^2)^2} \quad (2.16)$$

Where q_{\parallel} , σ_r , ξ_{\parallel} and H are the component of the momentum transfer vector in the surface or interface of the ML sample, physical roughness of the interface, in-plane correlation length in the interface and jaggedness factor, respectively. The vertical correlation length between the two interfaces i^{th} and j^{th} ($i^{\text{th}} > j^{\text{th}}$) is defined as ξ_{\perp} and can be written by the relation

$$C_{ji} = \exp\left(-\sum_{n=j}^{i-1} \frac{t_n}{\xi_{\perp}}\right) \quad (2.17)$$

Where t_n is the thickness of the n th layer. The 1st order Distorted Wave Born Approximation (DWBA) expressed the diffuse scattering reflectivity expression by considering interdiffusion (σ_d). The detailed expressions have been derived by Stearns [83]. The fitting of the diffuse scattering reflectivity profiles has been done by considering the fixed thickness and densities of each layer obtained from HXR measurements. The jaggedness factor (H) has been taken as 1 for all the MLs during fitting. The detailed explanation of this assumption is discussed elsewhere [88].

X-ray diffuse scattering performances are performed by a Bruker D8 Discover x-ray diffractometer (Cu K_α) in rocking scan geometry. The diffuse scattering measurements are performed for each ML in rocking scan geometry where the scattering angle 2θ adjusted at 1st Bragg peak position. Also, the angle of incidence was altered from 0° to 2θ°. The measured spectra were fitted using the “IMD” code “XOP” software package [33].

2.5.5: Resonant soft x-ray reflectivity (R-SoXR):

Resonant soft x-ray reflectivity (R-SoXR) is an important powerful technique used to probe the interfacial phenomena for the quantitative depth profile of spatio-chemical structure from surface to buried interfaces. At the absorption edges, x-ray reflectivity exhibits a resonant behaviour due to the strong variation of the atomic scattering factor. This happens due to the anomalous behaviour of the optical constants near the absorption edges [89]. The optical constants of the material can be derived from the semi-classical forced oscillatory model. In the semi-classical model, a bound multi-electron atom considers as a collection of harmonic oscillators with its own resonance frequency. The bound electrons are oscillated in simple harmonic motion by the incident electric field in presence of the restoring force of the nucleus. Therefore, the equation of motion of each bound electron can be written as [27]

$$m \frac{d^2x}{dt^2} + m\gamma \frac{dx}{dt} + m\omega_s^2 x = -eE_i \quad (2.18)$$

Where the first term in the above equation comes due to acceleration, the second term is the dissipative force term, the third term is due to the resonating force of an oscillator with resonance frequency ω_s , γ is the damping constant, E_i is the incident electric field. By considering incident electric field as $E_i = E_0 e^{-i\omega t}$, the displacement of each bound electron can be written as

$$x(t) = \frac{1}{\omega^2 - \omega_s^2 + i\gamma\omega} \frac{eE_i}{m} \quad (2.19)$$

And the acceleration of each bound electron can be written as

$$a(t) = \frac{-\omega^2}{\omega^2 - \omega_s^2 + i\gamma\omega} \frac{eE_i}{m} \quad (2.20)$$

Then the dipole moment, $P = \rho_e \alpha E_i$, comes due to the displacement of each bound electron.

where α is the polarizability, ρ_e is the free electron density. Therefore, the dielectric constant

becomes as $\epsilon = 1 + 4\pi \frac{P}{E_i}$ and the refractive index, the square root of dielectric constant is

given by the equation [27]

$$n(\omega) = 1 - \frac{\lambda^2 r_e N_a}{2\pi} \sum_{s=1}^Z \frac{g_s \omega^2}{\omega^2 - \omega_s^2 + i\gamma\omega} \quad (2.21)$$

Where λ is the incident wavelength, r_e denotes the classical electron radius, N_a is the number

density of atoms. Z corresponds to atomic number, g_s is the oscillator strength, i.e. the

number of electrons with a resonance frequency ω_s such that the sum of oscillator strengths is

equal to the total number of electrons $\sum_s g_s = Z$ according to the semi-classical model. The

scattering phenomenon is shown in the figure 2.6.

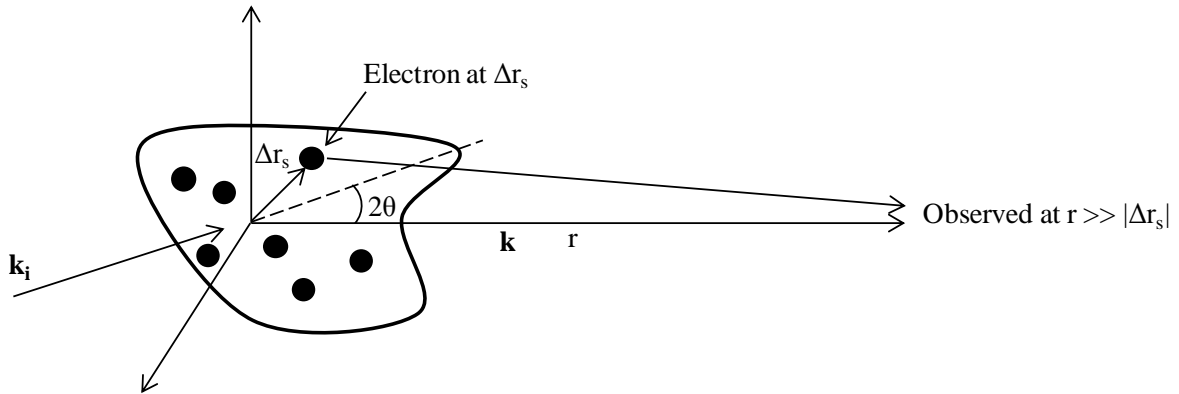


Figure 2.6 Schematic of the scattering phenomenon of a many-electron atom with incident radiation.

Each of the oscillatory electrons radiates electromagnetic wave in the same frequency. The electric field scattered by the multi-electron atom is written as [27]

$$E(r, t) = \left(\sum_{s=1}^Z \frac{g_s \omega^2 e^{-iq \cdot \Delta r_s}}{\omega^2 - \omega_s^2 + i\gamma\omega} \right) \times \left(-\frac{r_e}{r} (E_i \sin\Phi e^{-i\omega(t-r/c)}) \right) \quad (2.22)$$

Where r is the position vector, Φ is the angle between the E_i and the scattered wave vector k and q is the change in momentum transfer vector.

Now from equation 2.22, the complex atomic scattering factor is defined as

$$f(q, \omega) = \sum_{s=1}^Z \frac{g_s \omega^2 e^{-iq \cdot \Delta r_s}}{\omega^2 - \omega_s^2 + i\gamma\omega} \quad (2.23)$$

Thus the atomic scattering factor is the effective number of electrons that take part in the scattering phenomenon. It is noted that the term, $q \cdot \Delta r_s$ is the phase variation of the scattered field due to the variation the electronic position.

The phase term in equation 2.23 can be written as

$$|q \cdot \Delta r_s| \leq \frac{4\pi \sin\theta}{\lambda} a_0 \quad (2.24)$$

Where a_0 is the Bohr radius. The phase term can be simplified in two special cases as:

$$|q \cdot \Delta r_s| \rightarrow 0 \text{ for } \frac{a_0}{\lambda} \ll 1 \text{ (Long wave length limit)}$$

$$|q \cdot \Delta r_s| \rightarrow 0 \text{ for } \theta \ll 1 \text{ (Forward scattering)}$$

Depending on the above two cases (long wavelength limit and/ or forward scattering condition) the atom can be taken as a point that gives the in-phase scattered radiation. Also, the complex atomic scattering factor can be written as

$$f^0(\omega) = \sum_{s=1}^Z \frac{g_s \omega^2}{\omega^2 - \omega_s^2 + i\gamma\omega} \quad (2.25)$$

Again it can be simplified as [89]

$$f(q, \omega) = f_0(q) + f_r(\omega) + if_i(\omega) \quad (2.26)$$

Where, $f_0(q)$ is the real part of the atomic scattering factor related to the free electrons (Thompson scattering phenomena), $f_r(\omega)$ (dispersion term) is also real part of the atomic scattering factor and $f_i(\omega)$ (absorption term) is the imaginary part of the atomic scattering factor. Both $f_r(\omega)$ and $f_i(\omega)$ are associated with bound or resonating electrons and are called the resonant (or anomalous) term of the atomic scattering factor. Both the $f_r(\omega)$ and $f_i(\omega)$ terms become significant with comparing $f_0(q)$ when the incident photon energy near the absorption edge. If the incident photon energy close to the atomic resonance energy, the corresponding core electron response is affected by their binding to the nucleus. The photons produce real and virtual transitions in which they are absorbed and re-emitted.

The insight of the physical picture of the anomalous scattering factors can be explained by the semi-classical approximation of the photon scattering from the bound electrons. If the incident photon energy is more than the binding energy of the electrons (so-called free electrons), they contribute to the polarization which is out of phase of the incident photon (Thompson scattering model) [27]. If the incident photon energy is less than the binding energy of the electrons, the polarization attributed to these electrons is in phase. This leads to the sign reversal of the real part of the atomic scattering factor. Depending upon the amount of out-of-phase component of polarization with respect to the in-phase, the amount of sign reversal occurs. So the strong resonance occurs at the edge. The details of the theory of the resonant atomic scattering factor based on a multiple-scattering approach have been studied by Benfatto *et al.* [90]. The tabulated values for the atomic scattering factor (calculated and experimental, for some elements) for all the elements $Z=1-92$ in the energy range 50 eV to 30 keV have been given by the Henke *et al.* [28]. They measured f_2 from

transmission measurements and determined (f_0+f_r) using the Kramers-Kronig relation. The refractive index is written as $n = 1 - \delta + i\beta$. Where, δ and β are the optical constants which are related to the atomic scattering factor as

$$\delta = \frac{r_e}{2\pi} \lambda^2 N_a (f_0(q) + f_r(\omega)) \quad (2.27)$$

$$\beta = \frac{r_e}{2\pi} \lambda^2 N_a f_i(\omega) \quad (2.28)$$

N_a is the number of atoms per unit volume, r_e is the Thompson scattering length.

The technique is generally applicable to any systems with respective absorption edges such that for a specific energy one can show the unique features in order to increase the contrast and the rest of the other are flat. Thus, the spatio-chemical distributions in the film are quantified by using R-SoXR measurement at the respective absorption edges. The performance of R-SoXR measurements has been performed in s-polarization geometry by the Optics Beamline [67] at the BESSY-II synchrotron source. The energy resolution of the beamline is $E/\Delta E \approx 2000$ near the B K edge. The angle dependent soft x-ray reflectivity performance recorded with varying angle up to 89.2° by using a GaAsP-photodiode with an acceptance area of $4 \times 4 \text{ mm}^2$ at 310 mm away from the measure thin film sample. The absorption data are recorded simultaneously in conjunction with spectral dependent reflectivity. R-SoXR spectra are fitted by using Parratt formalism [34].

2.5.6: Near edge x-ray absorption spectroscopy (NEXAFS):

The different chemical states in the layer structure have been identified by the near edge x-ray absorption spectroscopy (NEXAFS) in C/B/Si/W/Si substrate. The soft x-ray absorption measurements were performed near the B, C and O K-edges and Si L-edge in the total electron yield (TEY) mode at Optics Beamline [67] of the BESSY-II storage ring. NEXAFS spectra are measured at 45° near the respective edges. The total electron yield can

be defined as the total number of electrons emitted from the sample (n_B) per incident photons, N_0 and can be written in the current mode as

$$\chi_c \frac{n_B}{N_0} = [1 - R(\omega, \theta)] \frac{\eta\omega}{2\Sigma} \frac{1}{\sin\xi} \mu(\omega)L \quad (2.29)$$

where $R(\omega, \theta)$ corresponds to the reflection coefficient, $\mu(\omega)$ denotes the linear absorption coefficient, θ is a grazing incidence angle, ξ denotes the grazing refraction angle. Σ is average energy required to generate a secondary electron which is capable of escaping in the vacuum from the photocathode, $\eta\omega$ is incident energy of the photon, $L = \frac{1}{\alpha}$ denotes the effective electron scattering length, which is largely determined by the mean free paths α of the secondary electrons and is, to first order, independent of the photon energy. The formula (equation 2.29) is valid only when $\mu(\omega) \ll \frac{1}{L}$. This reveals that one can consider as $\chi_c(\omega) \approx \omega\mu(\omega)$ at the range of large grazing incidence angle [$1 - R(\omega, \theta) \approx 1$].

2.5.7: Transmission electron microscopy (TEM):

Transmission electron microscopy (TEM) [91] is a powerful analytical technique in material science. In the present thesis, it is used to visualise and analysed the layer by layer structure in ML mirror. In TEM, the testing object is illuminated by a high energy electron beam and a transmitted/diffracted beam is observed, which gives the information about the structure through the formation high resolution image. The TEM has a high energy electron gun with the tungsten filament. The electrons are emitted from the gun by applying high voltage 100-500 keV. The electrons are focussed and magnified by the simple coil, quadruple, or hexpole lenses. Generally, four stages of lenses exist in the TEM, which are condenser lenses, the objective lenses, the intermediate lenses and the projector lenses respectively. The electron beam is focussed on the sample by the condenser lens, and the

magnified objective image is formed by an objective lens followed through the intermediate lens. Finally, the image is expanded on to the fluorescent screen by the projector lens.

Generally, the sample preparation is more complex and takes more time for TEM measurement. At first, two film/substrate specimens with dimension of $10 \times 5 \text{ mm}^2$ (length \times width) are used to be attached front to front with glue for sample preparation. Then the sample is inserted into a copper tube with the outer diameter $\sim 3 \text{ mm}$ by reducing the sample size to $8 \times 2.5 \times 2.5 \text{ mm}^3$ (length \times width \times height) by mechanical polishing on the emery paper. After that, disk-shaped samples are mechanically produced by cutting and grinding, and ultimately the samples are thinned $\sim 60\text{-}80 \text{ }\mu\text{m}$ thin by Ar ion thinning. The energy of Ar ion beam gradually lowered from 5 keV to 2 keV when the samples turn into thinner. The high resolution image of the sample is recorded using the bright field imaging mode after the sample preparation. The denser region with higher atomic numbers will absorb more electrons and produce a darker image whereas regions with low density, low atomic numbers and no sample will produce a bright image. In the present thesis, the cross-sectional TEM measurement of W/B₄C MLs has been performed using a Philips CM 200 transmission electron microscope, operated at 200 keV. The thickness measurement of each layer was performed using GATAN Micrograph software.

2.5.8: Residual stress measurement:

There are several experimental methods available for measuring residual stress in thin films/ML mirror. For the present thesis, the total residual stress in W/B₄C ML has been measured by the substrate curvature method using Zygo Mark-II laser Fizeau interferometer [92, 93]. The residual stress in the W layers is estimated by using grazing incidence x-ray diffraction (GIXRD) based $\sin^2\chi$ method.

2.5.8.1: Substrate curvature method:

The substrate curvature method is usually used to determine the stress within films and MLs coated on the substrate. The deposition of a film or ML can bend the substrate. The changes in the curvature of the substrate after film or ML deposition make it possible to calculate variations in stress. Therefore, the substrate curvature method is one of the most important techniques for measuring total residual stress in the film without taking any knowledge of film mechanical properties such as biaxial elastic modulus, Poisson's ratio etc. So the residual stress in the film is determined in a thin stressed film deposited on a thick substrate, using the substrate curvature by the Stoney's equation [94, 95] as follows:

$$\sigma = \frac{1}{6} \left(\frac{E_s}{1-\nu_s} \right) \left(\frac{1}{R_a} - \frac{1}{R_b} \right) \left(\frac{t_s^2}{t_f} \right) \quad (2.30)$$

Where, R_a and R_b are the radii of curvature of the substrate after and before ML deposition respectively, E_s is Young's modulus of the substrate and ν_s is Poisson's ratio of the substrate, t_s and t_f are the thickness of the substrate and film respectively and satisfy the condition $t_s \gg t_f$. In the present thesis, the Si substrate is used and the thickness is 0.5 mm. The values of E_s and ν_s are 165 GPa, 0.22, respectively [96]. In the substrate curvature method, the isotropic homogeneous stress distribution is considered in the deposited film and the deformation of the film is small compared to the substrate thickness. Here, the negative stress is considered as compressive stress and the positive stress is tensile stress. A schematic diagram of the substrate curvature method using laser Fizeau interferometer is shown in the figure 2.7

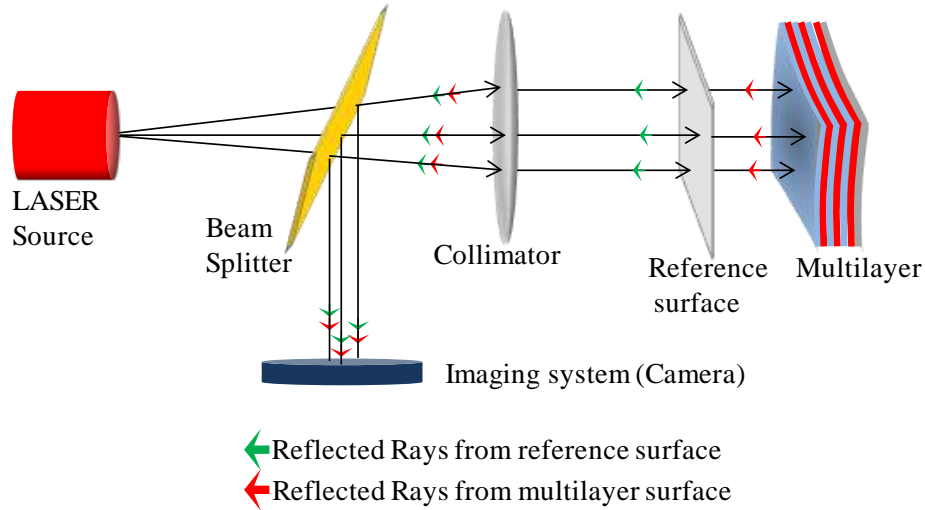


Figure 2.7 Schematic of the Zygo Mark-II laser Fizeau interferometer set-up for experimental arrangement.

A well collimated He-Ne laser (wave length (λ) = 632.8 nm) source was used as the source beam in the interferometer set-up. The flat reference surface reflects some of the incident laser light back into the interferometer set-up and forms a reference wave front. The remaining part of the laser light passes through the reference flat surface to the test sample surface and reflected back by the test sample surface to form the test wave front. After that, the two wave fronts interfere with each other. The phase difference between the two wave fronts results in an image of light and dark fringes. The interference pattern is transformed into electrical signals by a CCD camera through software analysis. Consequently, the computer takes several “snapshots” of the interference pattern using CCD. These snapshots are processed by the computer through software analysis to resolve the phase of the wave front at each point on the interference pattern using Zernike polynomial fitting analysis [97-99]. The surface shape profile function $Z_r(x_r, y_r)$ can be expressed as the linear combination of the different polynomials $F_j(x, y)$ and the coefficient A_p

$$Z_r(x_r, y_r) = \sum_{p=1}^m F_p(x, y) A_p \quad (2.31)$$

Where r denotes the sample index. The profile is fitted to a polynomial set by considering the least-square fitting procedure [100]. Then the spherical shape profile was extracted from the surface profile data fitting analysis for determining the radius of curvature of the substrate. The average radius of curvature (R) has been calculated from the curvature profile using the equation

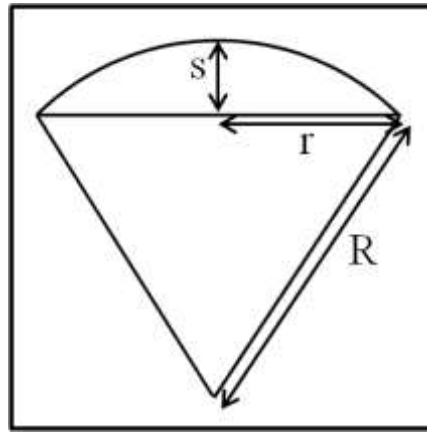


Figure 2.8 Drawing of the radius of curvature measurement from the spherical surface profile.

$$R = \frac{r^2}{2s} + \frac{s}{2} \quad (2.32)$$

where r is the radius of the circular substrate surface that is illuminated by the laser source. s is the sag in the spherical shape curvature of the surface profile. The figure 2.8 shows the schematic of the radius of curvature measurement. The interferometer appoints the phase shifting method for wave-front analysis. This confirms the exactness of the measured surface profile to be better than $\lambda/10$ (i.e., $0.063 \mu\text{m}$). It is noted that the curvature method is quite insensitive to small errors on the original substrate shape because the method is based on the change of the substrate shape before and after coating. Almost flat substrates (flatness $\sim 1\lambda$ ($0.6 \mu\text{m}$)) is selected for the residual stress determination. The error in measured total residual

stress was determined by taking into account the error measurement of curvature, substrate thickness, and film thickness.

2.5.8.2: GIXRD based $\sin^2\chi$ method:

Generally, the x-ray diffraction (XRD) method measures the residual stress due to the elastic deformation of the material. If the residual stress exists in the material, usually two effects happen on the measured diffraction pattern - (a) the diffraction peak shift and (b) peak broadening. Therefore, it is possible to obtain the inter-planer spacing/ diffraction peak position of the diffraction plane by using Bragg's law from this measurement and the inter-planer spacing/ diffraction peak position will be different from that of the stress-free state. From that diffraction peak shift, the residual stress can be calculated by the XRD method.

For thin film or ML samples, the GIXRD technique is used to determine the residual stress. This is because the GIXRD is a surface sensitive technique and beam covers a large surface area of the sample leading to a large structural contribution from the test sample at grazing incidence. In the present thesis Grazing incidence x-ray diffraction (GIXRD) based $\sin^2\chi$ method has been used to determine average in-plane residual stress in W layers of W/B₄C ML mirrors using the synchrotron source. Here, only residual stress in W layers is determined because of the w layers are formed as polycrystalline in nature and the B₄C layers are formed as amorphous structure. In this method, it is possible to get a number of diffraction peak positions from a particular diffraction plane with different χ angle rotation. The schematic of the experimental arrangement is shown in the figure 2.9.

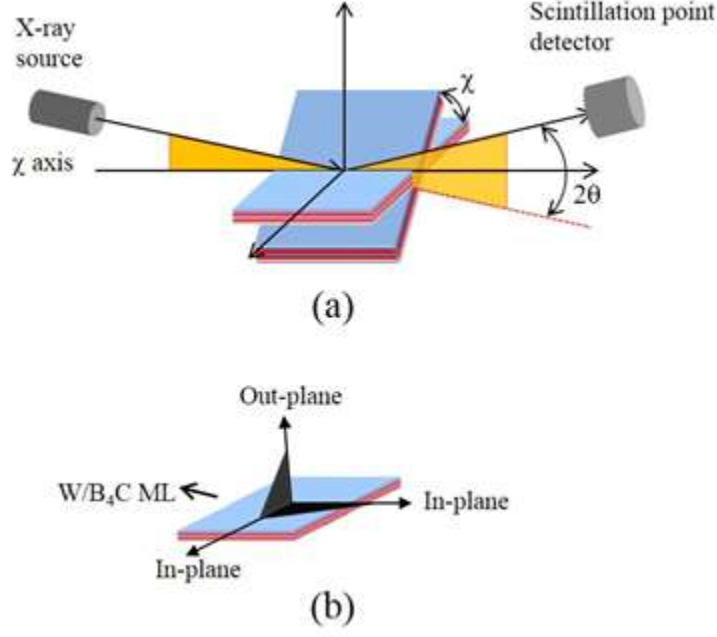


Figure 2.9 (a) Schematic diagram of GIXRD method for residual stress measurement. (b) In-plane and out of plane direction are shown on the W/B₄C ML sample.

The Bragg peak position for each χ rotation is measured through Gaussian curve fitting analysis. Thereafter, the slope has been calculated from the linearly fitted 2θ - $\sin^2\chi$ plot. Finally, the residual stress in W layers can be determined from the equation as [101, 102]

$$\sigma_{ind} = -\frac{E_W}{2(1+\nu_W)} \frac{\pi}{180} \cot\theta_0 \frac{\partial(2\theta)}{\partial(\sin^2\chi)} \quad (2.33)$$

Where, E_W is Young's modulus and ν_W is Poisson's ratio (the ratio of the longitudinal strain to the lateral strain) of the tungsten layers. θ_0 is the stress-free diffraction peak associated with a particular diffraction plane. The slope $\frac{\partial(2\theta)}{\partial(\sin^2\chi)}$ indicates the variation of the diffraction peak position with $\sin^2\chi$. To determine the residual stress in W layers, the GIXRD performance was carried out by Huber 5020 diffractometer at energy ~ 15 keV with changing χ angles at Indus-2 synchrotron source (XRD beamline, BL-12) [103]. The film tilt angle χ

varies from 0° to 40°. The residual stress then calculated from diffraction peak (2θ) shift considering the respective diffraction plane of W.

Now, all the characterization techniques used for studying structural properties, spatio-chemical depth profile, and structure-optical properties correlation of thin films and multilayers (MLs) have been summarized in a table.

Table 2.1 Characterization techniques with brief description of measurements.

Serial No.	Characterization Techniques	Measurements
1.	X-ray Reflectivity (XRR)	It is a non-destructive technique used to measure layer thicknesses, surface interface roughness, and density of the layer in thin film and multilayer structure.
2.	X-ray Diffuse scattering	It differentiates the physical roughness and interfacial diffuseness. It also measures the correlation lengths (In-plane and perpendicular) at the interface, thus provides information about interface correlation.
3.	Resonant soft x-ray reflectivity (R-SoXR)	While grazing incidence energy dependent reflection spectra discriminate the element-specific chemical state of the overlying from that of underlying surfaces by tuning the incident angles, the angular resonant reflectivity curves precisely quantify its depth

		<p>profile in a nano structured configuration. Therefore, it probes for quantitative depth profile of spatio-chemical structure from surface to buried interfaces.</p>
4.	Near edge x-ray absorption spectroscopy (NEXAFS)	The different chemical states in the layer structure have been identified by the near edge x-ray absorption spectroscopy (NEXAFS).
5.	Transmission electron microscopy (TEM)	It is used to visualise and analyse the layer by layer structure in W/B ₄ C ML mirror.
6.	Substrate curvature method	The substrate curvature method is used to determine the total stress in the W/B ₄ C MLs coated on the Si substrate by measuring the radii of curvature before and after ML deposition.
7.	GIXRD based $\sin^2\chi$ method	It measures the residual stress only in W layers due to the elastic deformation of the material by measuring the diffraction peak shift.

Chapter-3

A novel approach for surface interface science of nano-scaled layered structure materials:

This chapter presents the development of a novel approach and its application that precisely probes spatio-chemical structural phenomena in layered nano-structured films. This approach is developed by the combination of resonant soft x-ray reflection spectroscopy at grazing incidence close to the “critical angle” with angle dependent reflection at energies near to the corresponding absorption edges. The developed technique precisely demonstrates the nano-scaled layered structure of C (20Å)/B (40Å)/Si (300Å)/W (10Å)/ Si substrate. This technique precisely quantifies the atomic migration across the interfaces, a tiny amount of chemical changes of materials and the presence of impurities from the free to buried interfaces. The technique enables to reconstruct chemically- and spatially-resolved nano-scaled interfacial map from free surface to embedded buried interfaces. The technique is sensitive towards resolving compositional differences within a few atomic percent in a non-destructive manner.

3.1 Introduction:

Nano-scaled layered structures with changing compositions have unique optical, structural, electronic, magnetic and superconducting properties with a wide range of applications in material science [1, 3, 5, 6]. Properties of these structures are strongly governed by the distribution & chemical nature of the elements and presence of impurity across the buried interfaces [104, 105]. The quality of the films is an important aspect that determines the critical parameters of these nano-scaled devices [106, 107]. Any differences of the physical, chemical and geometrical parameters from desirable ones cause fluctuations in their properties. For example, the catastrophic drop of the reflectivity is observed in ultra-short period x-ray multilayer or the quantum effects in nano-electronic devices are completely disappeared etc. The problem becomes more complicated when the interlayer is formed due to the atomic migration, chemical reaction etc. Therefore, the effect of the fluctuation of the properties of the devices may destruct the utility by influencing the effective work function of electrodes [108], the optical contrast [10] or magnetization [11]. Thus, the development of such complex nano-scaled layered structures requires the advancement of the analytical techniques and methodology to understand the spatio-chemical structure-property relationships in a nano-scale device [109, 110]. The x-ray reflectivity, a non-destructive depth resolving technique can be able to measure the spectroscopic information accessible by x-ray absorption at the corresponding absorption edges of the constituent elements. Thus, the resonant x-ray reflectivity is a unique powerful technique for quantitative depth profiling of the spatio-chemical information from the free surface to the buried interfaces present within the penetration depth of x-ray due to both layer- and element-specificity.

There are different types of analytical techniques (destructive and non-destructive) to quantify the depth profiling of the spatio-chemical information with their limitations. For

example, the spatio-chemical information with the desired resolution is obtained by transmission electron microscopy (TEM) imaging if the interface roughness is small. Conversely the quantification of atomic composition by this technique is problematic. Also, it is a destructive technique and difficult to detect the low-Z materials in the presence of high-Z materials [111]. Similarly, the photoelectron spectroscopy or analyses of fluorescent radiation in combination with argon ion-sputtering technique are also destructive methods for depth profiling. But the methods introduce the artefacts during sample preparation [112]. Therefore, it is required to develop alternative analytical techniques (less aggressive than TEM) that could be able to quantify spatio-chemical atomic profile across the hetero-structure with a depth resolution better than 10 Å. There are number of non-destructive techniques that can be used to probe spatio-chemical layer structure. Among these techniques, due to the lack of sensitivity of the structure with a low contrast interface, and/or low-Z materials, the combination of x-ray standing wave with x-ray reflectivity technique [112] is not able to precisely probe. Also, neutron reflectivity technique (NR) is complementary to x-ray reflectivity [113, 114], but there are some known limitations of NR [115]. Ultimately, both hard x-ray photoelectron spectroscopy (HAXPES) [116] and depth-resolved soft x-ray emission spectroscopies [117] are the appropriate non-destructive spectroscopic techniques. However, all of these techniques use different physical models when processing original data, which often introduces its limitations. Therefore, there is a need for a suitable non-destructive technique which provides the quantitative depth profiling of the spatio-chemical information from the free surface to the buried interfaces.

In the present work, a novel approach, the combination of resonant soft x-ray reflection spectroscopy with angular dependent reflection at energies around the respective absorption edges is used to probe the interfacial structural phenomena in nano-scaled layered

structural film. Due to its optimal chemical sensitivity, high contrast variability and high resolution, this technique can defeat aforementioned the limitations mentioned previously.

Recently, spectral dependent reflection spectroscopy is used in different contexts at relatively larger incidence angles to find the atomic and electronic structures of materials [57, 61, 63, 118-120]. Similarly, the reflection spectroscopy at constant momentum transfer q_z is used to detect the spatio-chemical layer structure in epitaxially grown transition-metal oxides [6, 121-123]. Zwiebler *et al.* [123] precisely demonstrated the sensitivity of constant q_z -reflectivity to a marker layer ($\text{La}_x\text{Sr}_{1-x}\text{TiO}_3$, $x=0.006$) in SrTiO_3 film. The layered structure was subsequently probed by fitting the measured reflectivity spectra using the pre-information of the film. Also, the soft x-ray reflectivity spectra were fitted for an epitaxial LaSrMnO_4 film to obtain the atomic structure of the layer and the stacking sequence of the atomic planes [123]. Nevertheless, the concept of limited probing depth of reflected beam within a nano-scale range close to the “critical angle” is not evidently understood. Therefore, one can try to investigate the spatio-chemical characteristics of the nano-scaled layer structure by altering the incidence angle. In addition, shallow incidence angles close to the critical angle deliver greater sensitivity. This discriminates the chemical state in a nano-scaled layer structure. Depending on the aforementioned technique, the combination of highly sensitive energy-dependent and the angle-dependent near-edge reflection spectroscopy is proposed to achieve a quantitative spatio-chemical structural profile of the complex nano-scale film.

At the absorption edges, the x-ray reflectivity profile shows the strong resonant behaviour due to variation of the atomic scattering factor. What happens if an incident photon interacts with the electrons in an atom? If the incident photon energy is less than the binding energy of the electrons, the polarization attributed to these electrons is in phase. When the incident photon energy is greater than the binding energy of the electrons the polarization

attributed to these electrons is out of phase. So, there is a phase reversal. This leads to the sign reversal of the real part of the atomic scattering factor. Depending upon the amount of out-of-phase component of polarization with respect to the in-phase, the amount of sign reversal occurs. Thus, the photon generates real and virtual transitions in which it is absorbed and reemitted. So the strong resonance occurs at the edge where the number of the bound electron is comparable more than the free electron. Let us take an example considering Si atom. In Si, the number of electrons in K, L and M shell are 2, 8 and 4, respectively. If we consider the resonant measurement in K shell, near the K-edge, the number of free electrons 12 (L and M shell electrons contribute out of phase). Number of bound electrons is 2 (K shell electron). The number of bound electrons is very less compared to the free electrons. Resonant effect is very less. If the resonant measurement is carried out in L shell, near L-edge, the number of free electron is 4 (M shell, these contribute in out of phase). The number of bound electrons is 8 (L shell electrons, these contribute in phase). The variation of the number of electrons near the Si L-edge is shown schematically in the figure. Therefore, near the absorption edge, the interaction of incident x-ray photon with electron undergoes a strong variation. This strong variation gives rise to a strong variation in atomic scattering factors (f_1 and f_2). This strong variation of atomic scattering factors modulates the reflectivity profile near the edge. Thus, the modulated reflectivity profile holds information about the spatial variation of the resonance elements.

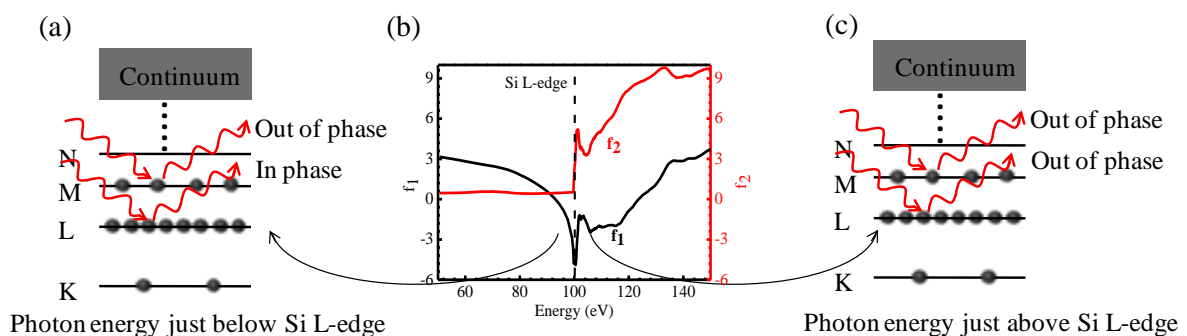


Figure 3.1 (a) Schematic energy level diagram of the Si atom with incident photon energy just below the Si L-edge. (b) The variation of the scattering factors (f_1 and f_2) around the Si L-edge. (c) Schematic energy level diagram of the Si atom with incident photon energy just above the Si L-edge.

The theoretical understanding of resonant soft x-ray reflectivity (R-SoXR) is similar to deuteration in neutron reflectivity which enhanced scattering contrast [124]. The angle dependent R-SoXR, a non-destructive depth probing technique, offers to precisely determine (a) structural, electronic and orientational ordering of organic films [58, 125, 126], (b) ordering in correlated electron systems [66], (c) electronic structure and structure of surface layers and thin films [61, 63, 127-129] and (d) magnetization in magnetic structures [64, 130, 131]. However, it is difficult to extract unique real-space information in order to achieve an element specific depth distribution profile in a straightforward way in more complex interface structure. The very poor electron density contrast at the interface with unknown interfacial atomic migration at different extents, chemical changes and the presence of impurities leads to complex interfacial structures. Therefore, it is required for proper understanding of the real and imaginary parts of scattering length density for modelling. In fact, here it is demonstrated an approach to defeat this difficulty with connecting spectral dependent reflection spectra to precisely and unambiguously determine the interfacial depth profile. In the present chapter, the developed technique enables precisely to reconstruct spatio-chemical interfacial map in a non-destructive manner up to tens of nanometre thickness within a few atomic percent. In the current thesis, the methodology has been demonstrated in the Si-B nano-scaled layered structure due to its technical interest because boron is used as a p-type dopant on a Si-based microelectronics device [132]. However, the methodology in general, will be applicable to other complex layered structures also.

3.2 Experimental details:

The thin film samples C (20 Å)/B (40Å)/Si (300Å)/W (10Å) are deposited on oxidized Si-substrate by using electron beam evaporation system (e-beam system) [74]. Si-substrates are cleaned by ultrasonic cleaning using acetone before deposition. The ultimate base pressure was $\sim 3 \times 10^{-8}$ mbar in the main chamber. A 10 Å thin W layer is deposited on the Si-substrate to offer the optical contrast between the Si-substrate and the deposited Si layer of thickness ~ 300 Å on the top of W layer. A boron layer of ~ 40 Å is deposited on Si layer and a C capping layer of thickness ~ 20 Å is deposited at the top of the sample to prevent the formation of native oxide. The deposition rate is maintained at ~ 12 Å/min and the layer thickness is monitored by a quartz crystal using Inficon IC-5 controller. The structural parameters were carried out through hard x-ray reflectivity (HXR) performance by Bruker D8 Discover diffractometer (at energy 8.047 keV). The R-SoXR performances are carried out at BESSY-II synchrotron source in the s-polarization geometry using the Optics Beamline [67]. The energy resolution of the beamline is $E/\Delta E \cong 2000$ near B K edge. The measurements are carried out using larger photon flux ($\sim 1.4 \times 10^{10}$) with smaller vertical angular divergence (0.5 mrad). The GaAsP-photodiode detector is used to collect the data. The data are collected up to $\theta = 89.2^\circ$ for angular soft x-ray measurements. The near edge x-ray absorption fine structure (NEXAFS) measurements are performed at an incidence angle of 45° in total electron yield mode. The soft x-ray absorption measurements (near edge x-ray absorption spectroscopy (NEXAFS)) were performed near the B, C and O K-edges and Si L-edge in the total electron yield (TEY) mode at Optics Beamline [67] of the BESSY-II storage ring. The measured data are accurately normalized to the beam flux. The schematic representation of the angular R-SoXR measurement and the energy dependent reflection measurement along with NEXAFS measurement are shown in the figure 3.1 (a and b). The more details of the NEXAFS measurements are already discussed in the section 2.5.6 in chapter-2. Here, the

measurements are done in small energy interval at the respective absorption edge. For example, the energy range is ~ 175 to 210 eV near B K-edge. Within this small energy interval, the penetration depth slightly varies for the material which has no absorption edge within this range. For example, for carbon at 2 degrees, penetration depth is 41.39 \AA at 175 eV and $\sim 43.69 \text{ \AA}$ at 210 eV. However, the penetration depth undergoes significant variations within this small energy interval for the material if it falls within the absorption edge. The penetration length varies significantly around the absorption edge of the respective material. When the incident photon energy just below the absorption edge, the penetration depth goes to maximum limit. Just above the absorption edge, the incident photon is involved to eject the electrons from the electronic shell. So, the penetration depth again decreases. For example, for B near B K-edge, the penetration depth at 2 degrees is 407 \AA at energy 188 eV (just below the edge) and 55.3 \AA at 191 eV (just above the edge). Although the penetration depth is energy dependent, near the absorption edge it is limited by a particular length for a particular layer at fixed incident angle. Therefore, to extract the chemical information the energy dependent resonant reflectivity measurement is carried out at different incident angle for different depth.

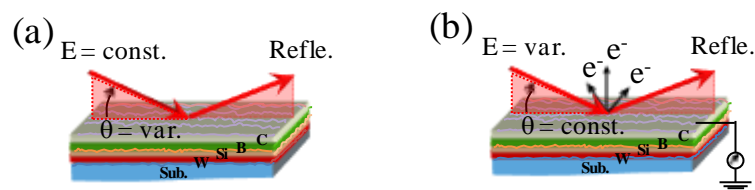


Figure 3.2 The schematic of the angular R-SoXR measurement and energy dependent reflection measurement along with NEXAFS measurement in the thin film layer structure is shown in this figure. (a) angular R-SoXR measurement, (b) energy dependent reflection measurement along with NEXAFS measurement.

The Parratt formalism [33] is used to model the R-SoXR measured data. The precisely measured optical constants δ and β (refractive index $n = 1 - \delta + i\beta$) of materials near the absorption edge are required for analysis of the R-SoXR data. The optical constants are obtained near the K- edge of boron for elementary B, B₄C and B₂O₃ using the measured absorption data [133] and using Kramers-Kronig relation [117]. It is noted that there is uncertainty in the tabulated values of near edge optical constants in Henke tabulated optical data [28] due to atomic like assumption and not considered in the present study. The measured microstructural parameters (such as the thickness of W and total film; rms roughness of the substrate, top surface and W layer; and density single layer (Si+B+C) and W layer) from HXR measurement data are used as starting guess for the modelling of R-SoXR measured data. Initially, the thicknesses of C, B, Si layers are used according to the deposited value. The optical constants of non-resonating elements (like C, Si, SiO₂ and W) close to B K-edge are accepted from Henke *et al.* [28]. The mass densities of C, B, B₂O₃, Si, SiO₂ and W are taken as 2.2, 2.34, 2.46, 2.33, 2.2 and 19.3 gm/cm³, respectively for optical constant calculations. The measured R-SoXR data is fitted through different iterations by simultaneously fitting the measured data at different energies of the respective absorption edges. This approach allows more reliable quantitative spatio-chemical depth profile from free surface to buried interfaces.

3.3 Results:

3.3.1 X-ray reflection spectra simulated near boron (B) K-edge:

The theoretical simulations of the spectral dependent reflectivity near the Boron K-edge are made for thin film with layer structure C (varying thickness)/B (40Å)/Si (300Å)/W (10Å)/oxidised Si substrate as shown in fig. 3.2 (a-c). The order of the layers structure remains the same as that of the fabricated one. The optical constants of B used for this calculation are measured as shown in fig. 3.2 (d). The other absorption edges like C K-edge,

Si L-edge and W N-edge in the layer structure are far from B K-edge. All the calculated fine structures in fig. 3.2 (a-c) are observed due to the B structure only. The fig. 3.2 (a) shows the structural sensitivity of the B layer with varying the thickness of the top C layer from 20 Å to 300 Å at the fixed incidence angle $\theta = 2^\circ$. The critical angle θ_c for total external reflection of C layer near B K-edge (190 eV) is 7.35° . It is observed that the incident field is penetrated ~ few tens of angstrom due to the finite absorption of the material below critical angle θ_c .

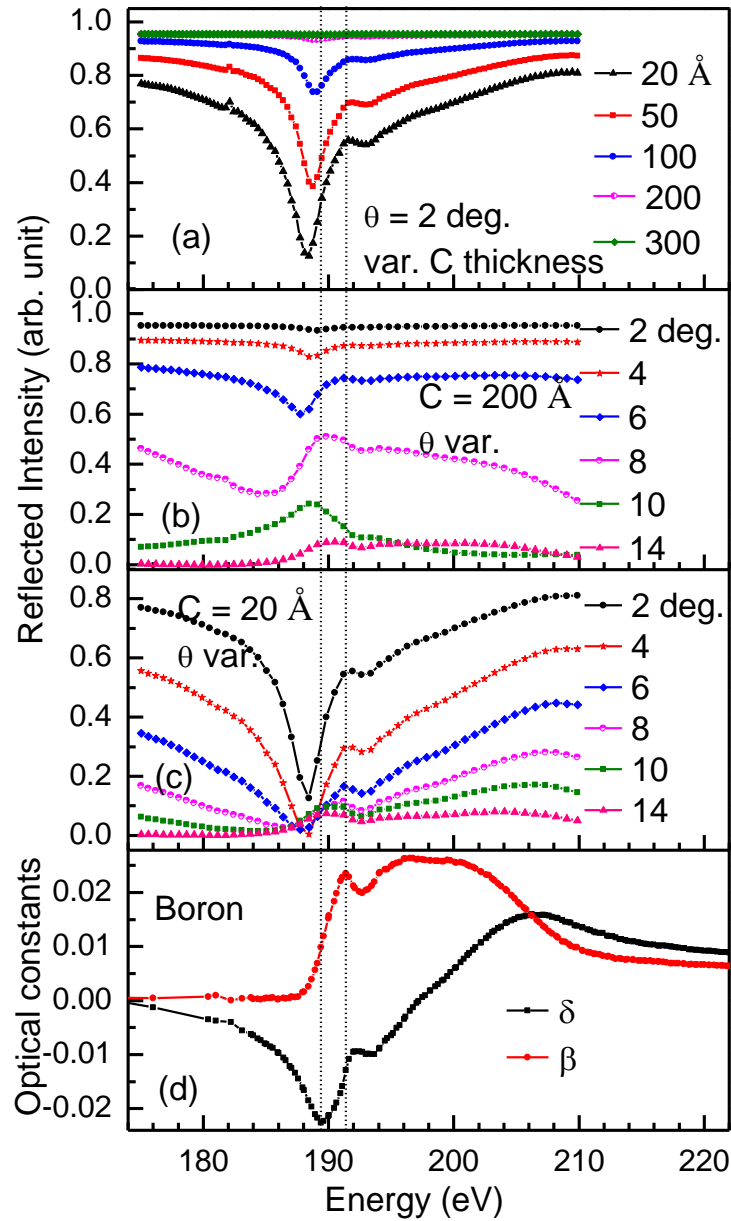


Figure 3.3 Energy dependent grazing incidence reflection spectra calculated near B K-edge for an ideal structure (considering bulk density and zero roughness) along with measured optical constants of elementary boron. (a) Reflection spectra at a grazing incidence angle of 2° by varying the thickness of the top C layer. (b) and (c) show the variation of the reflection spectra as a function of grazing incidence angle for the two different thicknesses of 200 \AA and 20 \AA of the top C layer, respectively. (d) Measured near edge spectral dependent optical

constants (δ and β) of boron. The vertical dotted lines correspond to the positions of the dip ($E \sim 189.4$ eV) and peak ($E \sim 191.3$ eV) in the δ and β profiles, respectively.

The penetration depth of the electric field is also tuned by changing the incident angle near the θ_c . For example, the penetration depths of the electric field in the C layer at energy 190 eV are 42 Å, 48 Å, 70 Å, 125 Å, 455 Å and 1768 Å for different incident angles 2°, 4°, 6°, 7°, 8° and 15° respectively [28]. When the top C layer thickness is more (≥ 200 Å), the underlying boron signal is not noticeable and hence reflectivity profile is nearly a flat manner. As the carbon thickness decreases (≤ 100 Å), the boron signal (amplitude of oscillation at resonance) gets enhanced gradually with more pronounced at the dip. Based on the spectral dependent near the edge reflection, this ensures the possibility of non-destructive depth-profiling of the local atomic structure. However, it must be emphasized that by the interference of waves reflected at the surface and interface between the C and the B layers the features in the reflection spectrum can be shifted in the energy scale and their amplitudes can be changed as shown in fig. 3.2 (a and b). In fig.3.2 (c) it is clearly observed that C layer (thickness 20 Å) does not affect the feature of the B layer. At a larger angle ($> \theta_c$) absorption effect is more prominent increases with increasing θ . The reflection spectrum in this region of the angles is very similar to the absorption spectrum [134]. The dielectric constant $\epsilon(E)$ and the refractive index $n = 1 - \delta + i\beta = \sqrt{\epsilon(E)}$ are complex functions due to the strong absorption of soft x-rays in the material. In this connection, the condition of the total external reflection does not hold even at the extreme lower value of grazing incidence angles for boron near its K-edge having a sign reversal of δ . Because of this sign-reversal, the reflected intensity is visible and slowly decreases (in the ample angular region) that makes possible the non-destructive local atomic structure depth probing of the samples. These observations clearly demonstrate how to discriminate the chemical information of the overlaying surfaces from that of underlying in nano-scaled range.

3.3.2 Experimental results of near-edge reflection spectra:

To obtain the chemical information at the different depths of the layer structure of C (20 Å)/B (40Å)/Si (300Å)/W (10Å)/oxidised Si substrate, the energy dependent reflectivity measurements at different grazing incidence angles are performed at the respective absorption edges of the elements. Also, the reflection spectra are examined simultaneously by near edge x-ray absorption fine structure (NEXAFS) spectroscopy (black line) at an incidence angle of 45° using TEY mode to sustain the validity of our approach.

It is observed that the absorption spectra of the C, B, and O K- edges and the Si L- edge are notably different from each other. It is familiar [135] that when a carbon film is grown on the top of the substrate the crystal structure of the film is modified which depends strongly on the method, precursors, atoms, or clusters, during synthesis process. In Figure 3.3 (a) the reflection and absorption spectra at C K-edge reveals that carbon layer is characterized with a high content of sp^3 hybridized carbon and sp^2 hybridized carbon [136]. The 1st dotted line at energy ~ 283.6 eV indicates the transition due to C $1s \rightarrow \pi^*$ absorption. The second dotted line at ~ 284.7 eV (1st peak) indicates the transition C $1s \rightarrow \pi^*$ in the C=C double bond in sp^2 -coordination [135, 137]. The additional 2nd peak at energy ~ 286.1 eV (3rd dotted line) is associated to C $1s \rightarrow \pi^*$ transitions due to the presence of oxygen contamination at the sample surface. The transition (indicated by 4th dotted line) observed at ~ 287.9 eV is assigned to the C $1s \rightarrow \sigma^*(\text{C-H})$ transitions [138]. This resonance is responsible for the sp^3 coordination. The 5th dotted line i.e. the onset of the smooth edge at ≈ 291 eV takes place from $1s \rightarrow \sigma^*(\text{C-C})$ states transition. All of these features correlate well with the NEXAFS spectrum (black line), indicating different chemical environments of carbon.

Analysis of the reflection and absorption spectra near the B K- absorption edge (Fig. 3.3 (b)) was conducted at different grazing incidence angles. The near-edge features of B are

not evidently seen because of the top carbon layer at small angles ($\theta = 2^\circ$). When the incident angle increases, the deeper layers are implicated into the reflection process. As a result, the local structural information from B layer becomes more visible. Moreover, the beam penetrates through boron layers to the underlying silicon layers at some grazing incident angles. There is a clear angular dependence of the resonance reflection intensities, which can be used to get information about the distribution of resonating elements at different depth scale in layered structure. The shape of the B K-edge reflection spectrum is well correlated with the absorption spectrum. The reflected intensity goes minimum (first dotted line) at the absorption edge (~ 189.4 eV). The peak (2nd dotted line) comes due to the electronic transition of B 1s to unoccupied 2p_z (π^*) states at energy ~ 191.3 eV. A broad peak is clearly visible in absorption spectrum which is due to the transition of B 1s electrons to unoccupied σ^* -states [133] in the energy range ≈ 193 eV to 207 eV centred at ~ 199.8 eV (4th dotted line). A tiny feature arises at energy ~ 193.8 eV (3rd dotted line) due to the overlap of small features of the π -resonance of both the elementary B and B₄C (Fig. 3.2 (d) and ref. 122) in both reflection and absorption spectra. At that same energy (~ 193.8 eV) the strong π -resonance of B₂O₃ is also located [133] but the angle dependent reflectivity performance indicates the absence of the B₂O₃ (discussed later).

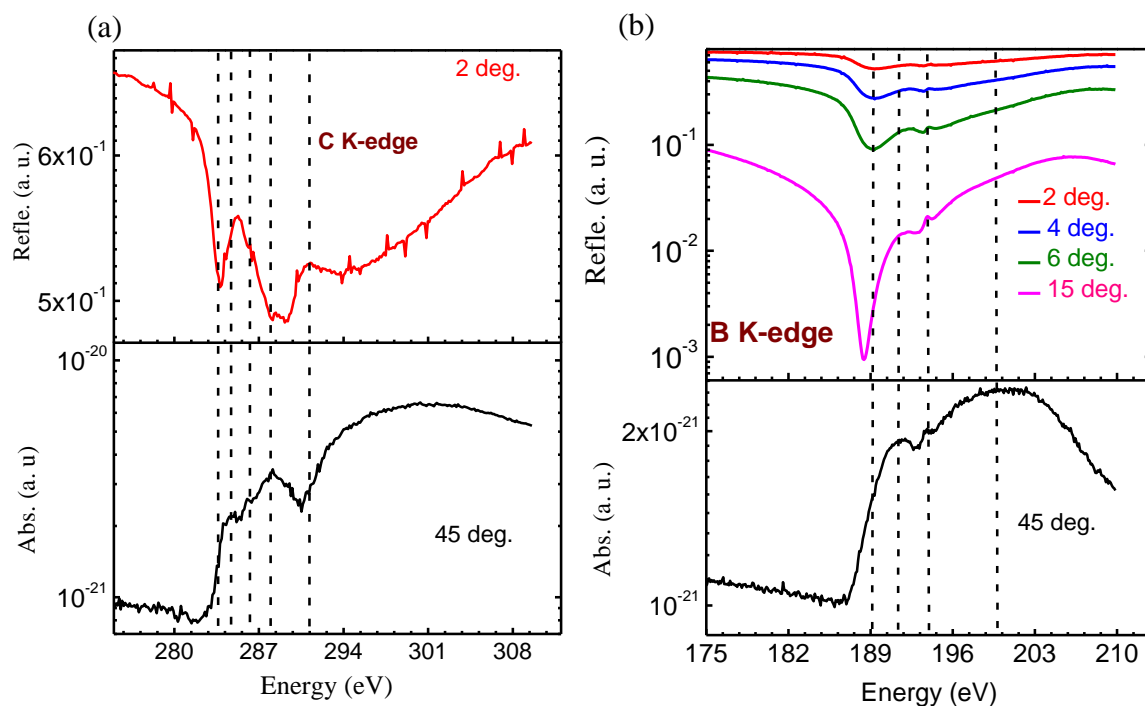


Figure 3.4 The measured reflection spectra (energy dependence) (coloured line) at different selected incidence angles around the K-edges of C, B. Also, the measured NEXAFS spectrum (black line) at 45° close to the respective edges is shown. (a) C K-edge region. (b) B K-edge region. The vertical dotted lines represent the fine structure features at different energy positions as mentioned in the text.

Now come to discuss the near edge reflection spectra along with absorption spectra at O K-edge. The O K-edge is traced in the measured reflection spectra for different specified grazing incidence angles (2°–6°) as well as in absorption spectra shown in figure 3.4 (a). The presence of oxygen is probably due to the adhesion of hydrocarbons (observed near C K-edge also) and water molecules at the top surface when the sample is exposed to ambient condition before the measurements. The analysis of the reflection spectra at O K-edge is well correlated with the absorption spectrum at the C K-edge and silicon oxide inside the layer structure if the top layer is assumed to get oxidized. The feature (1st dotted line) at energy 531 eV originates from C=O (π^*) bonds [139]. The strong band (3rd dotted line) at energy at ~ 539

eV arises from C=O (σ^* resonance) and/or from adsorption of water [139, 140] and from O 1s electrons to 2p states transitions mixed with Si 3s, 3p states in SiO₂. A careful analysis of the reflection spectra measured at different grazing angles reveals the appearance of an additional feature near 535 eV at the $\theta=4^\circ$. This feature can be traced in the absorption spectrum which makes evident itself in the asymmetry at the lower energy side. One can guess that an extra interface is incorporated in the formation of reflected beam with increasing θ because increasing the angle θ leads to the increase of the depth probing. It is indicated that the possibility of contribution from B=O bonds could be ruled out because the measured angular reflectivity near B₂O₃ edge reveals no presence of B₂O₃ (discussed in next section)

Near the Si L-edge (Fig. 3.4 (b)), the reflection spectrum exhibits a dip at energy \sim 98.8 eV (1st dotted line) because of the sign reversal of the real part of atomic scattering factor (hence δ) of Si even at extremely low glancing incidence angle of 2° . It is important to mention that near the Si L-edge (say at 99 eV), at incident angle $\theta = 2^\circ$, the radiation exhibits nearly a total reflection effect for carbon and boron layers with marginal penetration depth \sim 40 Å and \sim 43 Å, respectively. Therefore, it is almost impossible to identify the underlying silicon layer, which is present in the bottom of 60 Å. However, the observed signal at $\theta = 2^\circ$ confirm that silicon atoms may diffuse into the overlaying layers.

Nevertheless, in a real experiment due to a high sensitivity of the measurement, the attenuation length determines the real depth exceeding the depth at which the wave field is reduced in e-fold [134]. This means it may be possible to monitor the signal from a deeper level. In the absorption spectrum, the peak at \sim 99.6 eV (marked by second vertical dotted line) is assigned to Si L -absorption edge due to transition of 1s \rightarrow 2p electrons. Similarly, the peak at 106 eV in the absorption spectra arises due to silicon oxide (SiO₂) [141].

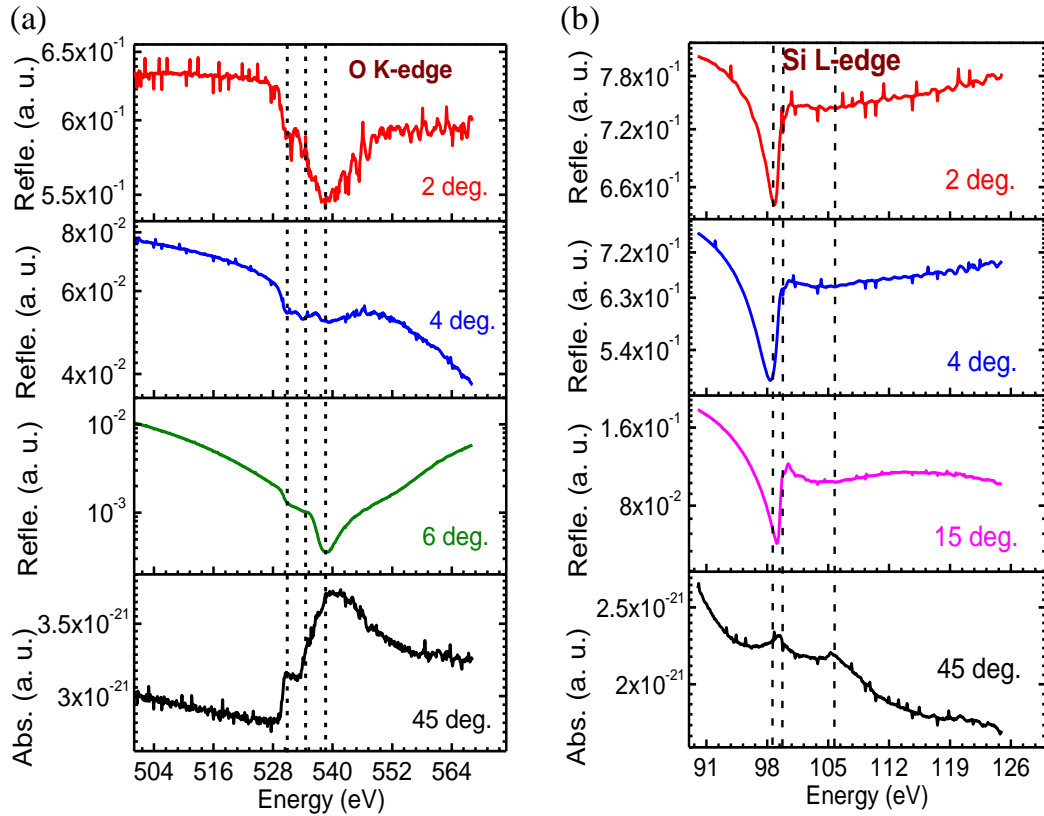


Figure 3.5 The measured reflection spectra (energy dependence) (coloured line) at different selected incidence angles around the O K-edge and Si L-edge. Also, the measured NEXAFS spectrum (black line) at 45° close to the respective edges is shown. (a) O K-edge region. (b) Si L-edge region. The vertical dotted lines represent the fine structure features at different energy positions as mentioned in the text.

The experimental reflection spectroscopy suggested the presence of different chemical information at the different depths of the structure and the results are well correlated with NEXAFS. Furthermore, the chemical information obtained using glancing incident reflection spectroscopy greatly complements with the angular dependences of R-SoXR for a more precisely determination of the quantitative depth profile of elemental distribution by utilizing the exact resonance intensities as discussed below. Hence, the present demonstration clearly reflects that the grazing angle reflection spectroscopy could be a potential tool to

obtain spectroscopic information at different depth scale in a layered structure thin film system. This clearly demonstrates novelty in the approach and importance in its utility in the emerging field of nano-scaled layered structured system.

3.3.3 Quantitative spectroscopic depth profile:

Before going to detailed quantitative spatio-chemical depth profiling of C (20 Å)/B (40Å)/Si (300Å)/W (10Å)/oxidised Si substrate layered structure using R-SoXR, the microstructural analysis of the layer structure was determined by hard x-ray reflectivity (HXR) measurements at energy of 8.047 keV as shown figure 3.5. The best-fit results are shown in the Table-3.1. The hard x-ray reflectivity (HXR) profile is fitted by considering Si, B and C layers as a single layer. The electron density profiles (EDP) are same for these three layers. The EDP profile shows no variations (see the inset of the figure 3.5) of these three layers which indicate that HXR is insensitive to the B/C and Si/B and interfaces due to the low electron density contrast (ideal $\Delta\rho_{B/C} \approx 1.7\%$ and $\Delta\rho_{Si/B} \approx 8.6\%$).

Table 3.1 The best-fit results of HXR the thickness, rms roughness and mass density.

Layer	Thickness (Å)	Roughness (Å)	Mass density ($\pm 3\%$)
Si+B+C	352 ± 1	8.3 ± 0.5	97 % of Bulk value of Si
W	11 ± 0.5	4 ± 0.5	96 % of Bulk

The best fitted result shows the rms roughness of the Si substrate is $\sim 4.5 \pm 0.5$ Å. A native oxide (SiO₂) layer (thickness of ~ 15 Å and rms roughness of $\sim 3.5 \pm 0.5$ Å) at the top of the Si substrate is taken to obtain the best-fit result.

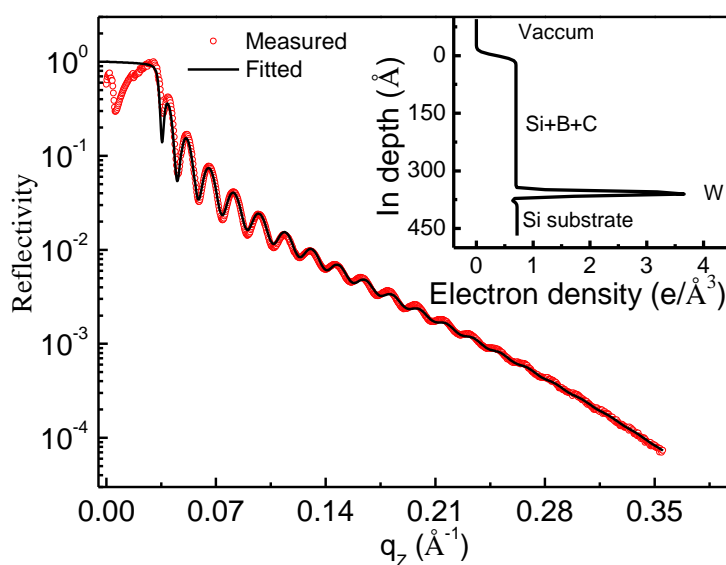


Figure 3.6 Measured Hard X-ray reflectivity (using Cu K_α source, $E=8.047$ keV) with fitted curves of the layer structure and electron density profile (inset) are shown in the figure.

In addition to the lack of ability to investigate the C/B and B/Si interfaces due to too low contrast, hard x-ray reflectivity is also unable to carry information about interfacial atomic diffusion, chemical changes and / or contamination of layers because of the presence of impurities.

To quantify the spatio-chemical depth profile from free to buried interfaces in layer structure, the angle dependent R-SoXR measurement was carried out near respective absorption edges of the elements. The R-SoXR spectra were measured around the K-edge of elementary boron (Fig. 3.6 (a)) at the selected energies in a narrow energy range (187 eV to 191.4 eV). These spectra quantitatively express the element specific information and the spatial variation of resonating boron atoms in the layered structure. This is because at this narrow energy range the atomic scattering factor of the elementary boron undergoes through a strong variation (shadow region in Fig. 3.6 (b)), whereas the flat optical response is observed for all other elements (for e.g., Si, C and W). Again, it is noteworthy to mention that

the oscillation pattern of R-SoXR curves get strongly modulated due to the interference of reflected amplitudes from the surface and different interfaces constituting the system.

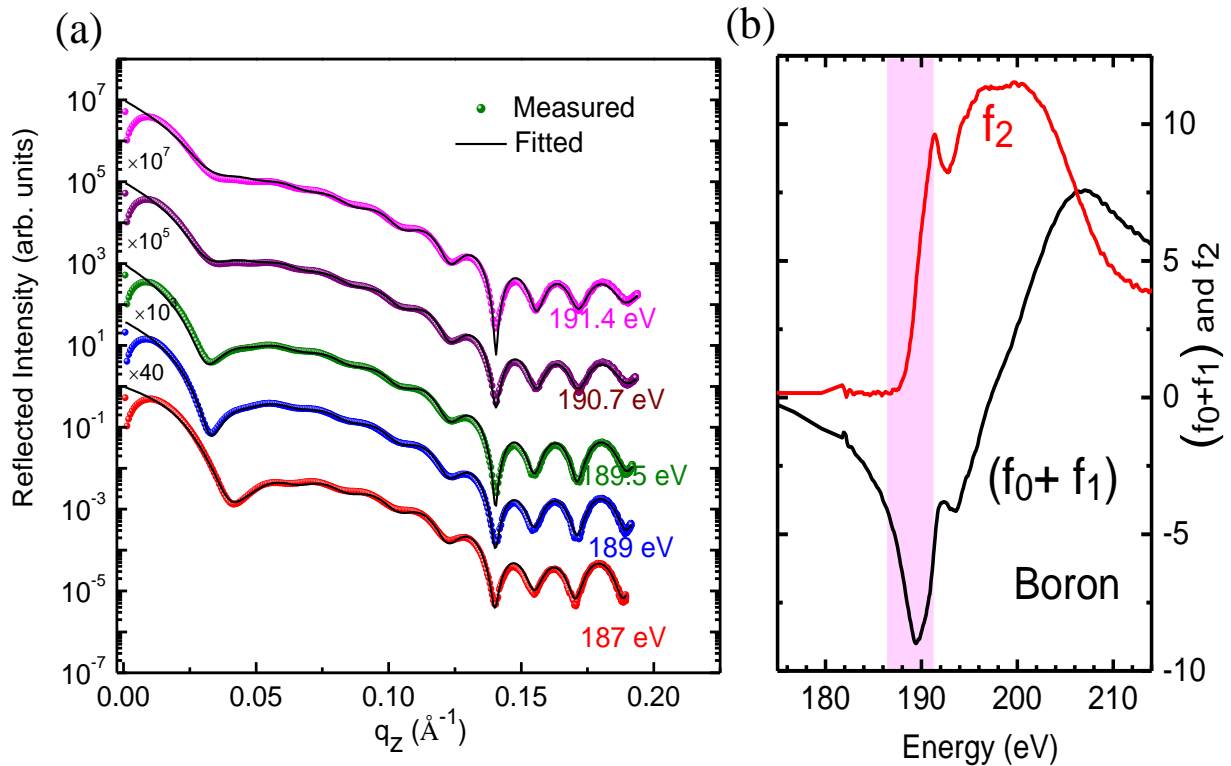


Figure 3.7 (a) Measured and fitted angular R-SoXR measurements around the B K-edge at the selected energies. The spectra are shifted vertically for clarity. This figure analyzes the quantitative structural and compositional analysis using angle dependent R-SoXR near to the B K-edge. (b) Spectra of the atomic scattering factors of B around the K-absorption edge. The coloured shadow area exhibits the energy range over which R-SoXR performance was carried out.

Therefore, the discrepancy between the HXR and the R-SoXR clearly verifies that R-SoXR is sensitive to low contrast C/B interface and B/Si interface. Moreover, to obtain the information about the chemical state of B atoms in the layer structure, the R-SoXR performances are carried out around the B K-edge of B_2O_3 (at energy 194.1 eV). The R-SoXR at the B K-edge of B_2O_3 exhibits similar behaviour with each other although the

atomic scattering factor of B_2O_3 shows a strong variation [figure 3.7 (a)]. The strong variation (shadowed region) of atomic scattering factor near B K-edge of B_2O_3 is shown in the figure 3.7 (b). This indicates that the B_2O_3 is not present in the layer structure within the detection limit. The absence of B_2O_3 may be due to the presence of the carbon cap layer at the top which prevents oxidation of the boron layer when the sample was exposed to the ambient condition.

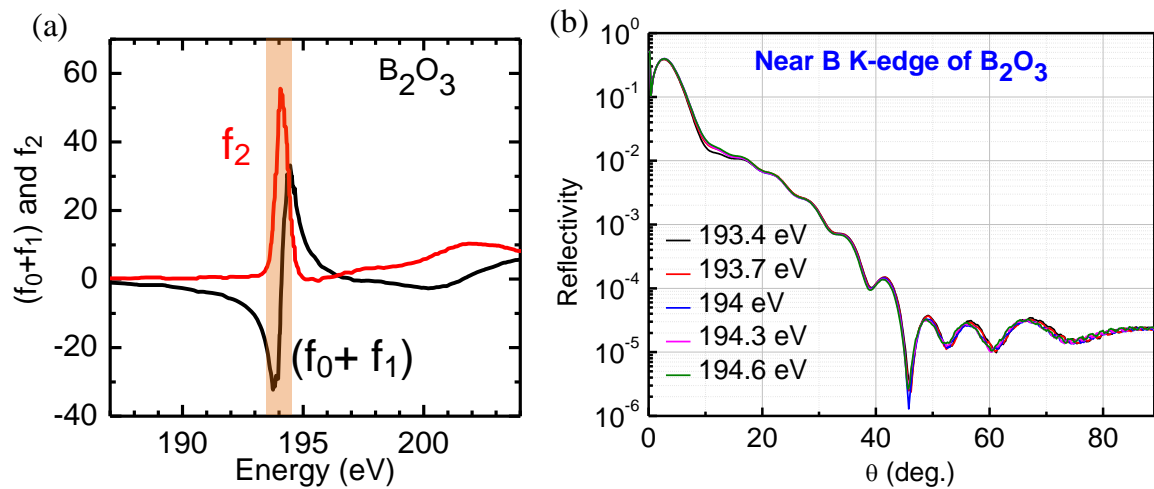


Figure 3.8 (a) Measured R-SoXR spectra at energies near the B K-edge of B_2O_3 . (b) This figure shows the variation of atomic scattering factor of B_2O_3 . The shadowed region indicates the energy range over which the measured R-SoXR profiles were presented.

The distribution and the chemical nature of the elements in a nano-scaled thin film are determined explicitly using an approach based on concurrent data fitting [128, 129] and is also briefly explained in the experimental details and data analysis section. In order to achieve consistent and reliable compositional parameters and the structural parameters, the measured R-SoXR profiles are fitted concurrently at the selected five different energies close to the B K-edge (Fig. 3.6 (a)).

The detailed fitting process how the fitting parameters affect the quality of the fitted parameters is shown in figure 3.8. In figure 3.8 the measured R-SoXR with fitted data at

190.7 eV clearly demonstrates the sensitivity of the R-SoXR technique for atomic composition of the resonating atoms in a layered structure. To realize this sensitivity, the composition of the boron layer has been altered by varying percentage of incorporation of silicon into the boron layer whereas all the structural parameters are kept fixed. The reflectivity profiles undergo strong modulation when the percentage of the boron is varied in the middle boron layer. The best fit result is obtained at 25 % of silicon in the middle boron layer. It is observed that the best-fit value deviates significantly even a change of 5 % resonating boron atoms away from that of the best-fit results. This implies that the R-SoXR is a highly sensitive technique for compositional analysis within a few atomic percent. For example, at 190 eV, 5% addition of boron atoms into the carbon layer changes the value of δ (β) from 8.13×10^{-3} to 6.79×10^{-3} (from 6.57×10^{-4} to 1.64×10^{-3}), respectively. Therefore, the scattering contrast at the interface, $(\Delta\delta)^2 + (\Delta\beta)^2$, undergoes a momentous and tunable enhancement.

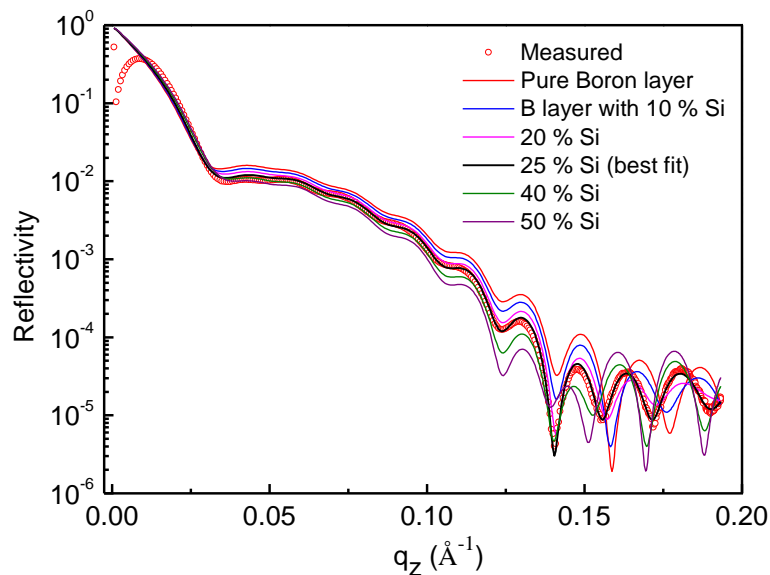


Figure 3.9 The measured and the fitted R-SoXR data at 190.7 eV demonstrating the sensitivity of R-SoXR to atomic composition of the resonating atoms in a layered structure.

In figure 3.9 (a), the best fit results show that the effective electron density profile (EDP). The profiles show that the strong sensitivity to the C/B and B/C interfaces. As the energy changes, the effective EDP profiles of the layers (B layer and the interlayer) containing the resonating B atoms undergo significant deviation.

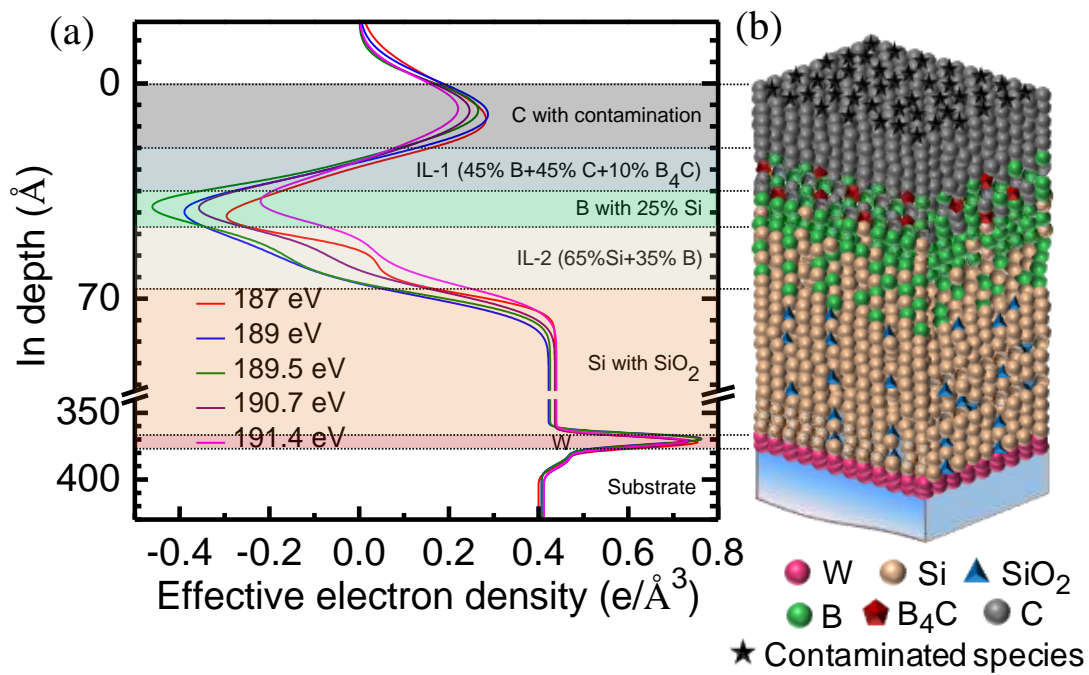


Figure 3.10 (a) The effective electron density (EDP) depth profiles obtained from the best-fit R-SoXR results. (b) Schematic representation of variation of spatial composition according to the best-fit R-SoXR data.

It is clearly observed that the boron atoms are embedded into the carbon and the silicon layers because the effective EDP profile is negative owing to sign-reversal of the real part of atomic scattering factor. The C/B and B/Si interfaces are not sharp and the mixed interlayers are formed at the C/B (IL-1) interface and B/Si (IL-2) interface. The best-fit results of the composition of layer structure, layer thickness, and rms roughness are given in Table no 3.2.

Table 3.2 The table contains the best-fit results of the composition of the layers structure, layer thickness, and rms roughness earned from R-SoXR measurement.

Layer structure	Layer composition ($\pm 3\%$)	Thickness (\AA)	Roughness (\AA)
C	C with contamination	21 ± 2	10 ± 1
IL-1	45% B + 45% C + 10%	15 ± 1	8 ± 2
B	75% B + 25% Si	9 ± 1	5 ± 1
IL-2	35 % B + 65% Si	22 ± 3	8 ± 2
Si	Si with SiO ₂	298 ± 3	4 ± 2
W	W	8 ± 1	2.7 ± 0.5

The thickness of the interlayer IL-2 is greater than that of the interlayer IL-1 due to the more atomic diffusion in the earlier interface. The low effective electron density $\sim 0.364 \text{ e/\AA}^3$ (bulk value = 0.429 e/\AA^3) is observed at the top carbon layer due to the contamination of hydrocarbon and other contaminants when the sample was exposed to surroundings. The boron does not present in the top carbon layer because the optical properties of the top C layer do not alter extensively around the B K-edge. The truncation in the effective EDP of the C layer (Fig. 3.9 (a)) is owing to the combined effect of the relatively smaller thickness of the C layer, the large negative effective EDP value of the underlying layer and the roughness. The signal of B₄C compound is observed due to the formation of a C-B bond in IL-1 at C/B interface. Furthermore, it is observed by best fit results that the boron layer is not pure and $25 \pm 3\%$ of Si atoms have diffused into the upper boron layer. Also, the interlayer IL-2 is composed of $35 \pm 3\%$ boron and $65 \pm 3\%$ Si. The considered layer structure is characterized by island film growth mode, which leads to the formation of the interface layer with stoichiometry B:Si \sim 1:2 where further silicon clusters or solid solution of Si and B are formed. Only after these steps, the boron layer begins to grow. The fitted result of the

effective EDP profile shows that the electron density of Si-layer is slightly greater than the pure Si shown in Fig. 3.9(a). This is owing to the presence of SiO₂ which has a high effective EDP. The presence of contaminant oxide in the Si-layer may arise during the deposition. The R-SoXR is not so sensitivity for oxide contamination of Si in other layers containing both boron and silicon around the B K-edge. Therefore, SiO₂ in the boron layer and the IL-2 are not shown in the Fig. 3.9 (b). The quantification of the SiO₂ contamination can be determined by analyzing the R-SoXR profile near the Si L-edge in the similar approach. A schematic of the atomic depth distribution is modelled by considering the best fit results of R-SoXR as shown in the Fig. 3.9 (b). Thus, R-SoXR is a highly sensitive technique to quantify the atomic migration across the interfaces, the tiny amount of chemical changes and the presence of impurities from the free surface to buried interfaces even if the very low density contrast.

3.4 Conclusion:

In conclusion, a non-destructive methodology is demonstrated experimentally to determine quantitatively spatio-chemical depth profile from free to buried interfaces by using resonance reflection spectra in soft x-ray regions. The grazing incidence reflection spectra extract the element specific chemical information from free to buried interfaces whereas the angle dependent resonant reflectivity profile precisely quantify the depth profile. The developed approach in the present study will stimulate to reconstruct the spatio-chemical interfacial maps for other low-Z systems by advancing the resonant soft x-ray reflection spectroscopy.

Chapter-4

Understanding the evolution of residual stress with varying microstructure in nano scaled W/B₄C MLs:

In this chapter, residual stress and its correlation with microstructure have been studied near the onset of formation of the continuous layer, important for ultra-short period W/B₄C ML optics, with varying individual layer thickness. The microstructural details are determined by using x-ray reflectivity (XRR) and x-ray diffuse scattering (rocking scan) performances. The total residual stress in W/B₄C ML stack which is obtained by the substrate curvature method is correlated with the residual stress of W layers obtained by grazing incidence x-ray diffraction (GIXRD) based $\sin^2\chi$ method using synchrotron. The total residual stress in ML film is correlated with the stress contributions from individual layers as well as interfacial stress. A non-monotonic variation of compressive residual stress is observed with varying the structural parameters and explained on the basis of the mechanism of growth of film at early the stage of film formation.

4.1 Introduction:

Nano-scaled thin films and multilayers (MLs) have been used in a wide range of applications in materials science [1, 142]. Recently, Periodic MLs find potential scientific interest due to the technological applications in various branches such as astrophysics [17], plasma diagnosis [15], soft gamma-ray optics [9] and synchrotron radiation instrumentation [12, 13]. The properties of these structures are strongly affected by the structural parameters such as layer thickness, composition, interfacial microstructure, and residual stress. Recently, due to advances in fabrication technology, there is a demand for ML structures of different layer thicknesses ranging from a few angstroms to few nanometers for various applications in frontier areas. However, in Volmer–Weber growth mode, most of the materials in this ultra-thin thickness range are grown as either near the limit of the continuous layer or in the discontinuous /quasi-discontinuous region. As a result, it is expected that the microstructure and morphology of the film are different from the continuous layers. Particularly, the optical properties are strongly influenced by the thickness of the layer, the composition of the layers and the imperfections at the interface [143-145]. Due to interdiffusion at the interface, the decrease of density contrast and the increase of interfacial width [146] reduce the specular optical performance. Another important governing factor is residual stress. This also acts an vital task in the optical performance of nano-scaled x-ray ML optics. Such as, cracks and buckling may be generated or ML film may peel off from the substrate due to high residual stress [24, 26]. In addition, it is expected that the interfacial atomic diffusion process in MLs with layer thickness near the quasi-discontinuous and/or discontinuous range may differ with that in the continuous thickness range. This could bring about unexpected changes in the physical properties of the materials and in the morphology of the interface which also affects the nature of the residual stresses of an ML structure. Therefore, it is necessary to understand the evolution of residual stress, stress-microstructure relationship with varying individual

layer thickness at ultra-short range. This can help to improve the long-term stability of the structures and their properties, for the better optical performance of ML mirrors by simultaneously reducing the residual stress and improving the quality of the interface.

Previously, the residual stress in ML optics has been studied by varying different process parameters [147-150]. It is noted that apart from the variation of stress with the process parameters, the residual stresses of the ML structures are also influenced by the thickness-dependent micro structures. In general, the total residual stress in an ML structures is contributed by stresses from individual layers as well as from interfacial stress. The nature of interfacial stress can be compressive or tensile that depends on the interface structure, material combinations, and individual layer thickness. For example, the stresses at the interface are tensile in sputtered deposited Cu/ Cr ML structures with periodicity 20 nm [71] and compressive in Ag/Ni ML structures with varying periods from 4 nm to 15 nm [64]. Zhang *et al.* [151] observed that the interfacial stress varies from 15 N/m to 90 N/m as the B₄C thickness changes from 30 nm to 90 nm in Cr/B₄C MLs. When the periodicity of the MLs decreases to lower value, the interfacial stress becomes more significant [71].

In recent times, many researchers have studied the evaluation of residual stress in MLs with varying individual layer thicknesses of the ultra-thin limit. The residual stresses in sputter-deposited W/Cu MLs have been analysed with altering the thickness of the W layer (12 nm to 1.5 nm), having fixed thickness of the Cu layer at 1 nm and 0.5 nm [152]. It is observed that that the total residual stress is compressive and lower (-3.2 GPa) compared to the compressive stress in the W layers (-6.8 GPa), for MLs with a periodicity $d = 2$ nm (thickness of W = 1.5 nm and thickness of Cu = 0.5 nm) and a number of layer pairs, $N = 90$. Similarly, based on the phase formation of W by altering the W layer thickness (7 nm to 2.5 nm) at a fixed Si layer thickness (3 nm), the nature of the stress W layers has been analysed in sputter-deposited W/Si MLs [153]. Windt observed that the β phase of W layer becomes

more tensile and the α phase becomes more compressive. Windt also studied the residual stress variation as a function of the individual layer thickness of ultra-thin limit, aging and thermal effect on stress in MLs (Mo/Si, W/Si, and Mo/C) [153]. It is seen that the stress depends on the thickness of the individual layers and also this can change over time. The evolution of the residual stress is explained by the various mechanisms. These are coherency stresses, interfacial stress, diffusion and energetic bombardment during film growth and stress associated with the formation of the amorphous interlayers. The W/B₄C ML is a promising candidate due to its good optical contrast at the interface, sharp and chemically stable interface [154]. A very little work has been studied on stress–structure correlation on periodic W/B₄C ML system. Previously, Windt [155] studied stress and roughness of single layers of W and B₄C as well as the W/B₄C ML (fixed period: $d = 1.125$ nm, $N = 40$; depth graded: the range of $d = 2.5$ nm to 45 nm with $N = 200$) with an intent to obtain a low stress and roughness by reactive sputtering in a nitrogen-argon gas mixture. It is observed that the stress as well as roughness decreases substantially owing to the incorporation of N₂ gas. However, the incorporation of the N₂ gas reduces the contrast at the interface. Further, incorporation of nitrogen can also increase absorption in the spectral region near the nitrogen. A detailed evaluation of residual stress and its correlation with microstructure without incorporation of nitrogen has not been addressed so far. These aspects were undertaken by systematically varying the microstructure of the individual layers at a constant number of layer pairs ($N=20$) near the layer continuous region, which has been discussed in this chapter. This is followed by a detailed stress-structure correlation analysis which are carried out in W/B₄C MLs with changing of N from 20 to 400 at a fixed periodicity of the order of ~ 1.9 nm, required for soft gamma-ray application [next chapter], which has been discussed in the next chapter.

In this chapter, the residual stress is analysed with altering the thickness of the individual layer ($\sim 0.4\text{--}3$ nm) in sputtered deposited W/B₄C ML with a constant N=20. It provides a better understanding of the evolution of residual stress- microstructure correlation.

4.2 Experimental details:

Two sets of periodic W/B₄C MLs have been fabricated on Si (100) substrates by a magnetron sputtering instrument [76]. In sample set-A, W layer thickness varied from 2.03 nm to 1.06 nm with unaltered B₄C layer at ~ 2.9 nm and the number of layer pairs N= 20. In sample set-B, B₄C layer thickness varies from 2.13 nm to 0.4 nm with fixed W layer thickness at ~ 1.7 nm and N=20. To obtain the structural parameters the hard x-ray reflectivity (HXR) and diffuse scattering (rocking scan) measurements are carried out at Cu K _{α} source. The substrate curvature method is used to determine the total residual stress in the W/B₄C MLs by a Zygo Mark-II laser Fizeau interferometer [92, 93] by determining the radii of curvature of the substrate before and after deposition of MLs. The schematic of the experimental arrangement for total residual stress measurement is shown in [figure 2.7, chapter 2]. Then the residual stress of W/B₄C ML systems was calculated using the Stoney equation [94, 95]. In this chapter, the values of Poisson's ratio and Young's modulus of the Si substrate are taken as 0.22 and 165 GPa, [96] respectively. The thickness of Si substrate is 0.5 mm. The details of the curvature method are described in the chapter-2 (section 2.5.8.1).

The residual stress in the W layers is determined by using grazing incidence x-ray diffraction (GIXRD) based $\sin^2\chi$ method in INDUS-2 BL-12 synchrotron source. The schematic of the GIXRD measurement are shown in the [figure 2.9, chapter 2].The GIXRD measurements are carried out using six-circle diffractometer (Huber 5020) with a scintillation point detector [103] at energy 15.4 keV and fixed grazing incidence angle (α) 0.6° with respect to the sample surface. The film tilt angle (χ) varies from 0° to 40°. The residual stress

of the W layers is determined from diffraction peak (2θ) shift of W (110) due to the change in lattice spacing at different orientations. The details of the curvature method are described in the chapter-2 (section 2.5.8.2).

4.3 Results and Discussion:

4.3.1 Microstructural analysis (hard x-ray reflectivity and diffuse scattering):

The structural parameters of the W/B₄C MLs are obtained by fitting of hard x-ray reflectivity (HXR) and diffuse scattering profile. The measured and fitted x-ray reflectivity profiles of W/B₄C MLs for two sample sets, Set-A (ML-a to ML-d) and Set-B (ML-e to ML-h) with varying individual layer thickness are shown in figure 4.1. The reflectivity profiles are plotted with varying the momentum transfer vector (q_z). The best fit results are given in the table 4.1. The HXR measurements are carried out up to a higher q_z value to get reliable structural parameters. The measured HXR profiles show that the Bragg peaks are well defined up to the 4th order even as the thickness of the individual layers decreases to the ultra-thin limit. The measured HXR profiles also show the well-defined Kiessig fringes at higher q_z values, e.g., between second- and third-order Bragg peaks for a number of MLs (ML-b, ML-c, ML-d, ML-g and ML-h). The Kiessig fringes (N-2 numbers) are clearly observed for ML-g and marked by vertical downward arrows shown in the inset of Figure 4.1 (b). The observations indicate well maintained periodic structure and the interfacial widths throughout the ML stacks.

In Sample set-A, it is observed that, the interfacial width of the W layers increases from 0.34 nm to 0.47 nm and the interfacial width of the B₄C layers slightly increases from 0.18 nm to 0.22 nm for ML-b to ML-d (but for ML-a the B₄C roughness is 0.23 nm) as the thickness of the W layer decreases from 2.03 nm to 1.06 nm (ML-a to ML-d) and fixed thickness of the B₄C layer of ~ 2.9 nm and number of layer pairs, N= 20. The variation of the

interfacial widths of W and B₄C layers may be owing to the affect of the thickness-dependent microstructure of the W layer. Also, this variation may be due to the increase of physical roughness and/or interfacial diffuseness as W layers thickness decreases toward the film continues limit. When the thickness of the W layer reduces from 1.38 nm toward the continuous-discontinuous transition range (thickness of W layer ~ 1 nm), there is a probability to increase the physical roughness and interfacial diffuseness in Volmer-Weber growth mode [156]. As a result, the interfacial width increases at the interface. The mass density of the W layer remains unaltered at 17.3 g/cm³ (89% of bulk density) for three W/B₄C MLs (ML-a, ML-b and ML-c) and decreases to 16.5 g/cm³ (85% of bulk density) for ML-d. This reduction of mass density for ML-d is owing to the embedding of more B₄C molecules in loosely packed W layers while the thickness of the W layer decreases toward layer continuous- discontinuous transition range. The mass densities of the B₄C layers are almost fixed for all MLs in set-A at 2.4 g/cm³ values (95% of the bulk density). This suggests that there is no significant change of the mass density of the B₄C layers due to relatively high thickness value of B₄C layer (~ 2.9 nm). In table 4.1, first-order Bragg peak for all W/B₄C MLs in set-A show the relatively high reflectivities which is due to the good quality of the ML structure in terms of interface width and mass density as well as the comparatively higher periodicity. For ML-d, reflectivity decreases due to the combined effect of the increase of the average interface width, decrease of the densities of the W layers, and the shift of the Bragg peak toward higher angle of incidence as the ML period decreases. Here, it is noteworthy that in order to reduce the number of fitting parameters for modelling of the reflectivity spectra, a two-layer iterative structure of the ML is taken instead of individual layers. In this model, the fitted profiles are well matched to the measured reflectivity spectra except the widths of the higher-order Bragg peaks. The broadening of the higher-order Bragg peaks depends on different factors such as variations of interfacial roughness at different interfaces, individual

layer thickness errors, and non-uniformity of the period. These factors are not considered for modelling. In some cases, the deviation of the measured profiles from the simulations between the successive Bragg peaks (i.e., for ML-g, between the first and second Bragg peaks) may also be due to the above factors. The error of the bilayer period (shown in Table 4.1) is found from the shift of the Bragg peak positions, especially for the higher order Bragg peaks.

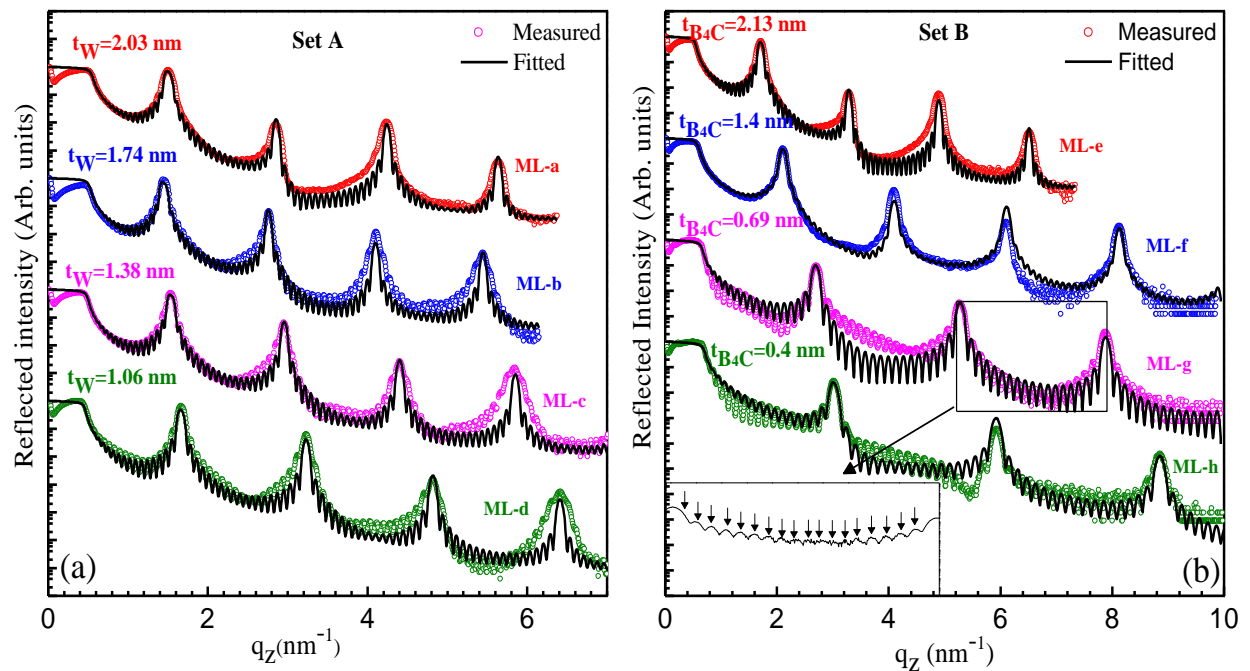


Figure 4.1 Measured (colored circles) and fitted (solid black line) HXR profiles of W/B₄C MLs with altering the thickness of the individual layer and constant $N = 20$ for Set-A and Set-B. (a) For sample set-A, the thickness of the W layer reduces from 2.03 nm to 1.06 nm (ML-a to ML-d) at a fixed thickness of the B₄C layer of ~ 2.9 nm. (b) For sample set-B, the thickness of the B₄C layer reduces from 2.14 nm to 0.4 nm (ML-e to ML-h) at a fixed thickness of W layer of ~ 1.7 nm. For ML-g, the measured Kiessig fringes ($N-2$ number) between 2nd and 3rd Bragg peak of ML-g are indicated by the vertical downward arrows in inset. The HXR profiles are vertically shifted for a clear picture.

In sample set B (ML-e to ML-h), interfacial width decreases from 0.23 nm to 0.12 nm as the thickness of the B₄C layer decreases from 2.13 nm to 1.40 nm (ML-e to ML-f), after that the interfacial width increases to 0.19 nm with decreasing the B₄C layer thickness up to 0.4 nm at fixed W layer thickness ~1.7 nm and fixed number of layer pairs N=20. The interfacial width of W layers for these W/B₄C ML samples (ML-e to ML-g) follow the similar trend of the nature of the interfacial width of B₄C layer. For, ML-h, the interface widths remain approximately equal within the error bar. The mass density of the W layers remains unchanged at 17.3 g/cm³ (89% of bulk density) for all the MLs in Sample set-B. The mass density B₄C layers remain nearly fixed at 2.4 g cm³ (95% of bulk density) for ML-e and ML-f. But the mass density of the B₄C layers increases to 3.0 g/cm³ (119% of bulk density) in case of ML-g. The mass density of the B₄C layers increases due to the energetic heavy W atoms embedded in the loosely packed B₄C layers. Again, the mass density of the B₄C layer significantly increases up to 3.9 g/cm³ (154% of bulk density) as the B₄C layer thickness decreases to 0.4 nm. The rate of increase in mass density of B₄C layer with decreasing its thickness is higher than that of ML-g to ML-h compared to ML-f to ML-g. It is indicated that more number of W atoms get embedded into B₄C layers that are more loosely packed as the B₄C layer thickness decreases from 0.69 nm to 0.40 nm. In sample set B, as the B₄C layer thickness decreases, the reflectivity at the first-order Bragg peak decreases. As the period of the MLs decreases, the faster drop in reflectivity is due to the shift of the Bragg peak towards higher incident angles as well as the combined effect of the increase of average interface width and decrease of density contrast. Since reflectivity varies as proportional to $(1/q_z)^4$, the drop of reflectivity is faster as the Bragg peak moves toward higher angles. In addition, in case of real ML structure, a slight increase in roughness has a greater effect on the reduction of reflectivity for ultra-short period MLs. This is because of the exponential dependence of reflected intensity on the roughness via the Debye–Waller factor $\{\propto \exp[-(\sigma/d)^2]\}$ [145].

However, observation of well-defined Bragg peaks at such ultra-short thickness of B₄C layer [figure 4.1 (b)] indicates that ML structures have well-defined periodicity throughout the ML stack although density contrast decrease.

Table 4.1: The best-fit results of HXR of W/B₄C MLs with varying individual layer thickness. d, t, ρ, σ and R denote ML periodicity, layer thickness, mass density, interface width and 1st Bragg peak reflectivity, respectively.

Sample set-A								
Sample Number	d (nm)	W			B ₄ C			R (%)
		t (nm)	ρ (g/cm ³)	σ (nm)	t (nm)	ρ (g/cm ³)	σ (nm)	
ML-a	4.48	2.03±0.02	17.3±0.5	0.34±0.02	2.45±0.02	2.4±0.2	0.23±0.02	75
ML-b	4.64	1.74±0.02	17.3±0.5	0.42±0.02	2.9±0.02	2.4±0.2	0.18±0.02	76
ML-c	4.31	1.38±0.02	17.3±0.5	0.44±0.02	2.93±0.02	2.4±0.2	0.20±0.02	74
ML-d	3.93	1.06±0.02	16.5±0.5	0.47±0.02	2.87±0.02	2.4±0.2	0.22±0.02	65
Sample set-B								
ML-e	3.87	1.74±0.02	17.3±0.5	0.37±0.03	2.13±0.02	2.4±0.2	0.23±0.02	64
ML-f	3.10	1.70±0.02	17.3±0.5	0.3±0.02	1.40±0.02	2.4±0.2	0.12±0.02	40
ML-g	2.4	1.71±0.02	17.3±0.5	0.35±0.02	0.69±0.02	3.0±0.2	0.17±0.02	10
ML-h	2.13	1.73±0.02	17.3±0.5	0.34±0.02	0.40±0.02	3.9±0.2	0.19±0.02	3

To analyse the nature of the interfaces and morphological structure of the layers as a function of the individual layer thickness, X-ray rocking scan measurements (diffuse scattering) are performed. The component of physical roughness is separated from the total interface width by this analysis. The total interfacial width is $\sigma = (\sigma_r^2 + \sigma_d^2)^{1/2}$ obtained from HXR. Where σ_d and σ_r are the interfacial diffuseness and physical roughness, respectively. Additionally, to obtain the morphology of the interface the in-plane correlation length ($\xi_{||}$) and the perpendicular correlation length (ξ_{\perp}) are determined. The jaggedness factor (H) has been taken as 1 for all the MLs during fitting. The measured and fitted x-ray diffuse scattering spectra for two sample sets are shown in the figure 4.2. The diffuse

scattering profiles are analysed based on the formalism by Windt *et al.* [87]. The best fit results are given in table 4.2. The results show that the physical roughness is significantly less than the interfacial diffuseness in all the W/B₄C MLs. This is because the layers are grown as very smooth layers as well as the interfacial diffuseness is very high for the ultra-thin layer thickness range. In sample set-A, the physical roughness increases as the W layer thickness decreases (except from ML-b to ML-c) for both the interfaces (B₄C-on-W and W-on-B₄C) due to the impact of the morphological change of the W layers.

Notably, the physical roughness increases 5 times as the thickness of W layer decreases from 1.38 nm to 1.06 nm (See Table 4.2). This is because as the thickness of the W layer decreases to 1.06 nm, it is near to the continuous- discontinuous thickness range [156]. In the sample set A, the observation shows that the in-plane correlation length (ξ_{\parallel}) at the B₄C-on-W interface decreases from 13.5 to 9.9 nm with decreasing the W layer thickness may be due to variation of the morphology of the W layers. On the other hand, the ξ_{\parallel} at the W-on-B₄C interface is almost equal (~17 nm) because the B₄C layer thickness is fixed in the continuous region. Again, the perpendicular correlation length (ξ_{\perp}) decreases from 86 to 59 nm when the thickness of the W layers decreases. In the same way, in set B, as the thickness of the B₄C layer decreases from 2.13 nm to 0.40 nm the variation of the physical roughness and interfacial diffuseness is analogous to that of the interfacial widths taken from HXR.

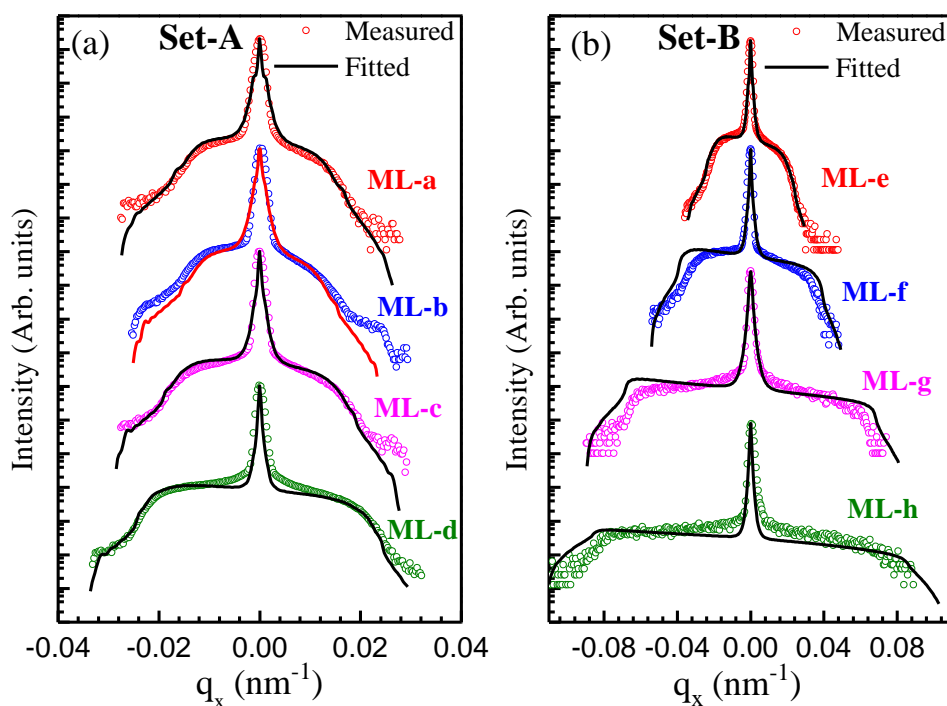


Figure 4.2 Measured (colored bubble) and fitted (solid black line) x-ray diffuse scattering spectra of W/B₄C multilayers. (a) set-A (b) set-B.

Again, it is observed that as the thickness of the B₄C layers changed, there was no significant variation in physical roughness and interfacial diffuseness, which may be due to the amorphous structure of the B₄C layer as compared to the nano-crystalline W layers. In sample set-B, the value of the ξ_{\parallel} at the interface of W-on-B₄C slowly decreases from 6.1 to 2.5 nm due to the morphological variations of the B₄C layers, whereas the ξ_{\parallel} at B₄C-on W interfaces is almost unchanged at ~ 6 nm. Conversely, the value of the ξ_{\perp} decreases extensively from 46 nm to 2 nm with decreasing of the B₄C layers thickness. By comparing the two sample sets, it is observed that both the in-plane correlation length and the perpendicular correlation length are smaller in set-B compared to the set-A. It is noted that the in-plane correlation length is strongly interrelated to the interfacial morphology and the atomic arrangement in the layer. As the thickness of the layer decreases gradually towards the

quasi-discontinuous/discontinuous thickness range, the layers are grown as a small island (nearly connected/disconnected network) that modifies the morphology of the surface. The small in-plane correlation length indicates that the same morphological feature is repeated at very low spatial intervals. In a ML structure, each rough interface participates in the scattering phenomena. Therefore, it is essential to understand the connection between the in-plane correlation length and the perpendicular correlation length. Here, it is noted that the cross-correlation function (i. e. connection between the in-plane correlation length and the perpendicular correlation length) [157] exhibits the degree of repetition of roughness from one interface to another. In the present study, the perpendicular correlation lengths are much larger than the interval between the consecutive interfaces for sample set A. This reveals that the roughness of the different interfaces is correlated with the nonzero cross-correlation coefficient. For set-B, the values of the perpendicular correlation lengths are very short and decrease faster with decreasing thickness of the B₄C layer. This recommends that the roughnesses of the different interfaces are either partially correlated or increasingly uncorrelated. Therefore, the coefficient of cross-correlation function may be gradually reduced to zero as the B₄C thickness decreases.

Table 4.2 X-ray diffuse scattering performance results. σ_r and σ_d are physical roughness and interfacial diffuseness, respectively. ξ_{\parallel} and ξ_{\perp} are in-plane and perpendicular correlation lengths, respectively.

Sample set-A

Sample No.	W-layer			B ₄ C-layer			ξ_{\perp} (nm)
	σ_r (nm)	σ_d (nm)	ξ_{\parallel} (nm)	σ_r (nm)	σ_d (nm)	ξ_{\parallel} (nm)	
ML-a	0.016±0.001	0.34±0.02	13.5±0.7	0.015±0.002	0.22±0.02	16±2	86±4
ML-b	0.035±0.002	0.42±0.02	12.5±0.5	0.039±0.002	0.17±0.02	17±2	76±4
ML-c	0.034±0.002	0.44±0.02	11.0±0.4	0.028±0.002	0.19±0.02	17±2	66±4
ML-d	0.186±0.01	0.45±0.02	9.9±0.5	0.13±0.01	0.20±0.02	16±2	59±2

Sample set-B

Sample No.	W-layer			B ₄ C-layer			ξ_{\perp} (nm)
	σ_r (nm)	σ_d (nm)	ξ_{\parallel} (nm)	σ_r (nm)	σ_d (nm)	ξ_{\parallel} (nm)	
ML-e	0.034±0.002	0.36±0.02	6.4±1	0.045±0.002	0.22±0.02	6.1±0.3	46±3
ML-f	0.044±0.002	0.29±0.02	6.0±1	0.038±0.002	0.11±0.02	4.4±0.6	12±2
ML-g	0.030±0.002	0.34±0.02	5.9±1	0.034±0.002	0.16±0.02	3.3±0.4	4±1
ML-h	0.045±0.002	0.34±0.02	6.4±1	0.033±0.002	0.18±0.02	ξ_{\parallel} (nm)	2.2±1

In the present study the interface quality is improved compared to another study [156] near the thickness of the layer continuous limit for W/B₄C MLs with N = 10. This is because of the further improvement of the conditioning of the deposition chambers and/or target materials to reduce out-gassing from inner surfaces, improvement of the plasma stability and slightly better quality of the substrate. The different values of correlation lengths of W/B₄C MLs in the present work may be due to the different qualities of interfacial morphology and the different N. This is because the quality of the surfaces / interfaces depends on the deposition conditions and the quality of the substrate, which can induce morphological change at the interfaces of W and B₄C layers.

The residual stress in the layer structure also depends on the structural arrangement of atoms/molecules in the layers, which is analysed by grazing incidence x-ray diffraction (GIXRD). A typical measured GIXRD profile at $\chi = 0^\circ$ for ML-c is shown in the figure 4.3 (a).

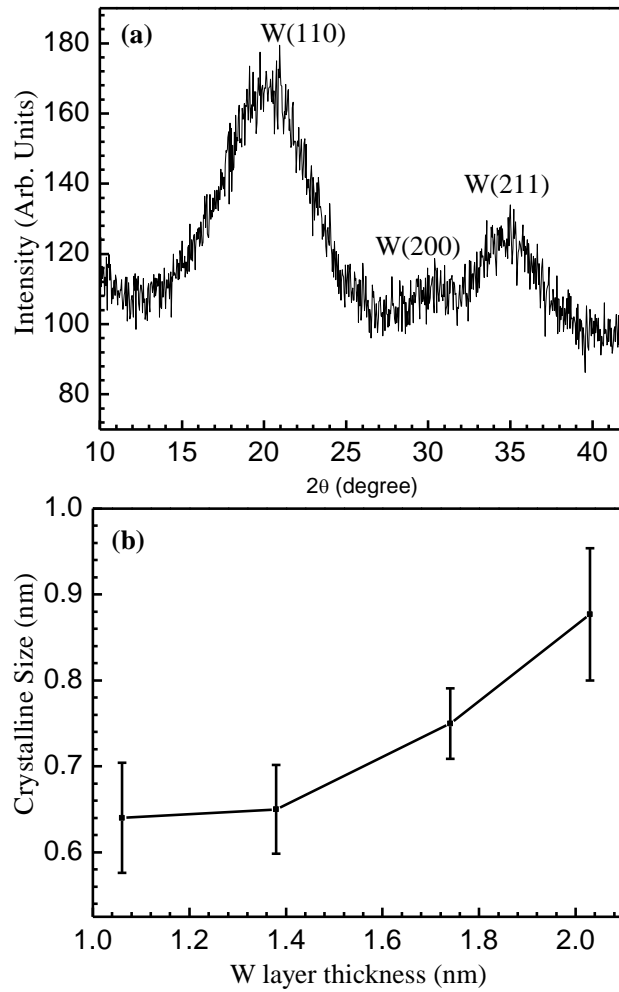


Figure 4.3 (a) Measured GIXRD profile of the ML-c at energy 15.4 keV at $(\alpha) = 0.6^\circ$ and at $\chi = 0^\circ$. (b) Crystallite size with considering W (110) plane as a function of thickness of the W layer.

The GIXRD profile shows that the W layers are formed as nano-crystalline in nature. Three peaks are observed as W (110), W (211) and W (200) for energy 15.4 keV. It is seen that the α phase is dominated in the present W layers [153], as indicated by measured peak positions. The crystalline size of the nano-crystalline W layers near the ultra-thin thickness range is estimated to understand its effect on the layer stress. It is observed that the diffraction peaks

are broadened may be due to contributions of small grain size and the broadening can be manifested by the Scherrer equation [101]. The Scherrer equation is written as

$$\Delta(2\theta) = 0.9\lambda / (L \cos\theta_B) \quad (4.1)$$

where $\Delta(2\theta)$ is the full width half maxima of the diffraction peak, λ corresponds to the wavelength, L denotes the average grain (crystallite) size and θ_B is the angle of Bragg diffraction. The figure 4.3 (b) shows the variation of crystallite size as a function of the thickness of the W layer. It is noted that the measured absolute values of the out-of-plane crystalline size may be overestimated. This is because of the contribution of the other affects such as lattice distortion and influence of the instrumental effects (wavelength spread, slit width, etc). However, the trend of the variation of the crystal size and its value as a function of the W layer thickness gives the essential information for understanding and correlating the residual stress and morphology of the layer. The crystallite size is smaller than the W layer thickness as shown in the figure 4.3 (b). As the W layer thickness increases from 1.06 nm to 1.38 nm the crystallite size in out-of-plane is nearly equal due to growth of island structure in the lateral directions to form a continuous layer. Further, the out-of-plane crystallite size increases with increasing thickness of the W layer up to 2.03 nm because of island growth of W crystallites in the perpendicular direction. Conversely, the B₄C layer forms as amorphous nature. So, the different growth morphology of W and B₄C layers may have different effects on the evolution of stress.

4.3.2: Residual stress analysis:

The evolution of residual stress and its correlation with microstructure has been investigated by determining both the total residual stresses of the MLs and the stresses in the W layers with varying the individual layer thickness. To determine the total residual stress, the radii of the curvature of the substrate is measured before and after ML fabrication. The surface

profile of substrate before and after the deposition of two MLs (ML-a and ML-e) is shown in the figure 4.4. The figure 4.4 shows the significant variation in the surface profile of the substrate before and after ML deposition. This is mainly because of the presence of residual stress in the ML structure. To assess the total average residual residue in MLs, the surface shape profile was subsequently fitted to the Zernike polynomial. Then, the radius of curvature is determined through extracting the spherical component of the surface profile.

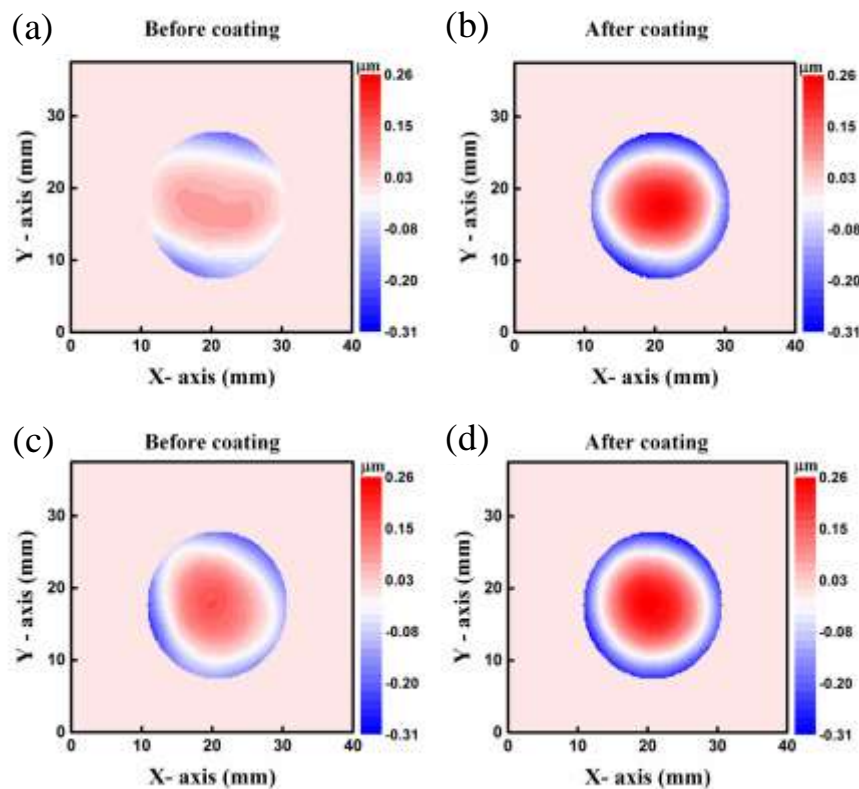


Figure 4.4 Two dimensional surface contour plot of W/B₄C MLs. [(a) before deposition and (b) after deposition] for ML-a and [(c) before deposition and (d) after deposition] for ML-e. The height of the surface profile is indicated by the colour contrast.

Similarly, the GIXRD measurements are carried out at different χ orientations for the determination of stress in W layers of W/B₄C ML stacks. It is mentioned that the high-intensity W (110) peak [Figure 4.3 (a)] is taken to determine the residual stress in W layers.

Here, it is noted that the higher-order Bragg diffraction peak W (220) is sharper than W (110). Thus, it would be more appropriate to determine the residual stress.

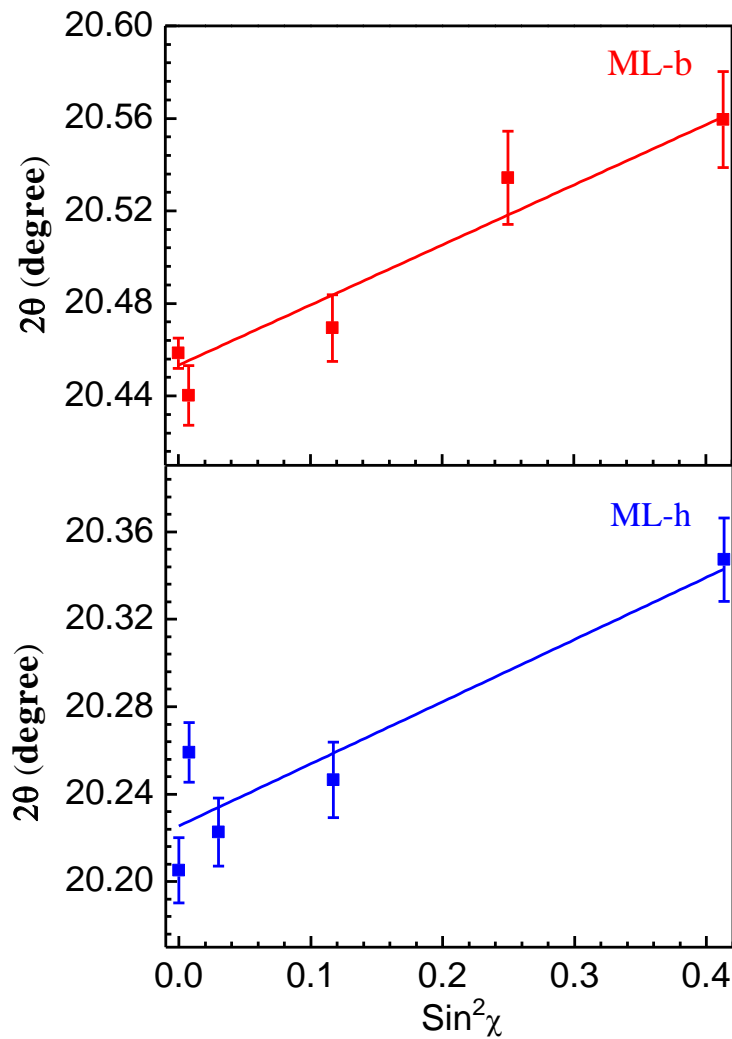


Figure 4.5 Variation of the diffraction peak position (2θ) relating to the W (110) with $\sin^2\chi$ for two multilayers b and h.

Nevertheless, the signal-to-noise ratio of the measured diffraction peak corresponding to W (220) plane decreases considerably for $\chi \geq 15$; as a result it has been ignored in the present study to determine the stress. The variation of the diffraction peak (2θ) of the W (110) plane vs. $\sin^2\chi$ for two particular MLs (ML-b and ML-h from each set) is shown in the figure 4.5. In figure 4.5 the errors are estimated by considering the uncertainty in determining the

positions of the wide diffraction peaks. The residual stress in the W layers is determined by the equation 2.33 [indicate from chapter 2] using the slope obtained from the measured 2θ vs. $\sin^2\chi$ plot. The figure 4.6 shows the variations of the total residual stress and the stresses in the W layers with varying the individual layer thickness. Fig. 4.6 (a) shows the variations of the total residual stress and stress in W layers with varying thickness of W layer (set-A). Also the stress variation with varying the B₄C layer thickness (set-B) is plotted in Fig. 4.6 (b). Both the figures (a and b) show that the total stress is compressive in nature as well as the stress in the W layers are also compressive in nature. Both the stresses undergo a significant variation as a function of individual layer thickness. Again, the value of total residual stress is lower than that of the W layers. In Fig. 4.6 (a), the total residual stress (stress in W layers) enhances from -2.625 ± 0.079 GPa (-3.6 ± 0.53 GPa) to -3.15 ± 0.14 GPa (-3.85 ± 0.14 GPa), respectively as the W layer thickness increases from 1.06 to 1.38 nm. When the W layer thickness increases up to 2.03 nm, the total residual stress (stress in the W layers) decreases to -1.24 ± 0.051 and -2.35 ± 0.38 GPa, respectively. In the case of W/B₄C MLs in set-B [Fig. 4.6 (b)], it is observed that the residual stress in the W layers varies as a different non-monotonic behaviour compared to the total residual stress. For example, the total residual stress (stress in W layers) rises from -0.78 ± 0.09 GPa (-2.01 ± 0.53 GPa) to -1.47 ± 0.07 GPa (-2.84 ± 0.52 GPa), respectively when the B₄C layer thickness increases from 0.40 to 0.69 nm. However, on further increasing the thickness of the B₄C layer up to 2.13 nm, the stress in the W layers is slightly increased within the experimental error bar limit. The total residual stress increases to -1.73 ± 0.09 GPa when the B₄C layer thickness increases to 1.40 nm. Thereafter, the total pressure decreases to -0.88 ± 0.09 GPa as the B₄C layer thickness increases to 2.13 nm. Also, in figure 4.6 (b), the stress curve has extended using the measured stress of ML-b from set-A as the B₄C layer and W layer thicknesses are 2.9 nm and 1.7 nm, respectively. It is observed that the total residual stress in the W/B₄C ML increases to $-2.3 \pm$

0.08 GPa whereas the stress in the W layers decreases slightly within the error bar limit as B₄C layer increases to 2.9 nm.

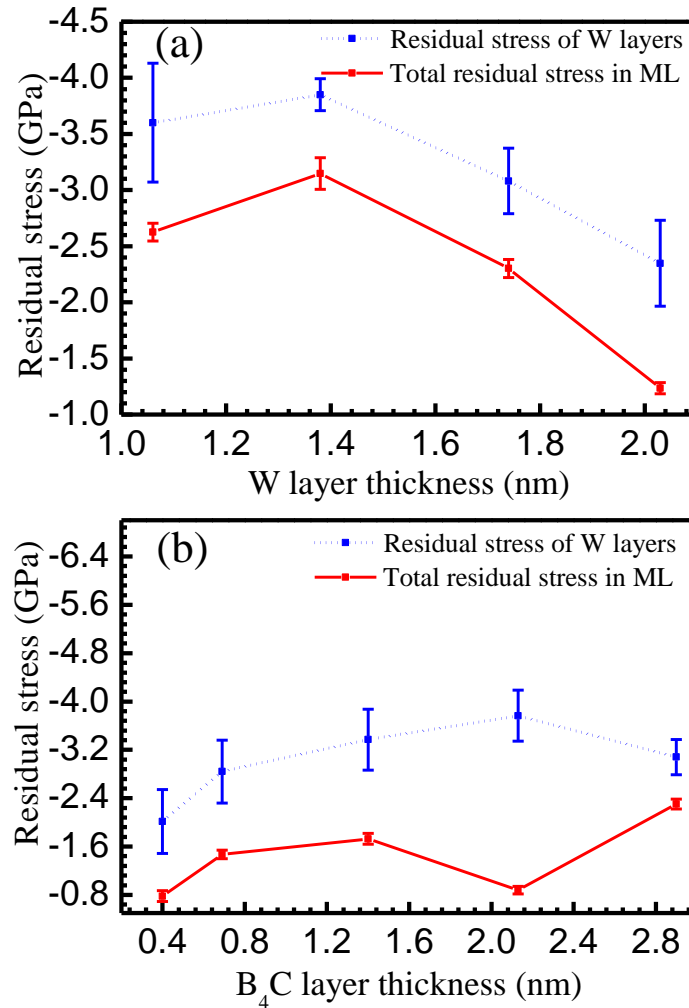


Figure 4.6 Variations of residual stress as a function of the individual layer thickness. (a) Set-A, with varying the W layers thickness at unchanged thickness of the B₄C layer of 2.9 nm. (b) Set-B, with varying the B₄C layers thickness at a fixed thickness of W layer of 1.7 nm. In (b), the stress value of ML-b is re-plotted from set-A for extrapolation of B₄C thickness up to 2.9 nm. The solid line with data points and the dotted line with data points represent the total residual stress and stresses in the W layers of the ML stack, respectively.

4.4.3 Correlation between the Stress and microstructure:

It is now discussed to understand and explain the origins and evolution of compressive residual stress with micro structural relationship. The total residual stress in the ML stack is contributed by the parts. (a) Stress presents in the individual layers which originated during the growth process. (b) Another is the interfacial stress that presents at the interface of successive layers. The stresses in the layer can be thickness dependent [69]. In a ML stack it can be determined separately for each type of material if the layers are crystalline structure. On the other hand, the stresses at the interface depend upon the extent of the interfacial roughness, diffuseness and chemical interactions. In the present study, the in-plane stresses in individual W layers are investigated by the GIXRD technique, because the W layers are nano-crystalline structure. However, determination of the stresses in the B₄C layers using GIXRD technique is not possible due to its amorphous structure. However, the nature of the net combined stresses arising from both the B₄C layer and the interface can be analysed qualitatively by deducting the measured stress in the W layers from the total stress of the MLs.

The evolution of thickness-dependent residual stress emerges through microstructural change of the layer and morphology of surface at the early stage of the film growth. This structural change undergoes through a series of film growth mechanism such as nucleation, island growth, coalescence of islands and continuous layer formation [50]. The W layer is in the discontinuous-to-continuous transition region when the W layer thickness is 1.06 nm [156-159]. In figure 4.6 (a), at this thickness, the compressive residual stress is originated in the W layers. This is due to the growth of the small and almost connected islands of nano-crystallite grains in the out of plane direction [Fig. 4.3 (b)]. Pradhan *et al.* [156] observed a well-defined layer structure of W/B₄C ML with good density contrast at the interfaces by using transmission electron microscopy [TEM] which gives experimental evidence of the

connected island structure at the W layer thickness of ~ 1 nm (near the discontinuous-to-continuous transition region for layer formation). Since the energetic (~ 10 - 12 eV) B_4C molecules come to the W surface with this type island morphology, they get embedded between the neighbouring W islands. As a result, it is observed by HXR (Table 4.1) that the W layer density decreases (compared with a continuous W layer). Again, when the thickness of W layer increases to 1.38 nm, the W layer becomes more packed and their density increases which is observed by HXR (Table 4.1). In figure 4.3 (b), the GIXRD results reveal that, the out-of-plane crystallite size remains almost same as the thickness of the W layer enhances from 1.06 nm to 1.38 nm. This suggests that since the thickness of the W layer increases from 1.06 nm to 1.38 nm, the W adatom occupy the gaps between the loosely packed W islands, therefore, the size of the islands increases in most lateral directions. As a result, the in-plane correlation length of B_4C -on-W interfaces is also increased with increasing the island size in the lateral direction (Table 4.2, ML-d to ML-c). The density of the W layers increases through the increment of island size and/or formation of new clusters within the gaps between islands. Therefore, as the W layer thickness increases to 1.38 nm, the compressive stress in the W layers also increases [Fig. 4.6 (a)]. A schematic model can assist to understand the growth mechanism and helps to explain the observed facts regarding the stress microstructure correlation, shown in the figure 4.7. In this figure, it is shown that the schematic model of the morphology of the W layer at thicknesses of 1.06 nm (near the discontinuous-to-continuous transition region) and 1.38 nm (the onset of continuous region), where the B_4C layer thickness is unaltered in the continuous region. In Figure 4.7 (a), as the thickness of the W layer is adjacent to the discontinuous-to-continuous transition region (thickness of ~ 1.06 nm), some B_4C molecules get embedded in the layers of the loosely packed W, which reduces the W layer density. In figure 4.7 (b), when the thickness of the W layer is increased to 1.38 nm, the W layer is formed as denser continuous layer due to the

addition of more W adatoms to fill the gap between the islands. Thus, the B₄C molecules is restricted to implant only in the interfacial region and not deeper inside the W layer. Further, as increasing W layer thickness through 1.74 nm to 2.03 nm, the HXR results show that the density of the W layers is almost the fixed (Table 4.1) due to the more densely packed continuous nature of the W layers. In this thickness region, when the W layers thickness increases up to 2.03 nm, it is observed that the out-of-plane crystallite size increases [Fig. 4.3 (b)], indicating that the growth of grains is mainly in the vertical direction. Thus, the reduction of compressive stress in the W layers is observed as the thickness of W increases to 2.03 nm [Fig. 4.6 (a)]. Though, it has been observed that the total compressive residual stress is appreciably less compared to the residual stress in the W layers. This is because of the compensation by resultant tensile stress originating from contributions of stress in the B₄C layers and interfacial stress. It is noteworthy that the elastic constants of the thin film [160] are used to determine the residual stress in the W layers because the elastic properties of the thin film are modified due to the microstructural change as compared to the bulk materials. Earlier, it is observed that the elastic constants are microstructure sensitive, which is interrelated to the layer formation through island-coalescence process from an initial discrete island towards a continuous film [161, 162]. So the elastic properties change with varying layer thickness. As a result, the residual stress is strongly related to the film's microstructure, which depends on the film thickness.

On the basis of the phase formation of W layers, Windt [153] discussed the nature of stress in sputtered deposited W layers in the W/Si ML. It is observed in his study that W layers contain both the α - and β -phases by varying the thickness of the W layer from 7 nm to 2.5 nm at a fixed thickness of Si layer of 3 nm. On the other hand, analysis of the measured data suggested that as the thickness of the W layer decreases, the α phase of W layers becomes more compressive and the β phase becomes more tensile.

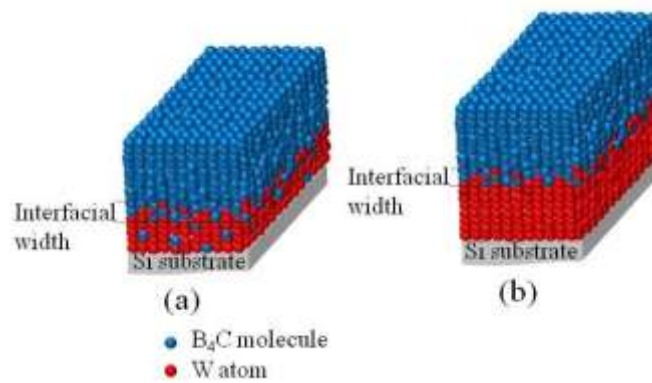


Figure 4.7 Schematic of a B₄C layer on a W layer at two different important growth stages. (a) At the W layer thickness of ~ 1.06 nm, discontinuous-to-continuous transition. (b) At the W layer thickness of ~ 1.38 nm, onset of formation of the continuous layer.

In the present work of the W/B₄C MLs, the thickness of the W layer is much smaller in the range of ~ 1.06– 2.03 nm. The residual stress is measured in W layers as compressive in nature which may be owing to the presence of only the α phase of W, observed by GIXRD spectra [Fig. 4.3 (a)]. Additionally, it is mentioned that the measured residual stress in W layers is compressive, but the lattice constant obtained from GIXRD at $\chi = 0^\circ$ [Fig. 4.3 (a)] is larger compared to the bulk value. The atomic peening model [68, 163] can explain the above observed phenomena. During the deposition the grown W layers are bombarded by Ar neutral atoms or/and sputtered atoms/ molecules, which can create compressive stress and increase the lattice constant. Previously, a same thing happened in the case of a sputtered deposited W thin film [161]. Also, a similar higher compressive stress in W layers was also observed in W/Cu MLs compared to the total stress of the ML structure [152].

In set-B [Fig. 4.6 (b)], the total stress of MLs varies in similar manner to that of set-A with changing the thickness of the B₄C layer from 0.4 nm to 2.13 nm. The value of total stress in MLs of set-B is less than that in set-A, may be due to the amorphous structure of the B₄C layer as compared to the nano-crystalline nature of the W layer. In set-B, it was to be

expected that the stress would be almost fixed in the W layers as varying the B₄C layer. This is because the thickness of the W layer is kept unaltered. Nevertheless, it has been observed that the stress of the W layer increases with increasing the B₄C layer thickness from 0.4 nm to 0.69 nm. This is because the B₄C layer is in quasi-discontinuous thickness range since the thickness of the B₄C layer very small (0.4 nm). At this very small layer thickness, the density of the B₄C layer increases significantly as W atom is embedded in the B₄C layer (Table 4.1). Thus, the stress of the W layers can be affected by the microstructure of the quasi-continuous B₄C layer. To compare the stress value, the measured stress of ML-b is re-plotted at B₄C thickness of 2.9 nm (Fig. 4.6 (b)). It is observed that the stress in the W layers slightly decreases within error bar limit, while the total stress increases significantly as the thickness of the B₄C increases up to 2.9 nm. This reveals that the resultant tensile stress (contributed from B₄C layers and interfaces) decreases due to the influence of the microstructure of layers and interfaces when the thickness of the B₄C layer increases.

In contrast, previously Zhang *et al.* [151] measured compressive residual stress in sputter deposited (Ar pressure $\sim 6.65 \times 10^{-5}$ mbar) B₄C thin film with thickness ~ 30 nm to 120 nm and in B₄C/Cr MLs with altering the B₄C layer thickness in the range 30 nm to 90 nm and thickness of the Cr layer of 20 nm to 80 nm. In the present work, the thicknesses of the B₄C layers are very small in the range ~ 0.4 nm to 3.0 nm and the layers are deposited with deposition rate of ~ 0.5 nm/min and Ar gas pressure 4.3×10^{-3} mbar. It is well-known that the stress state in a film significantly depends on the deposition rate [149], power sputtering [164], film thickness [153] and growth microstructure [162]. Additionally, it has been observed that the nature of interfacial stress may be compressive [69] or tensile [71] which depends upon the material combinations, individual layer thickness and the formation of interfacial structure at the early stage of film growth.

4.4 Conclusions:

In conclusion, the evolution of residual stress and its correlation with microstructure are simultaneously investigated with varying the individual layer thickness of ultra-short range ($\sim 0.4\text{--}3$ nm) in periodic W/B₄C MLs. To understand the nature of the stress contribution by each type of material in the layer and the interface to the total stress in the MLs, the stresses of the nano-crystalline W layers and the total stress in the MLs are determined separately. The stresses in B₄C layers are not able to estimate separately due to its amorphous nature. However, the nature of the resultant stress contributed from the combination of the B₄C layer and the interface has been analyzed. The evolution of stress and its microstructural correlation are explained using a growth model at the early stage of film formation. It is observed that the total stress is compressive and lower than the stress in W layers. The resultant stress contributed by B₄C layers and interfaces is tensile. Also the atomic peening mechanism dominates compared to the effect of the growth mechanism for arising the high compressive stress in W layers as indicated by measured compressive stress and the observation of a W crystallite plane at lower diffraction angles than the bulk.

Chapter-5

Study of residual stress-microstructure correlation in ML mirrors with large layer pairs:

This chapter discusses the study of the residual stress with varying number of layer pairs (N) in ultra-short period W/B₄C MLs, required for the development of soft gamma-ray ML optics. Similar to the previous chapter, the total residual stresses in the MLs are determined by the substrate curvature measurement technique. Also, the stress in W layers of MLs is obtained by grazing incidence x-ray diffraction (GIXRD) measurements. The microstructure is also analyzed by the hard x-ray reflectivity (HXR) and diffuses scattering techniques. The contributions of stress originating from layers and interfaces are correlated with the total stress in the ML stack. It is observed a non-monotonic decrease of total residual stress with increasing N from 20 to 400. The value of the total residual stress decreases from -1.444 GPa to -0.389 GPa with increasing $N = 20$ to 400 at constant periodicity of $d \sim 1.9$ nm. The variation of stress with N may be due to stress compensation as more and more interfaces formed. Similarly, at a constant $N = 300$, as the period decreases from 1.97 nm to 1.2 nm, the residual stress also decreases.

5.1 Introduction:

Today's ultra-short period larger number of layer pairs multilayer (ML) optics (period thickness (d) \sim 1–2 nm, and the number of layer pairs, N from 300 to 400) finds potential application in high energy application such as soft gamma-ray energy range (100- 600 keV). Recently, highly efficient ML optics is used to explore its application in the emerging frontier areas of both nuclear physics [9, 18] as well as high energy astrophysics [19, 20] of soft gamma-rays (100- 600 keV) energy range. For these applications, highly efficient ML optics is required to deliver higher photon flux to enhance the signal-to-noise ratio. This is due to the weak gamma-ray signal comes from the distant stellar object and from the nuclear spent fuel as compared to the background radiation. Now, it is mentioned that the actual optical performance of the ML optics not only depends on good optical contrast and surface/interface quality but also strongly depends on a critical parameter called the residual stress. The study of residual stress is very important for ML optics especially when the ML stack consists of a large N, which can unfavourably affect the performance of the ML optics. For example, the residual stresses can reduce the angular or spectral resolution and peak intensity by increasing the width of the reflectivity peak, can generate cracks and buckle in the films [24]. Due to the high residual stress, ML may become unstable over time and may be peel off from the substrate [26]. Thus, in order to achieve low residual stress for better performance of ML mirrors for high energy applications, it is significant to understand the evolution of the residual stress and stress-structure correlation. Therefore, in this chapter, the residual stress has been studied in ultra-short period W/B₄C ML optics with varying N. This is because the W/B₄C ML is one of the most important material candidate which gives good optical contrast at the interface, smooth interface and chemical stability [154].

Previously it is observed that the residual stress in the ML structure strongly depends on the various deposition parameters such as gas pressure, temperate, deposition rate, power

and microstructure of the ML structure [149, 150, 153, 164]. Commonly used methods for determining the residual stress are substrate curvature method for measuring the total residual stress of the ML [92, 93] and grazing incidence x-ray diffraction (GIXRD) based on the $\sin^2\chi$ method for measuring the residual stress in the layers of individual material if the layers are crystalline in nature. Previously, in the B_4C based ML structure, the residual stress has been studied in sputtered deposited Cr/ B_4C ML by varying Cr thickness from 20 nm to 80 nm at fixed B_4C layer thickness (three different values 30 nm, 60 nm, and 90 nm) as well as in single layer of Cr (thickness 6.2 nm to 127.1 nm) and B_4C (thickness 30 nm to 120 nm) [151]. They observed that for Cr single layer the tensile stress decreases from 3.9 to 1.0 GPa with increasing Cr thickness. But in case of B_4C layer compressive stress is 3.2 GPa which is independent of its thickness. Nevertheless, in the case of MLs, the total residual stress not only depends on the stress of B_4C and Cr layers but also on the stress of the interface between adjacent layers. This is because the total residual stress of MLs varies significantly with increasing B_4C layer thickness and also varies from tensile to compressive after a particular thickness of the Cr layer. The interfacial stress in Cr/ B_4C ML changes from 15 N/m to 90 N/m as the B_4C layer thickness increases from 30 nm to 90 nm. Here, the interfacial stress is expressed in terms of the force per unit width at the interface. In general, the total residual stress in the MLs is contributed by the stresses in the individual layers and the interfaces between the consecutive layers. Previously, it is observed that the interfacial stress could be determined from the difference between the measured total stress in the ML film and stresses in layers. For example, in case of sputtered deposited Ag/Ni ML films compressive interfacial stress (-2.27 ± 0.67 N/m) is observed with changing period from 4 nm to 15 nm [69]. Also, in Ag/Cu MLs, compressive interfacial stresses are observed as -3.19 ± 0.43 N/m [43] and -0.21 ± 0.1 N/m [165]. This difference of the absolute value of the interfacial stresses comes due to the difference in formation of interfaces at the early stage of film

deposition. Conversely, in sputtered deposited Cu/Cr ML with a period of 20 nm, a tensile interfacial stress (2.6 N/m) is observed having a total residual stress ~ 697 MPa [71]. Subsequently, it is observed that the interfacial stress is more important for low period MLs. Thus, it is now obvious that the nature of interfacial stress in MLs depends on the interface structure, material composition, and the individual layer thickness.

In the case of the W-based MLs, Girault *et al.* [152] studied the residual stress in sputtered deposited W/Cu MLs as a function of W layer thicknesses from 12 nm to 1.5 nm with fixed thickness of the Cu layer at 1 nm and 0.5 nm, respectively. It is observed that the strong compressive stress is generated in W layers, e.g. the stress in W layers is - 6.8 GPa whereas the total stress in the ML film is - 3.2 GPa for ML with period $d = 2$ nm ($t_w = 1.5$ nm and $t_{Cu} = 0.5$ nm) and $N = 90$. Similarly, in case of sputtered deposited W/Si ML [153] the nature of residual stress in W layers has been analyzed based on the phase formation of W layers. In the case of sputtered deposited Al/SiC MLs, the nature of the residual stress is interpreted by the atomic peening mechanism [68]. Previously, a very little work of stress-structure analysis is reported for W/B₄C MLs [155].

In this chapter, both the microstructure and residual stress in W/B₄C MLs are studied concurrently with varying $N = 20 - 400$ which is essential for the development of ML optics with larger N . To understand the correlation between the residual stress in crystalline W layers and the total residual stress of W/B₄C ML, the residual stresses are measured independently by the GIXRD and the substrate curvature methods. The variation of total stress in the ML stack with varying N is explained by considering both the stresses in layers and the interface stress. The stress-structure is also correlated considering the evolution of the microstructure in the ML structure along with the film growth mechanism.

5.2 Experimental details:

Periodic W/B₄C MLs are fabricated with varying number of layer pairs (N) from 20-400 at fixed periodicity ~ 1.9 nm. The MLs are deposited on ultrasonically cleaned Si (100) substrates using a magnetron sputtering system [76]. The structural parameters are measured using the hard x-ray reflectivity (HXR) and diffuse scattering (rocking scan) measurements [see sections 2.5.3 and 2.5.4] at incident energy 8.047 keV (Cu K source). For fitting of the rocking scan has been carried out by considering the jaggedness factor (H) = 1. The total stress in the W/B₄C MLs is measured by the substrate curvature technique using a Zygo Mark-II laser Fizeau interferometer [92, 93] by determining the radii of curvature of the substrate before and after deposition of MLs using the Stoney equation [94, 95]. The more details of the substrate curvature method are described in the previous chapter (experimental section chapter-4) and the chapter-2 (section 2.5.8.1). After that grazing incidence X-ray diffraction (GIXRD) based $\sin^2\chi$ method is used to determine the residual stress in the W layers using INDUS-2 BL-12 synchrotron source [103]. The measurements are performed at energy 15.695 keV with a fixed incident angle at 4.5°. The three diffraction peak positions considering W(110), W(211), and W(220) planes are measured using a Mythen detector. Here, the W(211) peak is used to determine the stress by taking into consideration of the signal-to-noise ratio at higher χ values (>15). It is observed that the intensities of diffraction peaks are very weak and in few cases disappear at a certain higher χ (>15) for ML having the total thickness is very small (N < 50). Therefore, GIXRD measurement is also carried out at incidence angle of 0.6° to enhance the diffraction intensities, and the diffraction peak W(110) is taken for stress analysis of MLs with N= 20 and 50. During the measurements the incident energy was 15.4 keV for MLs with N < 50. The χ angle varies from 0° to 40° during the measurements. The residual stress is examined using the W (110) diffraction peak for MLs

with $N= 20$ and 50 as well as using $W(211)$ for MLs with $N = 50, 100, 300,$ and 400 at different χ rotations. The diffraction peaks are analysed by the Gaussian peak fitting.

5.3 Results and discussion:

5.3.1 Microstructure analysis:

To obtain the structural parameters of W/B_4C MLs with altering N from $20 - 400$ at a constant periodicity ~ 1.9 nm, the hard x-ray reflectivity (HXR) and diffuse scattering measurements are performed at 8.047 keV. The measured HXR profiles along with best fitted profiles of W/B_4C MLs are shown in figure 5.1. The reflectivity profiles have been plotted with varying q_z . The reflectivity profiles exhibit well defined Bragg peaks up to 3^{rd} order although the period is small. This indicates good quality of MLs. Also, the well-defined Kiessig oscillations are clearly observed for ML with $N=20$ up to the second Bragg peak which reveals a good control over the thickness of the deposited layers. The best fit results of HXR profiles are given in the table 5.1. It is seen that the densities of W and B_4C layers are 16.5 g/cm^3 (85 % of bulk value 19.3 g/cm^3) and 3.0 g/cm^3 (119 % of bulk value 2.52 g/cm^3), respectively for all the ML samples. The density of the W layers increases whereas the density of the B_4C layers decreases. This is because of the diffusion of W atoms in B_4C layers and vice versa as one type of material deposited on other near the continuous limit of layer structure due to loosely packing densities at ultra-thin thickness limit. Here, the two-layer model is considered for fitting by altering mass density to account the extent of embedded W atoms in B_4C layer and vice versa. Therefore, the optical contrast at the interfaces decreases as compared to the ideal value due to the inter-diffusion. It is also observed that the densities of the layers remain unaltered for all the MLs. This indicates that there is no significant change in intermixing of two layers with increasing N . The interfacial width of the B_4C layer increases from 0.15 nm to 0.22 nm whereas the interfacial width of the W layers increases

from 0.26 nm to 0.44 nm, with varying N from 20 to 100. For MLs with N=300 and 400, the HXR profiles are fitted by allowing for random layer thickness error ~ 0.006 nm and 0.013 nm, respectively. The thickness error in MLs having larger N = 300 and 400 takes place owing to slightly alteration in the rate of deposition during deposition for a long time, (~ 16 -20 hrs) for ML with N=400. In the present two-layer model, it is noted that the ML stack may have variations of roughness from one bilayer to another but could not be considered for fitting. Further, the roughnesses of the both W and B₄C layers remain nearly unchanged as N increases up to 400. Also, a weak modulation of HXR profile is observed between 1st Bragg peak and the critical angle for ML with N=400 due to the very thin contaminated layer on the top of ML surface with thickness ~ 4.4 nm, density ~ 3 g/cm³ and interface width ~ 0.53 nm.

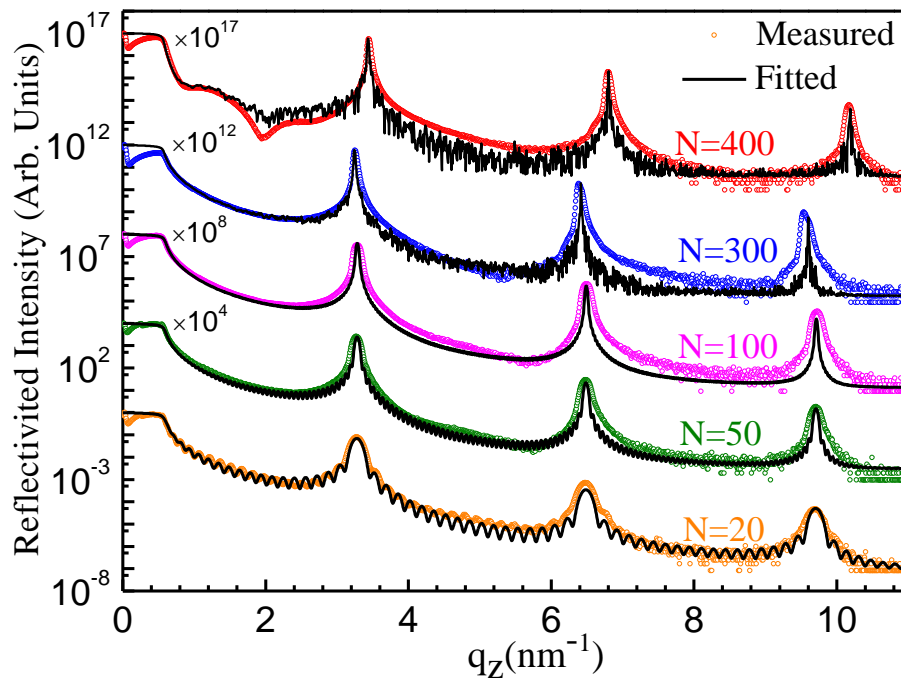


Figure 5.1 Measured (coloured bubbles) with fitted (black solid lines) HXR profiles of W/B₄C MLs as a function of N from 20 to 400 at unchanged period of $d \approx 1.9$ nm. Random layer thickness errors are considered as 0.006 nm and 0.013 nm for MLs with N=300 and 400, respectively during the fitting. In case of N =20, 50 and 100, the measured HXR spectra are fitted with a constant period.

Table 5.1 The best fit results of HXR of W/B₄C MLs with varying N. d, t, ρ and σ denote as ML period, layer thickness, mass density and interfacial width, respectively.

N	d (nm)	W layer			B ₄ C layer		
		t (nm)	ρ (g/cc)	σ (nm)	t (nm)	ρ (g/cc)	σ (nm)
20	1.94	1.07±0.02	16.5±0.6	0.26±0.03	0.87±0.02	3.0±0.2	0.15±0.02
50	1.94	1.07±0.02	16.5±0.6	0.32±0.03	0.87±0.02	3.0±0.2	0.17±0.02
100	1.94	1.09±0.02	16.5±0.6	0.44±0.04	0.85±0.02	3.0±0.2	0.22±0.02
300	1.97	1.01±0.02	16.5±0.6	0.40±0.03	0.96±0.02	3.0±0.2	0.22±0.02
400	1.85	0.95±0.02	16.5±0.6	0.35±0.04	0.90±0.02	3.0±0.2	0.20±0.03

Now, the detailed analyses of the diffuse scattering spectra are carried out at the first Bragg peak to study the correlation length in ML structures. Also, the interface physical roughness and interfacial diffuseness are distinguished from total interface width by diffuse scattering analysis. The measured rocking scan and fitted profiles are shown in Fig. 5.2. The fitting for MLs with larger N (300 and 400) could not be undertaken owing to the participation of a very large number of structural parameters. It is observed from the best fit results that the physical roughness is less compared to the inter-diffusion gradient at each interface for all the MLs. The best fit results are shown in table 5.2. It is observed that the physical roughness is in sub-angstrom level due to finite size of atoms/molecules. Therefore, the lower value of physical roughness reveals the atomically smooth interface with atomic diffusion in angstrom level. Thus, the results indicate that improved optimized condition is achieved near layer continuous limit in terms of physical roughness for microstructure limited optical performance of W/B₄C ML optics. Furthermore, the measured diffuse scattering results show that both the lateral correlation length and perpendicular correlation length

increases as N increases from 20 to 50. After that both the correlation lengths remains unaltered within errors as N increases. In figure 5.2, the qualitative analysis seems that both the value of perpendicular correlation length and the correlation length at the interface are nearly same after $N=100$. It is here noted that reliable fitted parameters of correlation lengths are obtained by simultaneous fitting of both the measured diffuse scattering and HXR spectra. It is found that the correlation lengths are much smaller and in few nanometres range. It's worth mentioning that the non-coplanar x-ray scattering is more favourable for the estimation of correlation length when the lateral (in-plane) correlation is small \sim few tens of nanometres [166].

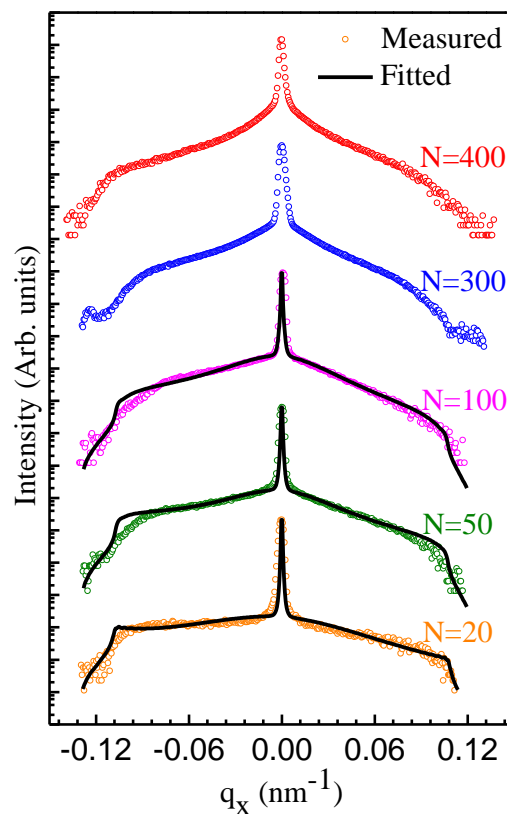


Figure 5.2 Measured diffuse scattering spectra (coloured bubbles) of W/B₄C MLs with varying N = 20-400 at d ~1.9 nm. Solid black lines correspond to the fitted profiles N = 20, 50 and 100.

Table 5.2 Best-fit results of diffuse scattering spectra. σ_r and σ_d represent physical roughness and interfacial diffuseness where as $\xi_{||}$ and ξ_{\perp} represent the lateral correlation length and perpendicular correlation length, respectively.

N	W-layer			B ₄ C-layer			ξ_{\perp} (nm)
	$\xi_{ }$ (nm)	σ_r (nm)	σ_d (nm)	$\xi_{ }$ (nm)	σ_r (nm)	σ_d (nm)	
20	15±3	0.028±0.005	0.25±0.06	4.3±1	0.02±0.009	0.14±0.06	1.4±0.5
50	24±3	0.018±0.003	0.31±0.03	6.6±0.5	0.024±0.004	0.16±0.03	5.6±1.4
100	25±2	0.016±0.003	0.43±0.05	6.7±0.7	0.015±0.005	0.21±0.04	6.8±0.8

5.3.2 Residual stress analysis:

It is well known that the total residual stress is the combination of the stresses of the individual layers and the interface between adjacent layers in the ML stack [69, 167]. In the present work, the total residual stress is studied in MLs, and the residual stress in the nanocrystalline W layer is measured individually to correlate with the total residual stress with varying N from 20 to 400. Therefore, the in-plane total residual stress of the W/B₄C MLs is estimated by using Stoney's equation [94, 95] using substrate curvature method (details of the substrate curvature method is discussed in chapter-2). Due to effect of the residual stress it is observed that the significance change of the surface shape profile before and after deposition. Here, for ML with N=400, the surface shape profiles before and after deposition are shown in the figure 5.3.

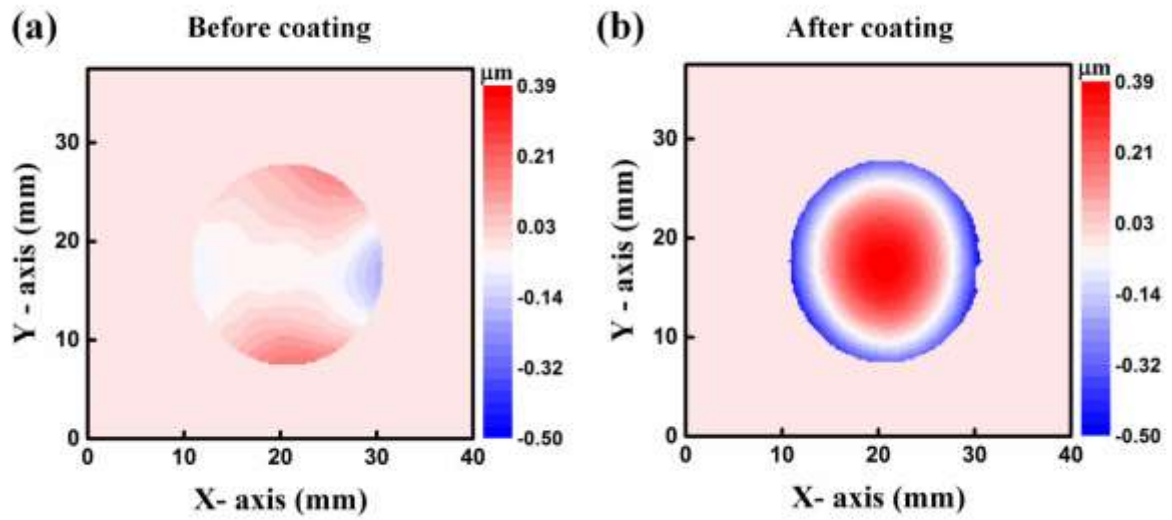


Figure 5.3 2-D surface shape profile of W/B₄C ML having N = 400, (a) before fabrication and (b) after fabrication. The height of the profile is indicated by colour variation.

In figure 5.3, it is clearly observed the significant change in the surface profiles after deposition of the ML which is mainly due to the existence of residual stress in the ML structure. Thereafter, the surface shape profile is fitted to the Zernike polynomial to extract the spherical shape profile and consequently radii of curvature before and after deposition. The variation of the total residual stress in the MLs as a function the N is shown in the figure 5.4.

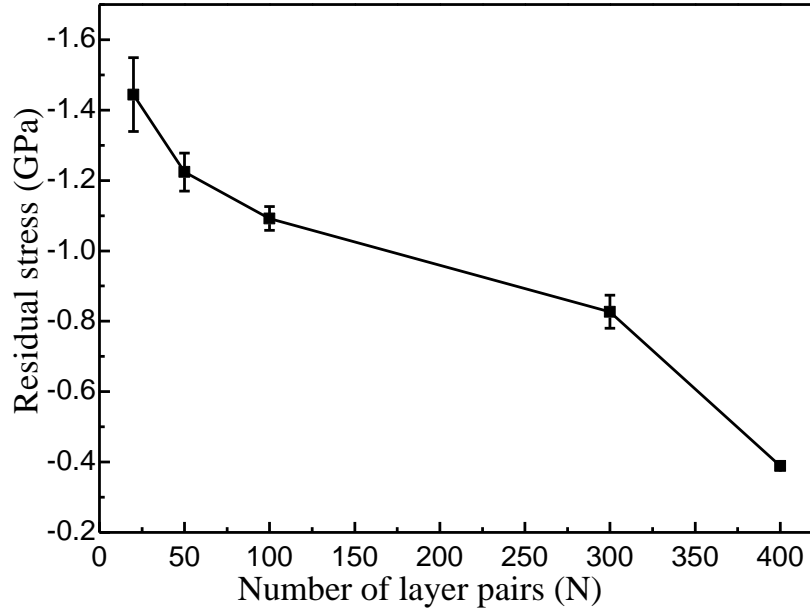


Figure 5.4 Measured total residual stress of W/B₄C MLs as a function of N. The total residual decreases with increasing N and also it is still compressive in nature. The period thicknesses of these MLs are fixed ~ 1.9 nm.

It is observed that the compressive residual stress decreases continuously in non-monotonically as the N increases from 20 to 400. The value of total residual stress varies from -1.444 ± 0.105 GPa (for N = 20) to -0.389 ± 0.009 GPa (for N = 400). It is worth mentioning that Fernandez-Perea *et al.* [168] also have determined total residual stress in three samples of WC/SiC MLs with N = 150 (d = 2 nm), N = 300 (d = 1 nm) and N = 500 (d = 1.5 nm) as a function of thickness ratio Γ . Since the period of their ML samples differs from each other, it is difficult to establish precisely the correlation of their stress variations as a function of N for a particular value of Γ . Nevertheless, the present study shows a similar trend with respect to them for a particular value of Γ except for the sample with N = 300, where d is very small. By comparing the total residual stress for large value of N, they measured total residual stress ~ -0.55 GPa for N = 300 (d = 1 nm and $\Gamma = 0.4$) and ~ -0.2 GPa

for $N = 500$ ($d = 1.5$ nm and $\Gamma = 0.4$). Whereas, in the present thesis work for W/B_4C MLs, total residual stresses are -0.827 ± 0.047 GPa for $N = 300$ and -0.389 ± 0.009 GPa for $N = 400$. The results of the total residual stress in the present study show that the measured stress for ML with large N are in reasonable range for optical device applications e.g. ML optics for soft gamma ray application.

It is also measured the total residual stress of W/B_4C MLs with varying the period (d) thickness from 1.2 nm to 1.97 nm keeping fixed $N=300$. The variation of the residual stress as a function of the period thickness is shown in the figure 5.5. It is observed that the total residual stress is compressive in nature. When the value of d increases from 1.2 nm to 1.56 nm the residual stress slightly increases from -0.176 GPa (± 0.008 GPa) to -0.183 GPa (± 0.008 GPa). But the residual stress significantly increases to -0.827 GPa (± 0.047 GPa) as the periodicity increases to 1.97 nm.

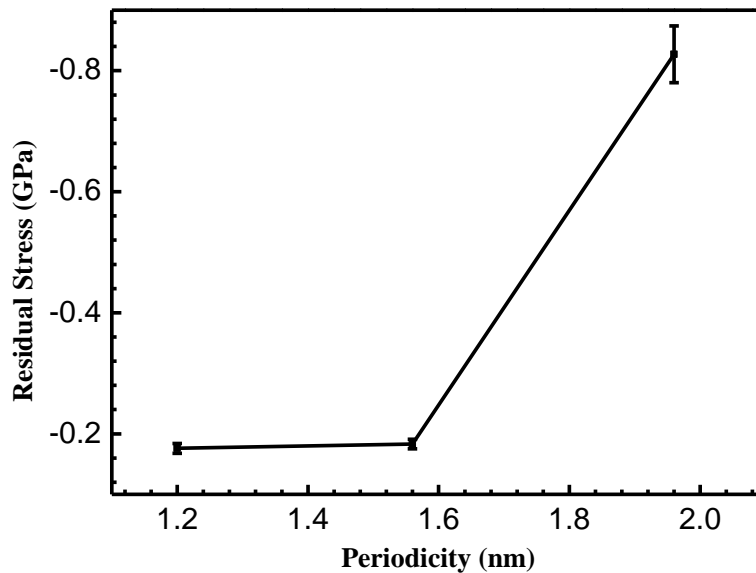


Figure 5.5 Measured residual stress of W/B_4C MLs as a function of periodicity. The periodicity (d) varies from 1.2 nm to 1.97 nm at fixed $N=300$.

Again, the variation of residual stress as a function of N with two different times is shown in the **figure 5.6**. The Black line shows the variation of residual stress as a function of N which is measured within 4 months from sample fabrication. The total stress varies from 1.444 ± 0.105 GPa (for N = 20) to -1.092 ± 0.034 GPa (for N= 100). As N increases from 20 to 100, the compressive residual stress decreases continuously in a non-monotonic manner. Now, the red coloured line shows the measurement of residual stress after two years from first measurement. It is observed that the residual stress is also compressive in nature and the value of the residual stress decreases from first measurement. As N increases from 20 to 100, the total residual stress varies from -0.318 ± 0.016 GPa to -0.911 ± -0.046 GPa.

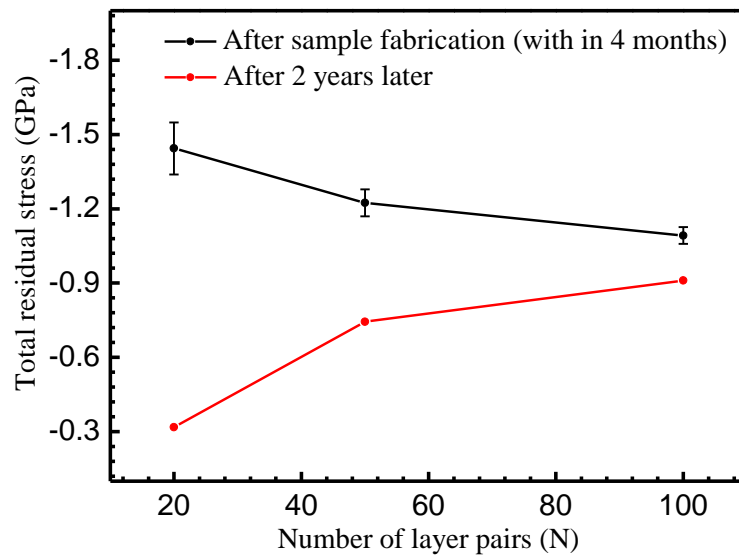


Figure 5.6: The variation of total residual stress as a function N from 20 to 100 having period $d \sim 1.9$ nm with time evolution. Black coloured line shows the measurement within 4 months from sample fabrication. The Red coloured line shows the measurement of residual stress after two years from first measurement.

To understand the evolution of compressive total residual stress and its correlation with stresses originating from layers and interfaces in W/B₄C MLs the GIXRD technique is used to determine the contribution of stresses from layers. Thus, the residual stress is only

measured in the nano-crystalline W layer because the B₄C layers are amorphous structure. The in-plane (biaxial stress) residual stress of W layers in W/B₄C MLs is determined using the GIXRD based $\sin^2\chi$ method. The details of the GIXRD based $\sin^2\chi$ method is discussed in the chapter-2. A typical GIXRD profile of a W/B₄C ML (N=300 at $\chi = 0^\circ$) at energy 15.695 keV is shown in Figure 5.7 (a). The diffraction peaks at $2\theta \approx 19.5^\circ, 34^\circ$ and 43.5° are observed due to W(110), W(211) and W(220) diffraction planes, respectively. The observed 2θ positions of diffraction peaks indicate that predominantly the α -phase is present in the W layers [153]. Indeed, it is difficult to eliminate the possibility of the presence of β -phase due to the broad nature of measured peaks and very close separation of diffraction peaks of α -phase and β -phase localized at $2\theta \sim 19.5^\circ$ and 17.8° . The observed diffraction spectra show that W layers are formed as polycrystalline in nature with average particle size in out-of-plane direction of ~ 0.7 nm obtained using Scherrer formula [101] The average lattice constant is ~ 3.2116 Å in polycrystalline W layers measured by considering the diffraction planes (110), (211), (220) at $\chi = 0^\circ$. It is noteworthy to mention that the measured particle size may be a little overestimated due to contributions of other factors such as defects and stress to the diffraction peaks broadening. For better accuracy, the higher diffraction angle corresponding to W(211) peak was considered for the determination of residual stress. Figure 5.7 (b) resents 2θ versus $\sin^2\chi$ for ML with N=300. The errors in Fig. 5.7 (b) are measured due to uncertainty in determining positions of broad diffraction peaks. The slope, $\frac{\partial(2\theta)}{\partial(\sin^2\chi)}$, is calculated by a linear fitting procedure. Then the residual stress in W layers is determined by using the value of that slope. by the Eq. 2.33 (chapter-2).

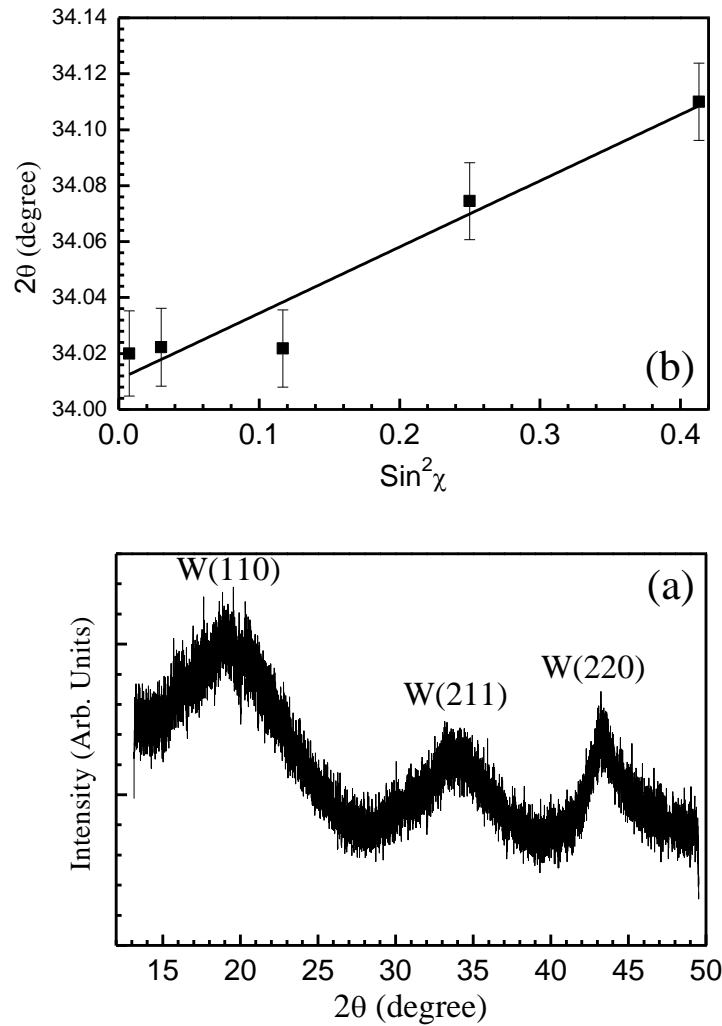


Figure 5.7 (a) Measured GIXRD profile of W/B₄C ML with N=300 at energy 15.695 keV and $\chi=0$. (b) Variation of diffraction peak position (2θ) relating to W(211) with changing $\text{Sin}^2\chi$ for multilayer with N=300.

To determine the residual stress, the θ_0 value used for the bulk W (211) is 17.796° analogous to the energy 15.695 keV [169]. Here, the stresses are measured individually by considering both the elastic constants of bulk and thin film because the elastic constants of thin film are much softened than the bulk values. The thin film [160] (bulk [170]) values used for E_w and ν_w are 338 GPa and 0.395 (411 GPa and 0.28), respectively. Here GIXRD measurements for higher N values (from 50 to 400) were performed at incidence angle 4.5° to confirm penetration of x-rays into all MLs. Also, the higher angle of diffraction peak corresponding to

W (211) plane was considered for stress measurement. However, the incident angle is kept at 0.6° to increase the interaction volume of x-rays in W layers, and lower angle diffraction peak W(110) was taken to enhance the signal to noise ratio for ML with a smaller value of $N=20$ (as well as $N=50$). It is noted that the measurement of residual stress with $N=50$ is performed for both the incident angles (4.5° and 0.6°). The result shows that the value of the residual stresses are within experimental error bar (fig. 5.8). Therefore, the result reveals that the residual stress does not depend on the angle of incidence. The detailed explanations about measurements are given in the experimental section [section 5.2]. The variation of in-plane residual stress of W layers in W/B₄C stack with varying N is shown in Fig. 5.8. The solid line (dashed lines) represents the residual stress in W layers obtained using bulk (thin film) values of the elastic constants, respectively. In figure 5.8, it is observed that the stress in W layers is also compressive in nature. As N increases, the compressive stress decreases. However, the rate of reduction of stress is more for smaller values of N. The decrease of stress is nearly within the experimental errors as N increases from 300 to 400. Considering the thin film values of the elastic constants, the compressive stress is relatively less than that of the bulk elastic constants, e.g., the stress for ML with $N = 400$ decreases by 25%. The stress determination of W layers by considering thin film elastic constants is more appropriated for the present study because the thickness of the individual W layers is ~ 1 nm. Considering the thin film elastic constants, as N increases from 20 to 400, the correspondingly compressive residual stress of the W layers reduces from -5.41 ± 0.54 GPa to -1.2 ± 0.35 GPa.

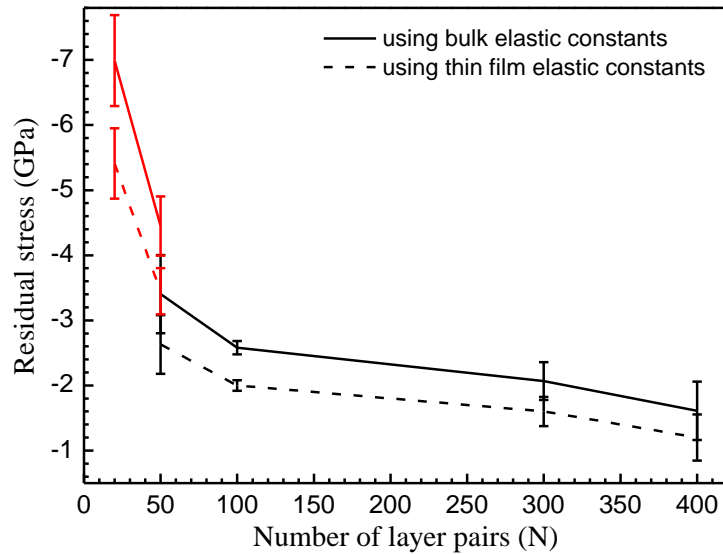


Figure 5.8 Measured residual stress of W layers in W/B₄C MLs with varying N. The solid line and dashed line show that stresses have been determined by two elastic constants values (bulk and thin film). The red lines illustrate the variation of residual stress using W(110) plane at an incidence angle 0.6° whereas the back lines represent the variation of residual stress using W(211) plane at an incidence angle 4.5°.

In order to correlate the total stress in W/B₄C MLs with that in W layers individually, it is clear that both the stresses are compressive in nature. However, the total compressive stress in the MLs is lower than that of the W layers. The higher value of the compressive stress in W layers can be explained by considering both microstructural growths [162] and the atomic peening mechanism that is induced by the impact of the energetic particles on the layers [68, 163]. In all these W/B₄C MLs, the thickness of the W layer is ~ 1 nm which is at near to the limit of continuous layer formation [156]. In support, the TEM measurement also indicates the formation of homogeneous structures with well-defined periodic structures as well as good contrast at interfaces when the W layer thickness is ~ 0.9 nm in W/B₄C ML [171]. Additionally, measured GIXRD profiles on these MLs indicate that W layers are deposited as nano-crystalline structure with out-of-plane average particle size ~0.7 nm. Thus, it ensures

that W layers are nearly continuous structure having many connected small crystalline particles in nanometer scale. These observations indicate that the existing growth conditions of W (deposition rate ~ 8 nm/min and 4.3×10^{-3} mbar) favor the increase of surface density of grain due to the formation of more crystalline nuclei than the previously formed nuclei. Thus, the compressive stress is generated in W layers. Additionally, the lattice constant obtained from the GIXRD data is larger than that of the bulk value and also the measured residual stress in the W layers is compressive in nature. A similar phenomenon is also observed in previously studied sputtered deposited W thin films [161].

The observed phenomenon can be explained by the atomic-peening mechanism [68, 163], where the bombardment of nano-crystalline W layers by the neutral Ar atoms during fabrication gives rise to the compressive stress and the increase in the lattice constants. Earlier, compressive residual stress is also measured in W layers in W/Si ML [153]. The higher value of compressive stress in W layers compared to compressive total stress in ML structure is also observed in other MLs such as W/Cu ML [152].

Previously it is mentioned that the total stress in ML stack is the combination of contributions of stresses from layers and interfaces. Thus, the observed lower value of total stress in W/B₄C MLs compared to W layers is due to compensation by resultant tensile stress arising from B₄C layers and interface stress. The stress of the B₄C layers cannot be estimated individually using GIXRD due to its amorphous nature, so it is difficult to separate the interfacial stress independently. Nevertheless, the measured total stress in ML stack and the stress in W layers clearly point out that the combined stress in B₄C layer and interfacial stress is tensile in nature. For example, it is observed that the total stress is -0.389 GPa and stress in W layers is -1.2 GPa for ML with N =400. Thus, the resultant stress contributed by the B₄C layers and interfacial stress is 0.811 GPa. In the previous study, it has been seen that stress in

B₄C thin film (thickness 50 nm) is compressive and decreases with increasing Ar pressure [172]. Further, stress state in thin film and ML structure also strongly depends on deposition rate [149], film thickness [153], sputtered power [161], and film growth microstructure [162]. In the current study, the B₄C layer thicknesses are very small (~ 0.9 nm), which are deposited at Ar pressure 4.3×10^{-3} mbar with deposition rate ~0.5 nm/min. At this ultra-short layer thickness range, the microstructure of the layers strongly affects the nature of residual stress [160, 162]. In contrast, it is observed that the nature of interfacial stress may be tensile [71] as well as compressive [69, 70, 165] depending upon the thickness of individual layers, material combinations and the formation of interfacial structure at the early stage of layer formation. The interfacial stress in the present study may occur due to interfacial diffuseness and physical roughness at ultra-short thickness limit as observed by using the rocking scan as well as interfacial bonding at interfaces. Therefore, it is expected that the observed difference between the total residual stress and residual stress in W layers is due to the resultant tensile stress arising from the B₄C layers as well as interfaces. The total stress in W/B₄C MLs follows nearly similar fashion as that of stress in W layers with increasing N. The variation of stress with N may be due to stress compensation as more and more interfaces formed [173].

5.4 Conclusion:

In conclusion, the microstructure and residual stress are analysed as a function of number of layer pairs (N) in ultra-short period (~1.9 nm) W/B₄C ML aiming to develop good quality ML mirrors having large N with low residual stress and interface width for application of the soft gamma ray ML optics. The substrate curvature method is used to measure the residual stress of W/B₄C ML whereas the GIXRD based $\sin^2\chi$ method is used to measure the residual stress in W layers. The results show that both the total residual stress and stress in W layers are compressive. The total residual stress in the ML structure is

correlated with stresses in layers and interface stresses. As N increases from 20 to 400 the compressive total residual stress decreases. Finally, ultra-short period W/B₄C ML with large N=400 is developed with low stress and ultra-smooth interfaces using a detailed stress-microstructure correlation analysis. The ML (N=400 and d= ~1.85 nm) is produced with low total stress of ~-0.389 GPa and average rms roughness in the range of ~ 0.275 nm for development of soft gamma rays reflective optics. Also the compressive residual stress has been measured as a function period thickness varying from 1.2 nm to 1.97 nm having fixed N=300.

Chapter-6

Development of W/B₄C multilayer (ML) reflective mirror for potential application in soft gamma-rays:

In this chapter, the development of the ML optics has been described for the application in the soft gamma-ray energy range (100-500 keV). In order to do this, high efficient-metal based W/B₄C ML optics is demonstrated as an excellent material system. The detailed structural parameters and interfacial perfections are probed and determined by using various complementary techniques such as the hard x-ray reflectivity, Transmission electron microscopy (TEM), x-ray diffraction and reciprocal space mapping (RSM). The optical performances are measured in the energy range 10 keV to 20 keV using BL-16, Indus synchrotron. To analyse the optical performance at soft gamma-rays, the reflectivity performance is predicted using extrapolation of known optical properties of materials and using the model derived from hard x-rays reflectivity data.

6.1 Introduction:

Recently, much attention is made towards the exploitation of soft gamma-rays (100 to 600 keV) to advance scientific and technological applications in the emerging frontier areas of nuclear [9, 18] and astrophysics [19, 20, 174]. One of the important issues for exploitation is the development of challenging multilayer (ML) optics, which involves a complex understanding of interfacial phenomena at the sub-nanometer scale. This stipulates the advancement of thin film synthesis technology with higher requirements in the precision and quality control of 1-D periodic ML reflective optics on angstrom level for applications extending towards such high energies. X-ray ML reflective optics works on modified Bragg's principle that provides significantly higher photon flux compared to diffractive optics. X-ray ML allows flexibility to tailor its parameters and to coat on the figured surface for x-ray imaging [4, 22, 175, 176] and focusing [3, 177]. To realize Bragg's reflection of soft gamma rays by a reflective optics, the period thickness of ML must be controlled to the shortest possible desired value with structural perfection at the atomic level. The main obstruction in attaining the ultimate shortest period limit is the formation of a quasi-continuous layer which depends on the material and its growth. In addition, the efficiency of such ML reflective optics depends significantly on (a) optical contrast, (b) interface perfection, (c) residual stress and (d) period uniformity in ML stack. Any deviations of these parameters from the desired values affect the optical properties which significantly impact the functionality of the device. For example, a catastrophic drop of reflectance as film thickness approaches beyond the continuous limit [9, 10] and instability of ML film over time due to high residual stress [26]. All of these, in turn, require a technological challenge to produce such ML optics with high efficiency. This demands to search for a suitable material system to grow the structure having a few hundreds of layer pairs (N) with period thickness $d \sim 1\text{-}2$ nm and to understand the

evolution of microstructure and interfacial phenomena to achieve atomic smooth interfaces, low residual stress and the tolerable thickness uniformity concurrently.

Taking into account these aspects, here, B₄C is considered as one of the prospective low-Z material for such mirror because B₄C is known to grow in 2D carpet-like manner, chemically stable, amorphous structure and form smooth surface [154]. W is considered as high-Z material because it has the ability to form a stable and sharp interface with B₄C layer [156, 178] and provides a high reflection coefficient. All of these, in turn, indicating W/B₄C could be a potential material system for the soft gamma-ray mirror, if the synthesis process could be judiciously engineered for higher structural requirements of such optics. Previously, W/B₄C system with different designing parameters has been studied for x-ray regions. For example, the minimum reported interface width was $\sigma=0.292$ nm for a commercial W/B₄C ML mirror (N=350, d=1.743 nm and $\gamma=0.382$) for soft x-ray polarization analysis [179]. Although, further shorter period W/B₄C MLs (d ~0.7-1.2 nm) are studied by Windt *et al.*[180] (with $\sigma = 0.29$ nm and N = 300) and thereafter by Bibishkin *et al.* [181] (with $\sigma =0.24$ nm and N =500-800) to provide high resolution in the soft x-ray region, but the designed thicknesses of the W layer are in the range of 0.147-0.252 nm, which are in discontinuous region because W layer continuity begins to be lost at its thickness of ~ 1 nm [182]. The discontinuous layers lead to low optical contrast, and unsuitable to provide high photon flux. In addition, none of the aforementioned earlier studies address one of the critical parameters, i.e., level of the intrinsic residual stress in the ML stack. A variety of material systems are currently being developed for prospective reflective ML optics for high energies, e.g., energy up to 200 keV [26, 87, 183, 184]. For further higher energies up to 600 keV, a metal compound based ML optics such as WC/SiC system has been demonstrated [9, 18 185, 186]. Considering metal carbide as the material of choice facilitates to obtain interfaces with a better smoothing due to the amorphous structure as compared to its bare metal

counterpart due to polycrystalline structure [187], but at a cost of lowering of optical contrast, for e.g., 22.8 % decrease of ideal density contrast in WC/SiC as compared to W/SiC. As the optical contrast decreases the integrated Bragg peak intensities (proportional to photon flux) decrease due to the contribution of a larger number of interfaces to the total reflection coefficient.

Here, we demonstrate efficient metal-based multilayered soft gamma-ray optics by precisely controlling microstructure at ultrathin limit near the onset of formation of the continuous layer to tailor interface width comparable with metal carbide system to make use of a bonus of the unique advantage of high optical contrast of the former to offer higher photon flux. The former parameter is achieved by a combination of engineering surface density of grains to form more crystalline nuclei rather than growth of previously formed nuclei by tailoring rate of impingement of metal ad-atoms and controlling the kinetics of ad-atoms for the required surface mobility. Considering these facts into account, we produce metal-based (W/B₄C) ML optics concurrently having an achievable average interface width as well as residual stress comparable with metal carbide-based ML counterpart [1, 187]. We report an achievable interface width (e.g., $\sigma \sim 0.27$ nm for ML with $d = 1.86$ nm and) along with a low compressive residual stress of 400 MPa as well as a period non-uniformity ~ 2.5 % over a length scale of ~ 130 nm size. This facilitates an added advantage due to its superior optical property as a candidate of choice for a highly efficient reflective optics required for soft gamma-ray spectroscopy. Measured optical properties in energy range 10 to 20 keV agree well with those predicted by the simulation. Structure-stress-optical properties are correlated considering the mechanism of film growth near the layer continuous limit. The expected optical performances are predicted in the soft gamma-ray region considering the model obtained from hard x-ray data and discussed.

6.2 Experimental details:

W/B₄C ML samples having periodicity $d = 1.86- 1.23$ nm and fixed number of layer pairs, $N=400$ are fabricated by magnetron sputtering system [76]. More details of the magnetron sputtering system are described in the chapter-2. The ML samples are fabricated on super polished oxidized silicon wafers (100) substrates (rms roughness in the range~0.3-0.4 nm) of size ~30 mm×20 mm. The substrates were ultrasonically cleaned in acetone prior to ML fabrication. Before the fabrication of final MLs the out-gassing from the inner surfaces in the fabrication chamber was optimized by proper conditioning and the microstructure of the layers and interfacial perfections are precisely engineered by adjusting and controlling the process parameters in a systematic way. The period of the MLs is varied by changing the thickness of B₄C at a fixed thickness of W at ~0.94 nm which is a lower limit for the formation of continuous layer. More details are discussed in chapter -2 (section 2.4). The hard x-ray reflectivity performance is carried out using BL-16 of Indus-2 synchrotron [188]. The incident flux is measured using miniature ionization chamber (micro-IC). The reflected intensities are measured using a Avalanche Photo Diode (APD) detector with the angular step size of 0.005° in s-polarized geometry. The optical performances are determined in the energy range 10-20 keV. The hard x-ray reflectivity data are fitted by using ‘IMD’ coded ‘XOP’ software package [33] and the algorithm of the software is based on recursive methods of Fresnel equation [35]. In order to calculate the reflectivity for soft gamma-ray at 300 keV, 378 keV and 384 keV, the optical constants are derived by considering the atomic scattering factors of elements [189, 190] and weighted average of bulk density of materials for compounds. The bulk densities of W, WC, Si, SiC, and B₄C are taken as 19.3 g/cm³, 15.63 g/cm³, 2.33 g/cm³, 3.21 g/cm³, and 2.52 g/cm³, respectively [28]. The reflectivities for the different material systems are calculated by using IMD software. The RSM (reciprocal space mapping) measurements are performed by omega scans for different 2θ values (step size 0.02

deg) around the Bragg peaks. Brucker D8 discover x-ray diffractometer is used for these RSM measurements at incident energy 8.047 keV (Cu K_{α}). The slit sizes are 0.05 mm and 0.2 mm at incident beam and detector, respectively. To calculate the crystallite size in the W layers the grazing incidence x-ray diffraction (GIXRD) measurements are done by angle dispersive x-ray diffraction beamline (BL-12) at Indus-2 synchrotron source [103]. The GIXRD measurements with in-plane and out-plane are performed at energy ~ 17.295 keV using a MAR345 image plate area detector. The standard NIST LaB_6 sample is used to calibrate the incident energy. The incident angle of the beam on the sample was fixed at $\sim 3^\circ$. The measured GIXRD profile of W (110) diffraction peak are fitted using the asymmetric double sigmoidal function. The cross-sectional TEM analysis of MLs with $d=1.55$ nm and 1.23 nm were studied using a Philips CM 200 transmission electron microscope, operated at 200 keV. The details are described in the chapter-2 (section 2.5.7). The layer thickness of the MLs is measured from TEM measurement using GATAN Micrograph software. The total residual stress in W/ B_4C ML was determined by measuring the radius of curvature of the substrate before and after deposition of ML film using substrate curvature method in a Zygo Mark-II laser Fizeau interferometer setup using Stoney's equation [94, 95]. The details of residual stress are described in the chapter-2.

6.3 Results and discussion:

6.3.1 Understanding of material system for soft gamma-rays reflective optics:

In the soft gamma-ray spectrometer, the challenges are higher requirements of efficient optics to deliver a sufficient amount of photon flux to improve signal-to-noise ratio because of the weak signal strength of emitted gamma-rays from distance stellar objects as well as remnant radioactive isotopes in nuclear spent-fuel. It requires an optically suitable better material system for ML mirror which enables to provide both high peak reflectance as well as high integrated reflectance (area under the Bragg peak). For optical consideration,

only four selected material systems for MLs are chosen (W- and WC-based) taking into account their ability to form a low interfacial imperfection at ultra-short period, which is required for such a high energy application. It is noted that according to classical wave physics, it was demonstrated earlier that ML optics works efficiently for such high energy and incoherent scattering does not affect the intensities at Bragg angle [9]. Thus, the position and amplitude of the Bragg peak can be calculated theoretically in the soft gamma-ray region using the wave model [33]. The Fig. 6.1 (a) demonstrates a comparative calculated first order peak reflectivity of four different ML systems as a function of interface width at 300 keV. Whereas, Fig. 6.1 (b) demonstrates peak reflectivity versus N for four ideal ML mirrors to understand about the role of optical contrast for high photon flux. For these calculations, the structural parameters of MLs are $d = 1.86$ nm, $N = 400$ and the ratio of the thickness of high-Z layer to period thickness $\Gamma = 0.505$ are kept fixed. In Fig. 6.1 (a), the vertical dotted line represents the value of interface width (0.275 nm) of WC/SiC soft gamma-ray ML optics reported in the literature [9] and for the vertical dashed line represents the interfacial width 0.27 nm of W/B₄C ML in the present study. The positions of arrows indicate the corresponding calculated reflectivities of WC/SiC ML and W/B₄C ML at the marked interface width. At the marked interface widths, the reflectivities of WC/SiC, WC/B₄C, W/B₄C and W/Si are nearly same (within 1%). However, in Fig. 6.1 (b), the saturated peak reflectivity (marked by arrows) is material dependent. The ideal density contrast of WC/SiC, WC/B₄C, W/B₄C and W/Si are 12.42 g/cm³, 13.11 g/cm³, 16.78 g/cm³ and 16.97 g/cm³, respectively [28]. Thus, ideally ~35 % more density contrast in W/B₄C with respect to WC/SiC system. It is clear that the higher is the density contrast the lower is the saturated N values. The calculated ideal reflectivities are saturated at $N \sim 190$ for W/B₄C ML and at $N \sim 250$ for WC/SiC ML. The lower saturated N values indicating the smaller numbers of interfaces contribute to the total reflection. Thus, W/B₄C and W/Si MLs have higher

integrated reflectance and hence higher photon flux compared to WC/SiC and WC/B₄C. By comparing W/B₄C with W/Si system, although the ideal optical performance of W/Si is nearly similar to W/B₄C ML system, but generally achievable interfacial perfection in W/B₄C is better than in W/Si ML system because of diffusion and/or reactivity of Si with metal at interfaces [191-193]. Thus, in soft gamma-ray region, W/B₄C material system turns out to provide higher integrated reflectance than its compound counterpart (WC) because of superior optical contrast in combination with low interface width.

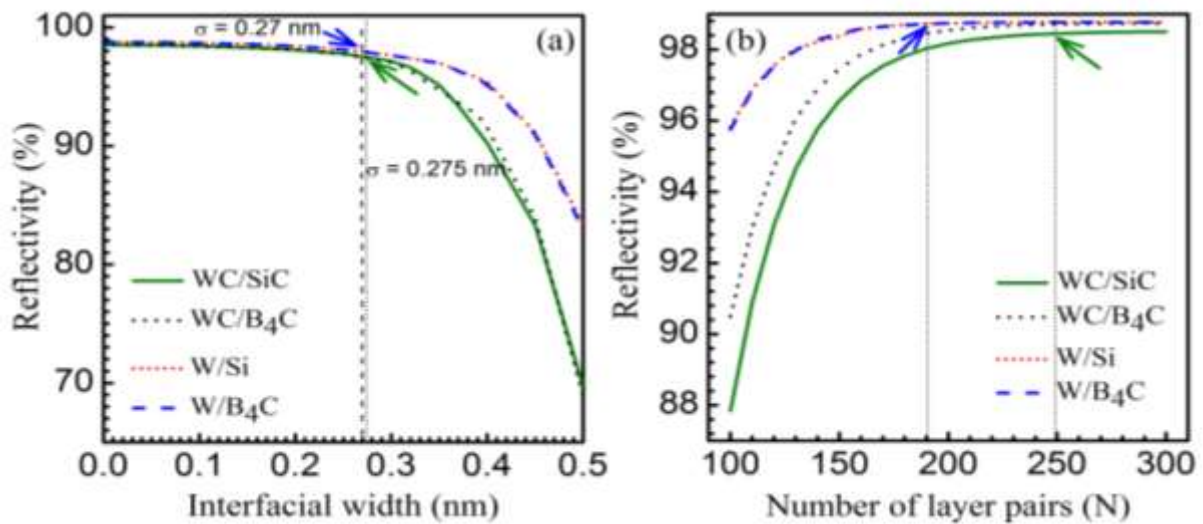


Figure 6.1 The reflectivity performances of four different ML systems (WC/SiC, WC/B₄C, W/Si and W/B₄C) are calculated by considering ideal mass densities at the energy 300 keV. Both the step size and instrumental angular resolution ($\Delta\theta$) are kept fixed at 0.0001° for that calculation. (a) Peak reflectivity of the 1st order Bragg peak as a function of interface width (σ). The calculations are performed for MLs with $d = 1.86$ nm, $N = 400$, and Γ ratio = 0.505. The dotted line represents the interfacial width (σ) = 0.275 nm of earlier reported soft gamma ray WC/SiC ML optics [9] and the dashed line indicates the $\sigma = 0.27$ nm for W/B₄C ML optics in the current work. The corresponding calculated reflectivities at the above specified interfacial width are indicated by the positions of the blue and olive colored arrows. (b) The

1st order Bragg peak reflectivity with varying N represents the material dependent of saturated peak reflectivity (indicated by arrows).

6.3.2 Analysis of microstructure:

The microstructural parameters of the MLs (ML-1, $d=1.86$ nm; ML-2, $d=1.55$ nm and ML-3, $d=1.23$ nm) are obtained more precisely by fitting the measured hard x-ray reflectivity (HXR) curves up to 6 degrees (Fig. 6.2). The measured HXR data are fitted by considering the modified Fresnel co-efficient formalism with assuming an error-function interface profile. The measured HXR spectra show well defined higher order Bragg peaks revealing good quality of periodic structure in the ML stacks even though periods are very small. Presence of shallow humps between the critical angle and first order Bragg peak indicating slightly modulations of the electron densities at the top of MLs. This happens due to contamination of the top layer when the MLs were exposed to ambient condition. The best fit results show that the thicknesses of contaminated top layer are 7, 3 and 2.5 nm for ML-1, ML-2 and ML-3, respectively. It is noted that the value of N is very large (400) in the present study. So, if each layer will be considered independently, then the number of fitted parameters will be very large. To avoid this difficulty, the thickness, interface width and density of each type of material are kept fixed in each period in ML stack during fitting of the measured data. The data are fitted by considering a random thickness error in ML to account for slight variation of deposition rate during deposition and shown in Fig. 6.2. The best fit results reveal a small random thickness error of ~ 0.012 nm in ML mirrors. We considered the instrumental angular resolution of 0.001° . To consider the incident photon energy band width (± 1 eV), reflectivity profiles are fitted at different discrete energy band of interval 1 eV and then averaged over the energy band width. The fitted profiles well match with the measured curves including peak intensities to interpret the structural parameters of the ML mirrors. For ML with $d = 1.86$ nm, the fitted profile is noticeable deviate from the measured data at the width of higher

order Bragg peaks. This is due to the broadening of the measured Bragg peaks arising from variations of interfacial widths at each interface and period non-uniformity, which are not included in the model. In MLs, the thickness of the W layer was kept fixed at ≈ 0.94 nm, while the thickness of the B₄C layer was decreased from 0.92 nm (ML-1) to 0.33 nm (ML-3). The thickness of the W layer was kept fixed intentionally at ≈ 0.94 nm to ensure that it provides a good optical contrast at near its lowest thickness limit for formation of the continuous layer [156]. The best fit results are given in Table 6.1. The densities of the W layers in both ML-1 and ML-2 are nearly the same ≈ 16.8 g/cm³. In case of ML-3, the W layer density decreases to ≈ 16.0 g/cm³ due to a small decrease of the W layer thickness (≈ 0.9 nm). Therefore, it is observed that the mass density of the layer is affected by a slight decrease of layer thickness near the layer continuous limit. The observed lower values of densities of the W layers in MLs than its bulk value (19.3 g/cm³) are due to the loosely packed W layers and embedded of some B₄C molecules into loosely packed W layers. Similarly, the density of the B₄C layer increases monotonically from 3.2 g/cm³ to 9.5 g/cm³ due to embedded of more and more W atoms into B₄C layers while the thickness of the B₄C layer decreases from 0.92 nm (ML-1) to 0.33 nm (ML-3). It is noted here that densities of B₄C layers are more than its bulk value (2.52 g/cm³) due to embedded of heavy W atoms in B₄C layers. There is a sudden significantly increase of density of B₄C layers (~ 156 %) from ML-2 to ML-3. This is because as B₄C thickness is decreased to 0.33 nm (ML-3), it form quasi-continuous layer. It is also clearly observed using TEM measurement that W atoms get embedded into B₄C layer.

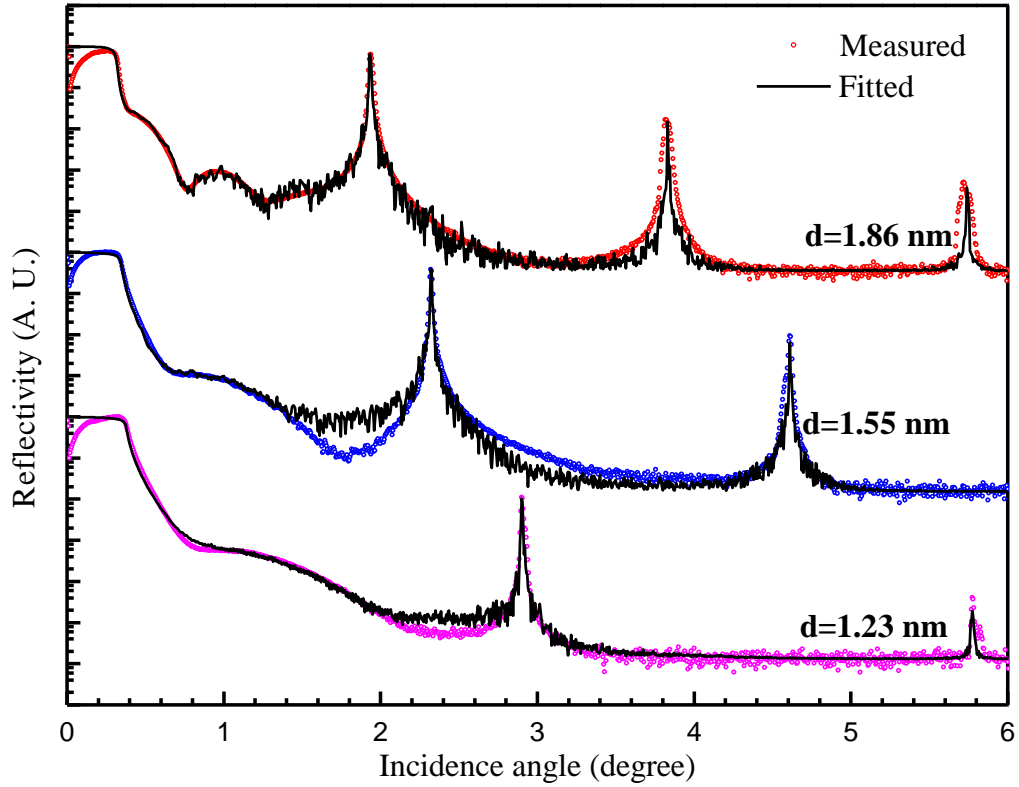


Figure 6.2 Measured and fitted HXR spectra at energy 10 keV of three W/B₄C MLs with varying periods $d = 1.86$ nm (ML-1), 1.55 nm (ML-2) and 1.23 nm (ML-3) at a fixed $N = 400$ with considering random thickness error ~ 0.012 nm, instrumental angular resolution 0.001° . Also, measured reflectivity spectra are fitted at energy band (± 1 eV) with interval 1 eV and then averaged over the energy band width.

Table 6.1. Best fit HXR results of W/B₄C MLs at energy 10 keV. d , t , σ and ρ are period, thickness of layer, interface width and mass density of layer, respectively.

Sample No.	d (nm)	W layer		B ₄ C layer	
		t / σ (nm)	ρ (g/cm ³)	t / σ (nm)	ρ (g/cm ³)
ML-1	$1.86(\pm 0.01)$	$0.94/0.33 (\pm 0.03)$	$16.8(\pm 0.5)$	$0.92/0.21(\pm 0.02)$	$3.2(\pm 0.3)$
ML-2	$1.55(\pm 0.01)$	$0.99/0.37(\pm 0.02)$	$16.8(\pm 0.5)$	$0.56/0.2(\pm 0.02)$	$3.7(\pm 0.3)$
ML-3	$1.23(\pm 0.01)$	$0.9/0.43(\pm 0.03)$	$16.0(\pm 0.5)$	$0.33/0.21(\pm 0.02)$	$9.5(\pm 0.6)$

The observed density contrast between W and B₄C layers was optimized by tailoring with the kinetics of ad-atoms/molecules by considering simultaneously interface widths and residual stress in ML stack. It is observed that the density contrast ($\rho_W - \rho_{B_4C}$) is 13.6 g/cm³ and 13.1 g/cm³ for MLs with d = 1.86 nm (ML-1) and 1.55 nm (ML-2), respectively. Here it is mentioned that previously for WC/SiC based soft gamma-ray mirror [9], density contrast taken as 12.82 g/cm³, which was estimated by considering bulk density for the WC layer (15.8 g/cm³) and used density of a reasonable higher thickness film for the SiC layer (2.98 g/cm³). In general, the actual layer density in the ML stack is lower than bulk value at an ultra-short layer thickness. This indicates that W/B₄C multilayer is an optically superior material combination with high density contrast compared to WC/SiC. Thus, it is anticipated that W/B₄C reflective mirror would provide a relatively higher photon flux in soft gamma-ray region than WC/SiC ML mirror, if interface widths could be engineered to an achievable level as compared with that of WC/SiC. Regarding interface widths, for ML with d = 1.86 nm (ML-1), interface width of W and B₄C layers are 0.33 nm and 0.21 nm, respectively. As period thickness decreases to 1.55 nm (ML-2), interface width of W increases to 0.37 nm whereas that of B₄C decreases to 0.2 nm. As the period further decreases to 1.23 nm, interface widths of W and B₄C layers increase to 0.43 nm and 0.21 nm, respectively. As the period decreases, roughness as well as interfacial diffuseness increases especially for W layers that lead an increase in length of the gradient of electron density at interfaces. The analyses of rocking scan measurements indicate that the component of diffuseness to interface width is more (~angstrom level) than physical roughness (~sub angstrom level) along with small (few nanometers) correlation lengths in the ML structures (discussed in the previous chapter chapters 4, 5). It is observed that the average interface widths of W and B₄C layers in MLs (ML-1 and ML-2) are 0.27 nm and 0.285 nm which are comparable to the earlier reported value of 0.275 nm for WC/SiC based soft gamma ray optics with N=300 and

$d = 1.474$ nm [9]. The bonus in the present case is that the superior achievable optical contrast in W/B₄C than WC/SiC to obtain high photon flux required for gamma-ray spectroscopy applications. As the period of ML decreases to 1.23 nm (ML-3), the average interface width increases significantly to 0.32 nm as well as density contrast decreases drastically to 6.5 g/cc due to quasi-continuous nature of B₄C layers. The quasi-continuous nature of B₄C layer is experimentally observed using high-resolution TEM. This is the microstructure limitation arising from film growth in Volmer-Weber growth mode. A similar microstructure limitation due to quasi-continuous nature of layers is observed earlier in case of WC/SiC ML [9].

For more detailed justification of microstructure of the layer structure in the MLs, the observed results of the HXR are well correlated to the RSM (reciprocal space map), TEM and GIXRD both in direction of in-plane and out-plane as follows. The RSM spectra (in terms of momentum vector q_x and q_z) around the Bragg peaks for ML-1 (Figs. 6.3(a-d)), ML-2 (Figs. 6.3 (e and f)) and ML-3 (Figs. 6.3 (g and h)) reveal that the scattered intensities from the MLs concentrate in intensity strip of Bragg sheets, centered at $q_z = \frac{2\pi n}{d}$, where $q_z = \frac{4\pi \sin\theta}{\lambda}$ and n is order of Bragg peak. The measured RSM profiles of the Bragg sheets evidence periodic ML structure and provide information on correlation of interfacial roughness profiles in MLs qualitatively. It noted that the Bragg diffuse scattering is not visible due to very low intensity in ML-3. The calculated periodicity for the ML-1, ML-2 and ML-3 from RSM measurement using the separation between two successive observed Bragg sheets are 1.89 nm, 1.53 nm and 1.23 nm, respectively. The results indicate that the periodicity well matches with the HXR results. The multilayer peaks are extended towards q_x (lateral direction) due to resonant diffuse scattering originated by the interference of the waves scattered from the partially correlated interfaces of the multilayer [85, 194]. Since width of the profiles along q_x does not change with n , one can conclude that the interface profile is same for all interfaces.

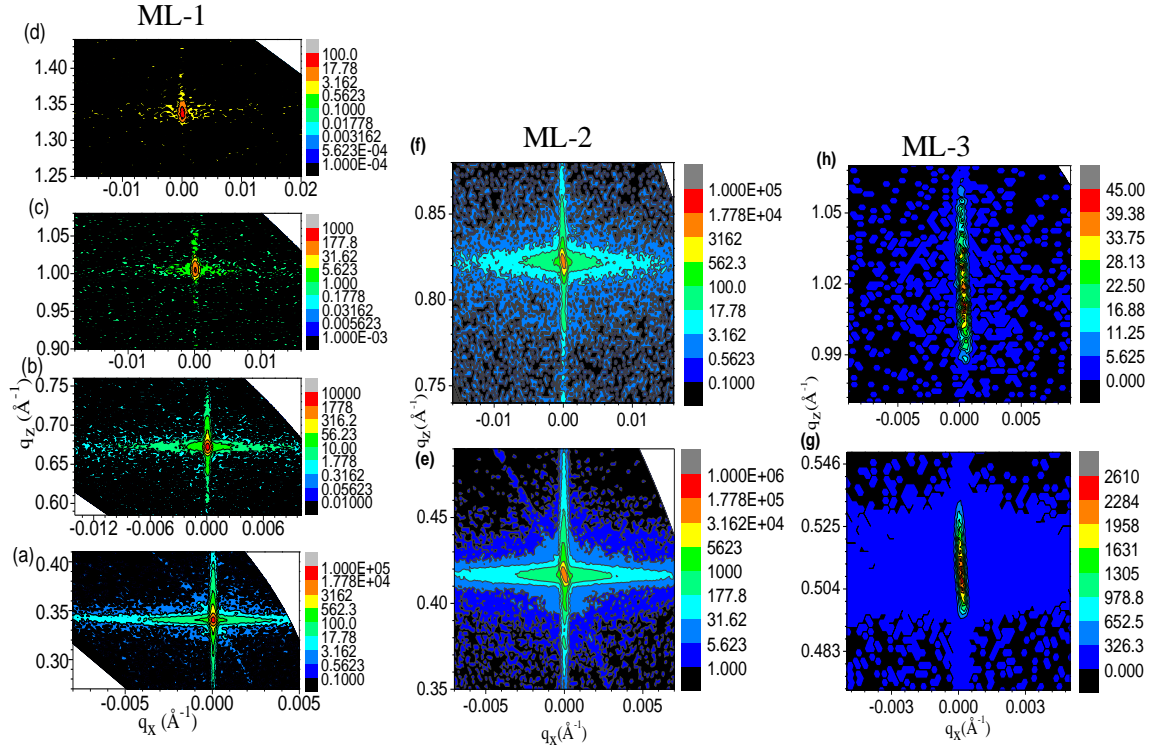


Figure 6.3 The RSM Measured data of three W/B₄C MLs at energy 8.047 keV. The figures in left panel (a-d) are of ML-1, the figures in the middle (e and f) are of ML-2 and the figures in right panel (g and h) are of ML-3. In left panel: (a) 1st order Bragg peak, (b) 2nd order, (c) 3rd order and (d) 4th order. In the middle: (e) 1st order Bragg peak and (f) 2nd order peak. In right panel: (g) 1st order Bragg peak, and (h) 2nd order peak.

It is noted that the two main parameters such as interface width and density contrast decide the optical efficiency of ML mirrors for soft gamma-ray region. Thus, comparing measured achievable values of interface width and density contrast, it is predicted that ML-1 and ML-2 in the current study would afford a better integrated reflectivity in the soft gamma-ray energy region. However, the structural perfection shows that ML-3 is not suitable for the soft gamma-rays energy range due to comparable high interface widths and decrease in optical contrast. The observed HXR results are correlated with high resolution cross-sectional TEM to understand more detailed microstructure in the layers of MLs (ML-2 and ML-3) which is presented as follows.

A well-defined layer structure with good density contrast is clearly observed in ML with $d = 1.55$ nm (ML-2) using high resolution cross-sectional TEM image (Fig. 6.4 (a)), revealing near perfect periodicity is maintained throughout the ML stack. However, the optical contrast is significantly deteriorated as period decreases to 1.23 nm for ML-3 which is clearly shown in Fig. 6.4 (b). The line profiles of these MLs (ML-2 and ML-3) are also shown in the figures 6.4 (c and d). In case of ML-3, as thickness of the B_4C layer decreases to 0.33 nm, quasi-continuous nature of B_4C is clearly observed, where W atoms are embedded in the discontinuous region of the B_4C layer. This result emphasizes that the density of B_4C layer increases significantly to ~ 3.77 time of its bulk value as observed by HXR. The average period measured from TEM image for ML-2 and ML-3 are $d = 1.48$ nm and $d = 1.23$ nm, respectively. Thus, observation of the TEM image correlate well with HXR results on the structure of MLs.

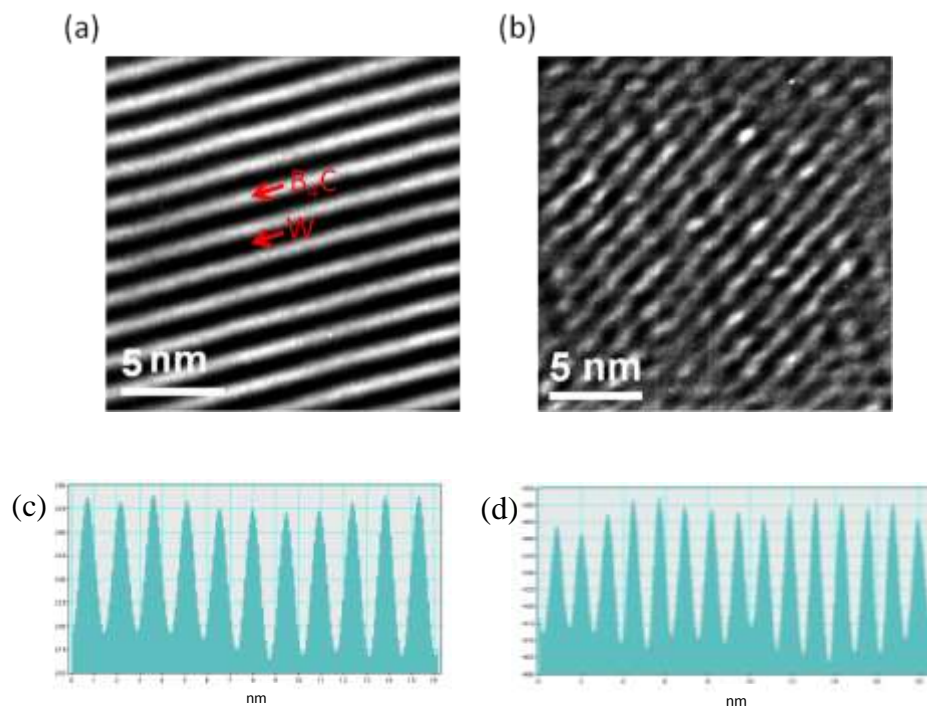


Figure 6.4 High resolution cross-sectional TEM images of W/ B_4C MLs with $N = 400$. (a) ML-2 with $d = 1.55$ nm. (b) ML-3 with $d = 1.23$ nm. (c) line profile of the ML-2. (d) line profile of the ML-3.

For better understanding of the observed achievable interface width for MLs, GIXRD measurements are performed in both in-plane and out-of-plane orientations. To correlate achievable interface width with the structure of layers at early stage of film growth, the crystallinities in W layers are quantitatively analyzed. The high intensity W (110) peak was considered for the analysis. The GIXRD pattern for these MLs is shown in the figure 6.5. The measured peak position, FWHM and crystallite size are tabulated in table 6.2. It is noted that the position of W (110) of stress free bulk W is $2\theta = 18.44^\circ$ at energy 17.295 keV [169]. The observed peak positions are lower than the stress free bulk W (110) value ($2\theta = 18.44^\circ$ at energy 17.295 keV). Further, in-plane FWHM is smaller than out-of-plane. The average crystallite (particle) size L is obtained from broadening of the diffraction peak using the Scherrer equation [101] $L = 0.9\lambda/(\Delta(2\theta) \cos\theta_B)$, where λ is the wavelength, θ_B is the Bragg angle and $\Delta(2\theta)$ is the line broadening at half the maximum intensity. In table 6.2, the average crystallite in the out-of-plane orientation is smaller than the thickness of W layer. The crystallite size in both in-plane and out-of the plane are in sub-nanometer length scale (0.50-0.67 nm). Again, relatively larger crystallite size in in-plane direction than out-of-plane represents dominating nature of the lateral growth of W particles at the early stage of film growth. Similarly, GXRD results show that B₄C is amorphous in nature. The observed smaller interface width of B₄C than W (Table 6.1) is because of amorphous structure in B₄C layer.

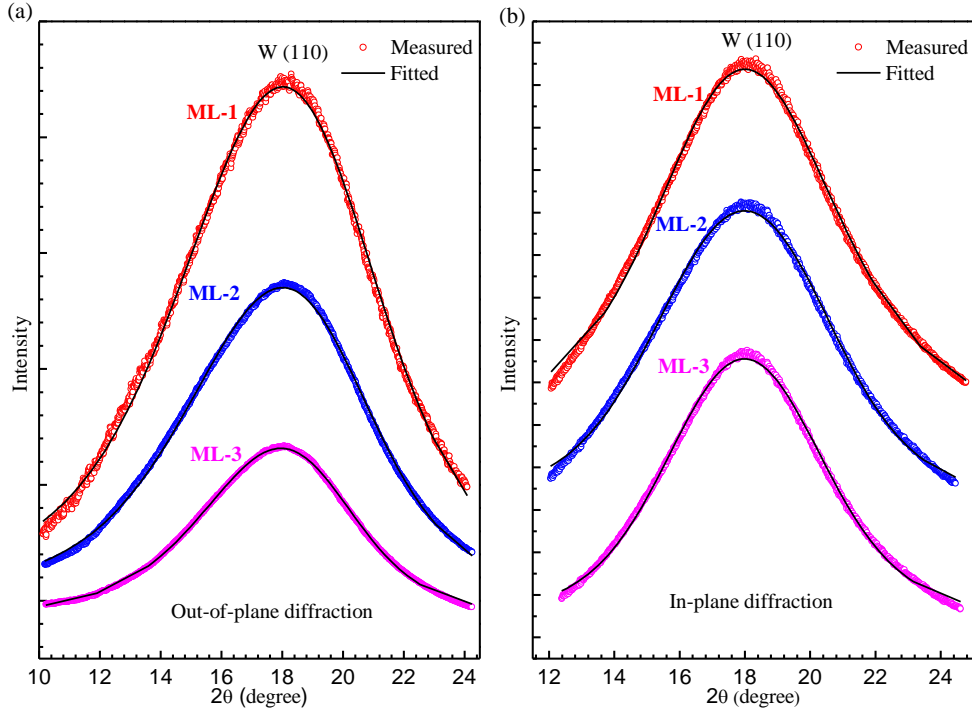


Figure 6.5 Measured and fitted GIXRD profiles of W (110) diffraction of ML-1, ML-2 and ML-3 at energy 17.295 keV. (a) Out-of plane diffraction (b) In-plane diffraction with data taken at an angle 18° above the sample surface.

Table 6.2. The best fit GIXRD results of W (110) diffraction peak along with average size of crystallite (particle).

Sample No.	Out-of-plane			In-plane		
	peak position (2θ°)	FWHM (°)	particle size (nm)	peak position (2θ°)	FWHM (°)	particle size (nm)
ML-1	18.06	7.54	0.50	18.07	6.40	0.58
ML-2	18.10	6.98	0.54	18.07	6.20	0.60
ML-3	17.98	5.84	0.64	18.07	5.61	0.67

The observed achievable structure of ML optics with required residual stresses (discussed in section 6.3.3) are obtained by precisely engineering surface density of grains and kinetics of ad-atoms. At the optimized process parameters, W layers creates more surface density of grains by decreasing mean size of grains to the order of sub-nanometer level (confirmed by

GIXRD) and relatively compact (corroborated from measured density using HXR) near the continuous limit of layer thickness. The observed microstructure of the layer indicates that the structural growth favors the formation of many crystalline nuclei rather than growth of previously formed nuclei at nucleation/island growth structure. Surprisingly, the crystallite size in the sub-nanometer level in both the directions supports that the microstructure of W layers form very fine crystallites, as if tending towards amorphous structure. Consequently, the average achievable interface width is obtained of 0.27 nm (ML-1) which is required for such high energy optics. Figure 6.6 shows a correlation between the morphology and surface density of grains schematically.

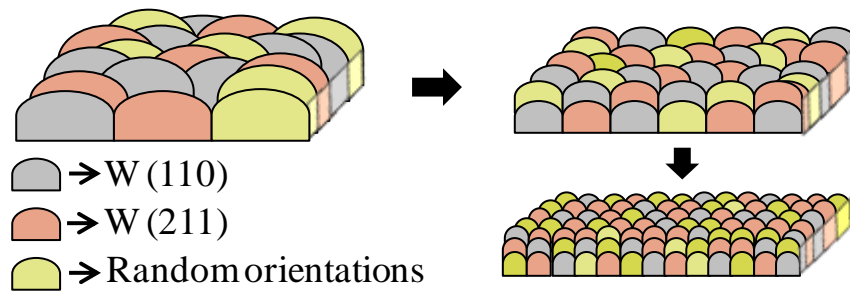


Figure 6.6 Schematic of morphology of W layer near the layer continuous limit representing correlation between roughness and surface density of grains. As surface density of grains increases gradually (indicated by arrows), the morphology tends toward more compact and smoother. The color code represents the different orientations of crystallites (particles).

6.3.3 Residual stress and period uniformity:

For long term stability, the study of the residual stress is another important factor in such ML mirrors with large values of N . The total residual stress of the ML stack is measured with varying N at fixed periodicity ~ 1.9 nm as shown in chapter 5 (Figure 5.4). The nature of the total residual stress is compressive. The total residual stress decreases as the N is increases. The total residual stress is ~ -389 MPa for the ML with $N = 400$. It is also observed that the measured residual stress decreases with decreasing periodicity at a fixed number of layer

pairs $N=300$, as shown in chapter 5 (figure 5.5). In multilayer structure, the total residual stress depends on both microstructure of layers and nature of interfaces between the adjacent layers especially important while thickness is near the onset of formation of the continuous layer. It is observed that the crystallites of W layers are small corresponding to the compressive residual stress. The detailed analyses of stress-structure correlation with the contribution of stress from only W layers in MLs are discussed in chapter 5. In the present work, the measured values of total residual stress in W/B₄C MLs with $N = 400$ is comparable with that of earlier reported for WC/SiC based soft gamma-ray ML reflective optics [168].

Similarly, ML mirrors to be operated at extremely small glancing incidence angles of a few to several milli-radians, the period non-uniformity was controlled to 2.5 % over 130 mm length by placing small size substrates at the different positions along the length. Three samples were placed at the centre (MS1), 20 mm away from the centre (MS2) and 130 mm from the centre (MS3). The measured HXR profile of three MLs with a fixed $N= 300$ at three different position over 130 mm is shown in the figure 6.7. It is observed that the periodicity decreases slightly from centre of the substrate holder to the end of the one side. This is because of the spatial variation of deposition rate across the large cathode of length 500 mm. It is assumed that the plasma concentration is higher at the center of the cathode and symmetrically reduces towards the both ends of the cathode in magnetron sputtering system. So, proper masking arrangement in front of cathode would certainly reduce the difference of the spatial variation of the distribution of sputtered atoms coming from the center and from the both ends of cathode through the tapered mask. This would further improve the uniformity over larger length of mirror. Thus, experimental observations indicate that low interfacial widths, low residual stress as well as tolerable period uniformity are concurrently obtained in an optically superior material system suitable to achieve a better optical performance which has been discussed in the next section.

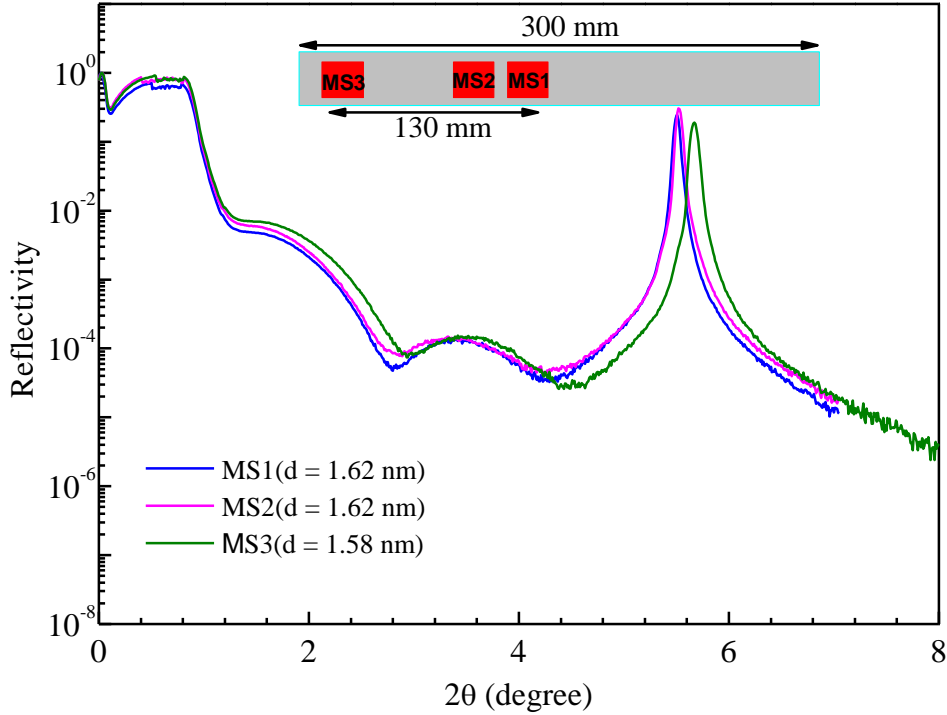


Figure 6.7 Measured HXR data (at Cu K_{α} energy) of three W/B $_4$ C ML samples (MS1, MS2, MS3) with a fixed $N= 300$ fabricated simultaneously.

6.3.4 Measured optical performance:

It is noteworthy that such high energy (soft gamma-ray) ML mirrors can be calibrated in a hard X-ray energy region that is easily obtainable using a synchrotron radiation source. Then, the optical performance in the soft gamma-ray energy region can be accurately predicted using the extrapolation of known optical constants of the materials [189, 190] and the measured structural parameters of the ML obtained from the hard X-ray data model. Thus, due to the unavailability of reflectometer based on soft gamma-ray energies and difficult for accessibility of such limited soft gamma-ray source based reflectometer at international, the optical performances are measured in the hard x-ray region (10-20 keV). It is noteworthy to mention that the structural parameters of ML mirrors derived from the model of hard x-ray data are in accordance with the measured optical performances in the hard x-ray region. This helps to accurately predict the performance of MLs for soft gamma rays. Fig. 6.8 shows

measured first order Bragg peak of ML with $d = 1.86$ nm in the selected energies from 10 to 20 keV. The clarity to the measured angular resolution of peaks at the selected energies is presented at the top of the fig. 6.8. At 10 keV, measured reflectivity is ≈ 64 %. As energy increases to 12 keV, reflectivity falls to ~ 37 % due to the presence of W L_{II}-edge at 11.544 keV. Again, the reflectivity increases as the incident photon energy increases further away from the W L-Edge. At 20 keV, measured reflectivity is ~ 55 %. In Fig. 6.9, the measured optical performances of three ML mirrors ($d = 1.86, 1.55$ and 1.23 nm) are compared at 10 keV, and the results are given in Table 6.3. $E/\Delta E$ is estimated using $E/\Delta E = \tan(\theta_{\text{Bragg}}) \times (1/\Delta\theta)$, where $\Delta\theta$ is the full width half maximum (FWHM) of the Bragg peak. For ML-1 ($d = 1.86$ nm), a significantly high reflectivity (≈ 64 %) is measured as compared to a theoretical value of 82 %. The difference between measured and theoretical values is mainly due to measured structural parameters of ML and ideal structure (zero interface width and bulk density). As period decreases to 1.55 nm (ML-2), reflectivity decreases to ≈ 39 % compared to theoretical value of 73 % due to slightly increase of interface width (≈ 0.285 nm), decrease of density contrast (13.1 g/cm^3) and q-dependency of reflectivity. However, the reflectivity catastrophically drops to ~ 1 % compared to theoretical value of 62 % as the period further decreases to 1.23 nm (ML-3). This is because of significantly reduction of density contrast (6.5 g/cm^3) and the increase of interface width. A similar drop in reflectivity is also observed in case of WC/SiC ML as the period decreases to ≤ 1.2 nm [9]. In order to account for the approximate $1/\theta^4$ dependency of reflectivity, plot of product of reflectivity and θ^4 as function of θ is shown in inset of Fig. 6.9. The inset clearly shows that in the case of ML-3, there is a significant decrease of peak intensities multiplied with θ^4 due to presence of higher structural imperfections. In Table 6.3, the energy resolving power ($E/\Delta E$) increases as period decreases. The reason is that as the period decreases, the angular positions of Bragg Peak shift towards

higher values (Fig. 6.9) and also at higher angle the larger number of layer pairs contribute to the reflection. It is noted that the measured optical performances in the energy range 10-20 keV are in accordance with the measured structural parameters of MLs. This provides a strong support for the argument about the prediction of the optical performance in the soft gamma-ray region from the structural parameters.

Table 6.3 The values of the measured peak reflectivities R and E/ΔE of three MLs at 10 keV.

Sample	d (nm)	R (%)	E/ΔE
ML-1	1.86	64	76
ML-2	1.55	39	133
ML-3	1.23	01	176

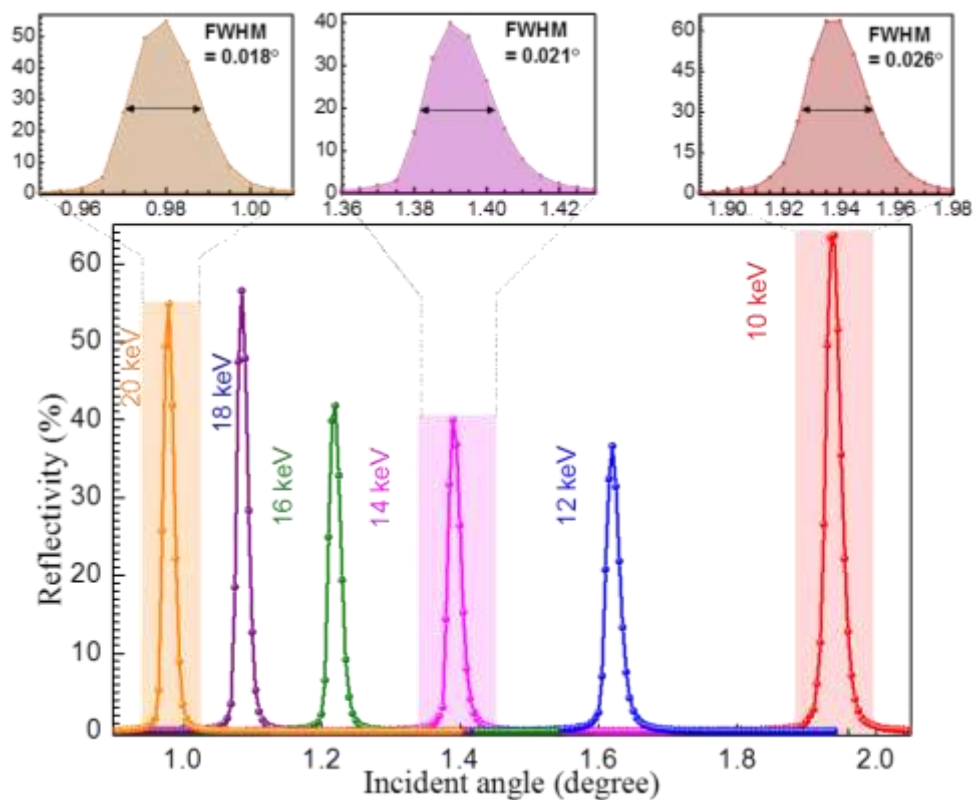


Figure 6.8 Measured optical performances of W/B₄C ML with d = 1.86 nm and N = 400 for selected energy in the energy range 10-20 keV. The reflectivity around 1st Bragg peak in the

linear scale as a function of the incident angle is shown in the lower figure. The top figures show more clearly the Bragg peaks at three selected energies to measure angular resolution.

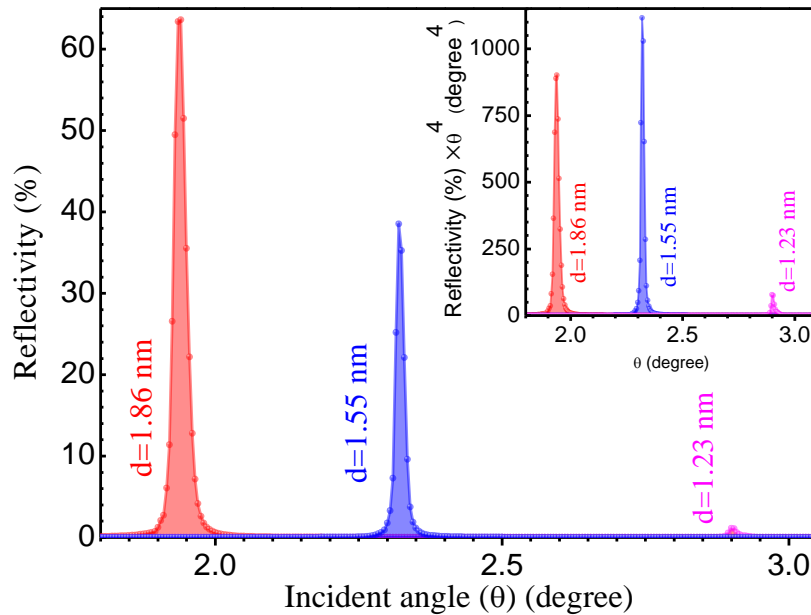


Figure 6.9 Comparative measured optical performances at 1st Bragg peak of three W/B₄C MLs with ML-1 ($d = 1.86$ nm), ML-2 (1.55 nm) and ML-3 (1.23 nm) at a fixed $N = 400$ at an energy 10 keV. Measured reflectivity profiles in the linear scale are plotted as a function of incident angle. The inset shows reflectivity multiplied with θ^4 as a function of θ .

6.3.5 Predicted soft gamma-ray performance:

It is known [185] that the position and amplitude of the first order Bragg peak can be accurately predicted at the soft gamma-ray region by a wave-optics formalism using the model derived from hard x-ray data. The predicted 1st Bragg peak reflectivities of these three MLs are calculated using IMD coded XOP software package [33] shown in the figure 6.10. The calculations have been done at energies 384 keV and 378 keV with the bandwidth of incident photon energy $\Delta E = 3$ keV and 9.8 keV, respectively. The calculations of the reflected intensities at the multiple discrete energies in the bandwidth interval with energy

step of 0.3 keV (0.5 keV) for $\Delta E = 3$ keV (9.8 keV) are averaged to account the respective resolution of incident photon energy.

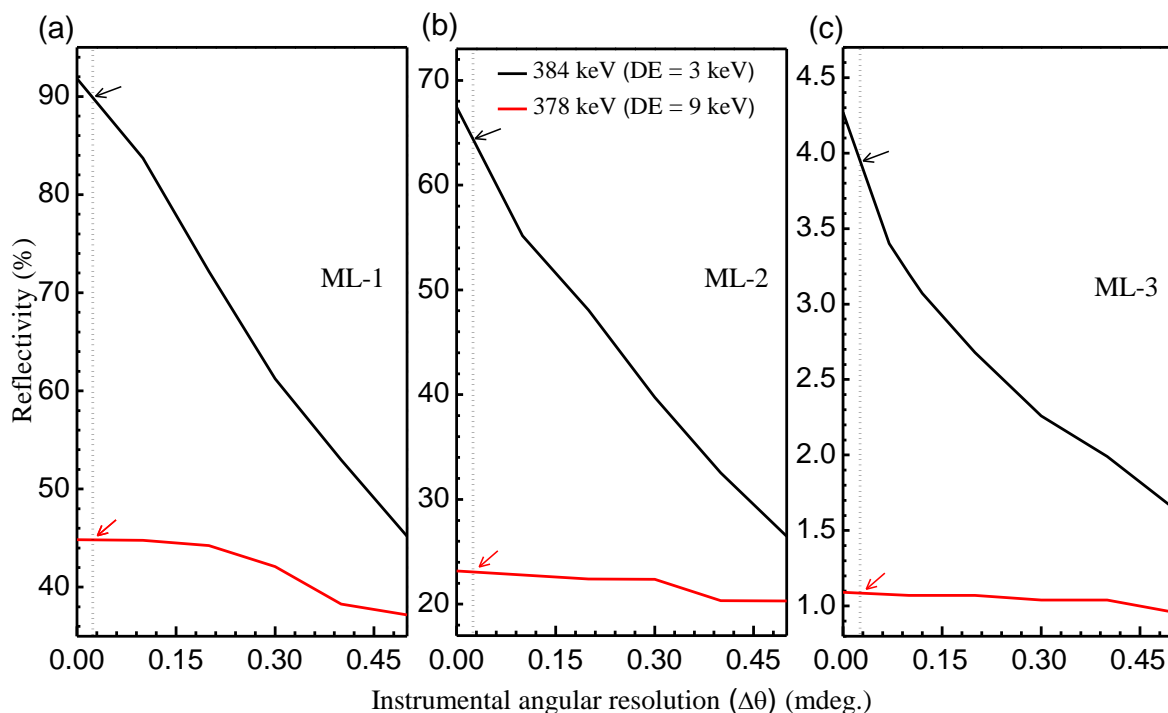


Figure 6.10 1st order Bragg peak reflectivity performances of three MLs with varying instrumental angular resolution ($\Delta\theta$) are calculated at energies of 384 keV ($\Delta E = 3$ keV) and 378 keV ($\Delta E = 9.8$ keV). The calculation is done with an angular step size 0.1 mdeg using measured structural parameters of MLs derived from hard x-ray data and by extrapolation of known optical properties of materials. The black line and red line indicate the energies 384 keV and 378 keV. The dotted line represents a typical instrumental angular resolution of 0.024 mdeg, where the respective peak reflectivities are marked by arrows. (a), (b) and (c) are for ML-1, ML-2 and ML-3, respectively.

It is noted that the calculated average reflectivity at 1st Bragg peak decreases with increasing instrumental angular resolution. Also, the Bragg peak appears at a very lower angle for that high energy application. For example, a typical reflectance band pass (FWHM) of the first order Bragg peak (position at ~ 50.4 mdeg) from ML with $d = 1.86$ nm and having an

instrumental angular resolution 0.024 mdeg is of the order of ~ 0.5 mdeg at energy 384 keV. Therefore, the instrumental angular resolution requires much lower value than FWHM of the Bragg peak. The predicted reflectivities are $\sim 90\%$, 64% and 4% for ML-1, ML-2 and ML-2, respectively for incident energy 384 keV having bandwidth 3 keV at the mentioned instrumental angular resolution of 0.024 mdeg (marked by arrows). On the other hand, the calculated reflectivities decrease to $\sim 45\%$, 23% and 1% for ML-1, ML-2 and ML-2, respectively while the bandwidth of incident beam increases to 9.8 keV at 378 keV. It may be noted for comparison that, at these same energies and identical bandwidth of incident photon energy, Fernandez-Perea *et al.* [9] evaluated the reflectivity of WC/SiC based soft gamma-ray ML optics ($d = 1.474$ nm, $N = 300$) with actual beam divergence 0.024 mdeg. Subsequently, 1st Bragg peak reflectivities are measured $\sim 52.6\%$ at energy 384 keV (with $\Delta E = 3$ keV) and $\sim 23\%$ at energy ~ 378 keV (with $\Delta E = 9.8$ keV). In both the cases, the difference in reflectivity is mainly because of the difference in periodicities ($d = 1.474$ nm earlier as compared to $d = 1.55$ nm in the present study). For example, if the period of W/B₄C ML is kept equal to 1.474 nm including all other parameters according to the present study, the predicted reflectivities are $\sim 53\%$ and 17% at energies 384 keV and 378 keV, respectively, which is comparable with WC/SiC. Therefore, a similar amount of peak reflectivity with the capability of having a higher optical contrast of W/B₄C ML is clearly expected to provide significantly higher photon flux than WC/SiC ML. The accurate integrated reflectivity around the Bragg peak can only be predicted using a combination of both wave-optics formalism as well as particle transport simulations because of Compton scattering [185], which is beyond the scope of the present study.

6.4 Conclusion:

Nano-scaled one dimensional periodic metal-based W/B₄C MLs are designed and developed for soft gamma-rays (100 -500 keV) reflective optics. The achievable rms interfacial

roughness (e.g., $\sigma = 0.27$ nm for ML with $d = 1.86$ nm and $N=400$) is ensured concurrently with low compressive residual stress (389 MPa) in ML stack, desirable for such high energy reflective optics. The required microstructure and residual stress achievements were simultaneously realized near the onset of grain growth of metal (on-set of the continuous layer) to prevent scaling of roughness. The precise structural parameters are unambiguously determined using complementary x-ray scattering techniques and high resolution TEM, and the results are well agreed, and correlated with residual stress. We present the optical superiority of the proposed metal based material system (Fig 6.1) and near perfect layer structure with achievable interface width as shown in figs. 6.2 to 6.5, along with tolerable range of residual stress and period uniformity. The good agreement between measured and predicted hard x-rays optical performances as illustrated in Figs 6.8 and 6.9. In addition with predicted optical performance of these ML mirrors in soft gamma ray region, makes a strong case supporting W/B₄C as one of a prospective material of choice for the next-generation high efficient soft gamma-ray reflective optics. The present study has the potential of advancing soft gamma-ray optics in the emerging field of soft gamma-ray spectroscopy as well as will open up a path for progress in the understanding of nano-science and technology.

Chapter-7

Future scope:

In this chapter, a short overview on prospective of future scope of the work has been discussed.

7.1 Future scope:

In the soft gamma-ray spectrometer, the main challenge is the requirement for efficient optics to deliver a sufficient amount of photon flux to improve the signal-to-noise ratio. This is because of the weak signal strength of emitted soft gamma-rays from distance stellar objects (for astrophysics application) as well as remnant radioactive isotopes in nuclear spent-fuel (nuclear technology application). This stipulates the need for a better material system for ML mirror that can provide both high peak reflectance as well as high integrated reflectance. In this study, it is found that the W/B₄C system as a candidate of choice for the soft gamma-ray mirror, by engineering the process parameters for higher structural requirements. There is a lot of interesting and important scope on this topic for the future works related to the W/B₄C ML system for soft gamma-ray ML optics as well as related surfaces/interface studies which are described comprehensively as follows:

As a part of the future scope, it is noted that due to readily unavailability of photon energies in the soft gamma-ray region, the optical performances are measured in the hard x-ray region (10-20 keV). It is noteworthy to mention that the calibration of such ML mirrors is done at hard x-ray region which is easily available using synchrotron facilities. The optical performance is accurately predicted at soft gamma-ray region using the extrapolation of known optical constants of materials and the structural parameters of ML derived from the model of hard x-ray data. However, it is interesting to measure the actual optical properties at the soft gamma-rays and to compare with the predicted values.

Regarding lateral period uniformity, there is a scope for further improvement of lateral uniformity by mounting an appropriate masking arrangement to control the spatial distribution of the rate of deposition over the target. Generally, in the rectangular cathode (target), the rate of deposition is more at the centre as compared with towards sides. So, in the

lateral direction (along the length of the substrate), by mounting an appropriate masking system having a tapering towards centre from both the ends, the spatial distribution could be controlled. This would improve the lateral period uniformity without disturbing other processing parameters. The lateral period uniformity along the width of the sample is ensured through the full swing of the sample across the width of the opening in front of the cathode.

In addition, to realize the Bragg reflection of such high energies, the period thickness of ML must be controlled to the shortest possible desired value with structural perfection at the atomic level. The main hindrance in attaining the ultimate shortest period is the limitation imposed by minimum thickness needed to form a continuous layer of homogeneous density (*continuous limit*) which depends on the material and its growth. Here, we have fabricated W/B₄C ML mirrors by changing period $d=1.86-1.23$ nm. The different periods were fabricated by varying thicknesses of the B₄C layers (0.92-0.33 nm), while keeping W layer thickness fixed at around 0.94 nm (because the continuous layer is formed around 1 nm). Through this design, good quality of MLs up to $d= 1.55$ nm (B₄C thickness 0.56 nm) is realized in terms of, interface width, optical contrast and low residual stress (required for such ML mirror). However, as d decreases further to 1.23 nm (B₄C layer thickness 0.33 nm), the contrast decreases significantly due to the formation of quasi-continuous layers. Since MLs with further smaller periods is desirable to be operated at relatively larger angles, it is interesting and important to fabricate MLs with shorter period than 1.55 nm by varying W thickness and keeping B₄C thickness fixed at around 0.5 nm. In this situation, W layers can be decreased in a controllable manner from 0.94 nm to 0.6 nm. As W layer decreased to 0.94-0.6 nm, it is important to systematically analyse the interfacial phenomena and correlate with the optical properties. In this way, one can study and establish a correlation between structure-properties and to understand up to what precise thickness of W could yield measured reflectivity more than 1 % @ 10 keV, which was observed in case of ML $d=1.23$

nm (B_4C thickness 0.33nm and W thickness 0.9 nm). This study would be certainly interesting to understand the scope for improvement of optical properties for MLs with period down to 1.55 nm.

Further, as we mentioned very good quality of the ML mirrors for soft gamma-rays are produced on smaller research grade substrates (30 mm \times 20 mm). it is important and interesting to fabricate on the larger substrates (100 mm \times 50 mm). Ten such substrates can be mounted in a cascading manner to form a single mirror (joined) up to a length of 1000 mm to develop the soft gamma-ray spectroscopy based on the developed ML optics. So, there is an interesting and important future scope for the development of the ML optics based soft gamma-ray spectroscopy for frontier areas of science and technology. The deposition chamber is able to accommodate substrate having size~500 mm (length) \times 100 mm (width) and thickness up to 30 mm. Considering the requirement of the better lateral period thickness uniformity, the length of the substrate is restricted to maximum up to 300 mm.

Further, here only W/ B_4C ML system was studied as a prospective potential material combination for the soft gamma-ray mirror. However, there is a wide scope to further search for a better material system as an efficient mirror for such high energies as well as to study their experimental feasibilities considering the higher structural requirements for such reflective optics. In addition, regarding the demonstration of the novel technique/methodology based on soft x-ray reflection spectroscopy, it is required to probe more complex interfaces of different material systems with unknown chemical compositions and to understand their interface phenomena using this technique for mapping chemically and spatially resolved interfacial map.

Name of the Student: Arindam Majhi

Title of the thesis: Surface/interface studies of thin films and development of ultra-short period W/B₄C multilayer mirrors with large layer pairs

Thesis Abstract

This thesis consists of two parts. The first part describes an experimental demonstration of a novel analytical technique for surface/interface science of nano-scaled layer structure materials using the synchrotron. The novel approach is developed by combining the resonant soft x-ray reflection spectroscopy grazing incidence near the critical angle with angular dependent reflection at energies around the respective absorption edges to precisely quantify spatio-chemical depth profile in a non-destructive manner. To support the validity of the approach, the reflection spectra are reviewed in parallel with the routinely used NEXAFS spectroscopy, which were measured simultaneously. The technique enables to map chemical profile to distinguish with compositional differences of few atomic percent from free to the embedded layers up to few tens of nanometers. It is difficult to obtain such spatio-chemical information using the conventional spectroscopy technique in a non-destructive manner.

The second part involves development of the multilayer (ML) mirrors with large layer pairs for soft gamma-ray spectroscopy (100-500 keV), and the related surface/interface studies. The fabrication of such ML optics is a challenging aspect, where the control of structural parameters on angstrom level is required along with the number of layer pairs (300-400) with period thickness 1-2 nm. Apart from fabrication, understanding surface/interface of such nano-scaled layered structure materials is a crucial aspect, which is systematically studied using synchrotron based x-ray reflectivity, glancing angle x-ray diffraction and laboratory based rocking scan as well as reciprocal space mapping. In addition, a detailed understanding of the evolution of residual stress and its correlation with microstructure has been studied by varying individual layer thickness near the ultra-thin region in W/B₄C MLs. This helps to improve the minimum thickness for the onset of continuous layer by optimization of process parameters for smooth interface. Thereafter, a correlation study of stress-structure analysis by varying the number of layer pairs up to $N = 400$ at a fixed ultra-short period ~ 1.9 nm is carried out to obtain low residual stress with low interfacial width required for gamma-ray reflective optics. Finally, W/B₄C ML optics for gamma-ray are successfully developed with low residual stress and with achievable interfacial width so far along with high optical contrast by varying period $d = 1.86-1.23$ nm at fixed number of layer pairs, $N=400$. The high quality developed ML optics is successfully tested using Indus synchrotron.

Arindam Majhi

Thesis Highlight

Name of the Student: Arindam majhi

Name of the CI/OCC: Raja Ramanna Centre for Advanced Technology

Enrolment No.: PHYS03201404006

Thesis Title: Surface/interface studies of thin films and development of ultra-short period W/B₄C multilayer mirrors with large layer pairs

Discipline: Physical Science

Sub-Area of Discipline: X-ray optics

Date of viva voce: 23/12/2020

A novel analytical approach of “near edge soft x-ray reflection spectroscopy technique” based on resonant x-ray scattering is demonstrated for surface/interface science of nano-scaled layer structure materials using the synchrotron. The novel approach is developed by combining the resonant soft x-ray reflection spectroscopy grazing incidence near the critical angle with angular dependent reflection at energies around the respective absorption edges to precisely quantify spatio-chemical depth profile in a non-destructive manner. To support the validity of the approach, the reflection spectra are reviewed in parallel with the routinely used NEXAFS spectroscopy, which were measured simultaneously. The developed approach is clearly demonstrated on the fabricated layered structure C (20 Å)/B (40 Å)/Si(300 Å)/W(10 Å)/Substrate. The technique enables to reconstruct chemically and spatially resolved atomic profile from free to the embedded layers up to few tens of nanometers with compositional differences of few atomic percent.

In addition, the development of the multilayer (ML) mirrors with large number of layer pairs has been undertaken for soft gamma-ray spectroscopy (100-500 keV) along with the studies related to surface/interface physics. Apart from fabrication, understanding surface/interface of such nano-scaled layered structure materials is a crucial aspect, which is systematically studied using synchrotron based x-ray reflectivity, glancing angle x-ray diffraction and laboratory based rocking scan as well as reciprocal space mapping. In addition, a detailed understanding of the evolution of residual stress and its correlation with microstructure has been studied by varying individual layer thickness near the ultra-thin region in W/B₄C MLs. Thereafter, a correlation study of stress-structure analysis by varying the number of layer pairs up to N = 400 at a fixed ultra-short period ~1.9 nm is carried out to obtain low residual stress with low interfacial width required for gamma-ray reflective optics. Finally, W/B₄C ML optics for soft gamma-ray are successfully developed with low residual stress and with achievable interfacial width so far along with high optical contrast by varying period d = 1.86-1.23 nm at fixed number of layer pairs, N=400. The high quality developed ML optics (except for d=1.23 nm due to quasi discontinuous, which decreases optical contrast) is successfully tested using Indus synchrotron.

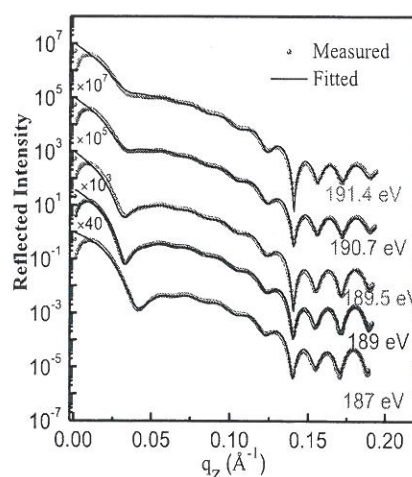


Figure 1 Quantitative structural and compositional analysis using angular resolved R-SoXR around the B K-edge.

Arindam majhi